

Thales Schröttner

**Design, Characterization and
Optimization of various
 β γ Measurement Systems**

DISSERTATION

zur Erlangung des akademischen Grades
Doktor der technischen Wissenschaften

Doktoratsstudium der technischen Wissenschaften
Technische Physik



Technische Universität Graz

Betreuer:

Univ.-Prof. Dipl.-Ing. Dr.techn. Peter Kindl
Institut für Materialphysik

Dipl.-Ing. Dr.techn. Martina Schwaiger, MBA
Seibersdorf Labor GmbH

Graz, März 2010

Acknowledgment

I would like to take this opportunity to thank all those who helped to make this work possible. First of all I would like to thank the coauthors of my publications Dr. Martina Schwaiger, Prof. Peter Kindl, Dr. Gérard Presle, DI Irene Schraick and Dr. Thomas Furch for their help and contributions.

My utmost gratitude goes to my thesis advisor Prof. Peter Kindl for precious discussions and many ideas relating not only to scientific but also general issues and for his friendly and flexible support.

My thanks and appreciation goes to my local supervisor in Seibersdorf, Dr. Martina Schwaiger for constant encouragement and support of my scientific work.

My gratitude extends to the management of the Seibersdorf Laboratories and the former Austrian Research Center for financial support of this work and for providing facilities, laboratories, instrumentation and equipment on a top level unique for Austria, which has been one base for effective scientific work.

Thanks to the staff of the Seibersdorf Laboratories and the Austrian Institute of Technology, especially the department of Radiation Safety and Applications. The friendly team and the familial working conditions have been the second base for successful scientific work.

Above all, I thank my beloved wife for being so patient with me, when neglecting my duties in the family, especially during the final phase of my work, which had to be done in addition to my regular employment.

Kurzfassung

Diese Doktorarbeit basiert auf vier von Experten begutachteten (peer-reviewed) Publikationen und beinhaltet die wissenschaftliche Arbeit von 2002 bis 2009. Den vier Publikationen entsprechen die vier Hauptkapitel der vorliegenden Arbeit. Der gemeinsame Schwerpunkt dieser Publikationen liegt in der Physik und Elektronik von Messsystemen für ionisierende Strahlung. Das gemeinsame Ziel ist die Optimierung der Messsysteme und die Erhöhung der Empfindlichkeit durch Verbesserung des Signal-Rausch-Verhältnisses (SRV).

Dies wurde durch die Reduktion des kosmischen und terrestrischen Strahlungsuntergrundes sowie durch die Verringerung von elektromagnetischen Interferenzen (EMI) und elektronischem Rauschen realisiert. Eine weitere Methode welche angewandt wurde, um das SRV zu erhöhen, war die Verwendung einer adaptiven Integrationszeit um das Verhältnis von aufgezeichneten Signal- und Untergrundimpulsen zu optimieren. Bei spektroskopischen Messsystemen spielt auch die Energiekalibrierung eine Schlüsselrolle für ein hohes SRV, da die Nachweisgrenze von der Energie-Auflösung sowie der Stabilität der Energie-Kalibrierung abhängt.

Die erste Publikation mit dem Titel „*Optimization of an active anti cosmic veto shielding*“ (Schroettner et al., 2004), behandelt die Optimierung eines Low-Level Gamma-spektroskopie Messsystems. Dabei wurde Zeitspektroskopie der kosmischen Myonen, welche den Guard-Detektor passieren und der entsprechenden Untergrundsignale im Germanium-Detektor angewandt, um das Zeitfenster der Antikoinzidenz zu optimieren.

Weiters wurde die Fluktuation des Myonenflusses untersucht und die daraus resultierende Variation der Quantenausbeute berechnet und optimiert. Um die Wirkung der aktiven Abschirmung auf niedrigere Gamma-Energien zu erweitern, wurden systematisch die Quellen für elektronisches Rauschen und elektromagnetische Interferenzen lokalisiert und eliminiert. Eine komplett galvanisch getrennte nullungsfreie Stromversorgung für das Labor wurde mittels elektronischer Filter und kompletter Netznachbildung durch eine unterbrechungsfreie Stromversorgung (USV) realisiert.

Die zweite Publikation mit dem Titel „*Enhancing sensitivity of portal monitoring at varying transit speed*“ (Schroettner et al., 2009) beschäftigt sich mit der Charakterisierung von Portalmonitoren, die auf Plastik-Szintillatoren basieren und stellt neue Methoden zur Erhöhung der Messempfindlichkeit bei veränderlichen Durchgangsgeschwindigkeiten vor. Die Resultate der Charakterisierung der Strahlungsdetektoren werden verwendet, um das Messsignal für unterschiedliche Geschwindigkeiten und Normalabstände zu simulieren. Diese Simulation diente als Basis, um einen neuen Algorithmus zur geschwindigkeitsabhängigen Datenauswertung des Zählratensignals zu entwickeln.

Das SRV und die Nachweisgrenze wurden als Funktion der Integrationszeit berechnet und so ihr Optimum bestimmt. Die Algorithmen wurden experimentell an einem hochgeschwindigkeits-Quellentransportsystem validiert, welches ein bewegtes Objekt mit einer radioaktiven Quelle simuliert.

In der dritten Publikation "*Long term comparison of methods to sustain energy calibration in low level gamma-ray spectroscopy and investigation of possible sources for drift*" (Schroettner and Kindl, 2010) wurden verschiedene Ursachen für die Drift der Energiekalibrierung von Germanium-Detektoren untersucht. In einer Langzeitstudie über mehrere Jahre wurden verschiedene Verfahren zur Energiekalibrierung (Quelleneinschuss und Pulser Methode) verglichen und ein neues Konzept zur Überwachung und Stabilisierung der Energiekalibrierung von Germanium-Detektoren präsentiert, welches die übliche Kontrolle der Energiekalibrierung ersetzt.

Die vierte Publikation "*A high resolution, multi parameter, β - γ coincidence μ - γ anticoincidence system for radioxenon measurement*" (Schroettner et al., submitted to NIM A on 30.1.2010) beschreibt ein neues hochauflösendes Multi-Parameter Messsystem, in dem β - γ Koinzidenz und μ - γ Antikoinzidenz kombiniert zur Anwendung kommen. Das Messsystem wurde für die Messung von Radioxenon Proben und Kalibrierstandards entwickelt. Ein Germanium-Detektor wird zum Nachweis der Photonen und ein Silizium-Sperrschicht-Detektor zum Nachweis der Elektronen verwendet, um die koinzidente γ /Röntgen und β /Konversionselektronen Strahlung zu messen. Die Datenerfassung im Listmodus erlaubt nachträglich eine Veränderung und Optimierung der Zeitfenster für die (Anti-)Koinzidenz bei der Auswertung der Messdaten. Das System könnte auch als α - γ Koinzidenz zur Überwachung von Nuklearanlagen oder zur nuklearen Forensik eingesetzt werden.

Schlagwörter: aktive Abschirmung, cosmic-Veto, Zeitspektroskopie, Untergrundreduktion, Zugmonitoring, Portalmonitore, hohe Durchfahrtsgeschwindigkeit, Integrationszeit, Empfindlichkeit, Nachweisgrenze, Energiekalibrierung, Low-Level Gammaspektroskopie, Gain-Stabilisierung, elektronische Drift, Referenzpeak, Pulser, Detektor Qualitätssicherung, β - γ Koinzidenz, μ - γ Antikoinzidenz, hochauflösend, BEGe, SSB, Radioxenon, Multiparameter, Listmodus, Konversionselektron

Abstract

This thesis is based on four peer reviewed publications and reflects the scientific work from 2002 to 2009. These four papers correspond to four main chapters of the thesis. The common sense of the work is the focus on physics and electronics of measurement systems for ionizing radiation. The common aim is to increase measurement performance and sensitivity by increasing the signal to noise ratio (SNR).

This has been realized by reduction of the terrestrial and cosmic radiation background and by minimizing of electromagnetic interference (EMI) and noise pick up by electronic measures. Another method, applied to increase the SNR, utilized adaptive integration time to optimize the ratio of recorded signal and background counts. For spectroscopic systems, also the stability of the energy calibration plays a key role for high SNR, as the detection limit depends on the energy resolution and stability of energy calibration.

The first paper '*Optimization of an active anti cosmic veto shielding*' (Schroettner et al., 2004) deals with optimization of a low level gamma spectroscopy system. Time spectroscopy of the cosmic muons passing the guard detector and the related background signals in the high purity germanium (HPGe) detector has been applied to optimize the veto time window. The fluctuation of the muon flux has been investigated and the possible induced drop and variation of measurement efficiency have been calculated and minimized. To extend the operation of the active veto towards lower γ -energies, the electronic noise and interference has been reduced by systematic location and elimination of the sources. A totally isolated power net employs filtering and regeneration of the power line for the laboratory.

The second paper '*Enhancing sensitivity of portal monitoring at varying transit speed*' (Schroettner et al., 2009) contains a characterization of a plastic scintillation based portal monitoring system and presents a method to increase the sensitivity of the system at varying transit speed. The detector-characterization results are used to simulate the signal for various speed and off axis distance. The simulation has been used to develop and test new algorithms for speed dependent data processing of the count rate signal. The SNR and the minimum detectable activity (MDA) have been calculated as function of the integration time to obtain their optima. The algorithms are experimentally validated by using a high speed source transport system to simulate a passing source.

The third paper '*Long term comparison of methods to sustain energy calibration in low level gamma-ray spectroscopy and investigation of possible sources for drift*' (Schroettner and Kindl, 2010) investigates various sources for drift of energy calibration of HPGe detectors.

A long term comparison of different methods for energy calibration (source injection method and pulser method) shows pros and cons and presents a new concept to monitor and sustain energy calibration of gamma spectroscopic measurement systems.

The fourth paper '*A high resolution, multi parameter, β - γ coincidence, μ - γ anticoincidence system for radioxenon measurement*' (Schroettner et al., submitted on 30.1.2010 to NIM A) describes a novel high resolution multi parameter measurement system combining β - γ coincidence and μ - γ anticoincidence. The system is intended for measurement of radioxenon samples and calibration of radioxenon spikes. A HPGe detector for photons and a silicon surface barrier (SSB) detector for electrons are combined to measure coincident γ /x-ray and β /conversion electron radiation. The data acquisition in list mode allows changing, checking and optimizing all time windows for (anti-) coincidence off line during data processing and analysis. The system has been designed to be operated also in α - γ coincidence mode which can be applied to nuclear safeguard (forensics).

Keywords: active shielding, veto shielding, anti cosmic, time spectroscopy, background reduction, train monitoring, portal monitoring, high transit speed, speed-dependent detection algorithm, signal to noise ratio, integration time, sensitivity, minimum detectable activity, energy calibration, low level gamma-ray spectroscopy, gain stabilization, electronic drift, reference peak, pulser, gain stabilizer, detector QC, β - γ coincidence, μ - γ anticoincidence, high resolution, HPGe, SSB, radioxenon, multi parameter, list mode, conversion electron

Table of contents

Acknowledgment	2
Kurzfassung	3
Abstract	5
Table of contents	7
List of figures	10
List of tables	12
Preface	13
1 Introduction	14
1.1 Radiation origin, propagation and measurement basics	14
1.2 Reliable nuclear data	15
2 Optimization of an active anti cosmic veto shielding	16
2.1 Introduction	16
2.2 Measurement setup of the active anti cosmic veto shielding	16
2.3 Time spectroscopy to optimize the time-window	18
2.4 Countermeasures against electromagnetic interference	21
2.5 Discussion	23
2.6 Conclusion	23
3 Enhancing sensitivity of portal monitoring at varying transit speed	24
3.1 Introduction	24
3.2 Motivation.....	24
3.3 Concept and application of speed dependent signal processing	25
3.4 Dependence of sensitivity on the chosen integration time	26
3.5 Comparison with previous work	26
3.6 Experimental determination of the efficiency	27
3.7 Measurement methods and consideration of the uncertainties and error propagation	28
3.8 Static measurement of quantum efficiency	28
3.9 Dynamic measurement for testing implementation	28
3.10 Semi-empirical fit of the data	29
3.11 Influence of the measurement geometry on the FWHM of the signal shape	32
3.12 Calculation of the MDA for different integration times.....	34

3.13	Influence of varying integration time on MDA and critical level.....	35
3.14	Signal and standard deviation at MDA level	35
3.15	Influence of the integration time on the MDA.....	36
3.16	Optimum integration time.....	36
3.17	Calculation of the signal to noise ratio	38
3.18	Comparison of optimum MDA vs. optimum SNR consideration	42
3.19	Use of speed dependent signal processing in combination with other advanced processing methods	43
3.20	Application of the system for train monitoring	43
3.21	Comparison of conventional and speed dependent signal processing.....	44
3.22	Conclusion and Interpretation	45
4	Methods to sustain energy calibration in low level gamma-ray spectroscopy.....	46
4.1	Introduction	46
4.1.1	Accuracy and stability of energy calibration.....	46
4.1.2	Concept of energy calibration used in the experiment.....	47
4.1.3	Spectrum stabilization by a reference peak	47
4.2	Methods	48
4.2.1	Source injection method	48
4.2.2	Pulser method.....	49
4.2.3	Investigation of the possible causes for the drift of energy calibration.....	50
4.3	Results and Discussion.....	51
4.3.1	Drift of offset and gain.....	51
4.3.2	Initial energy calibration	51
4.3.3	Long term study of the source injection method	51
4.3.4	Long term comparison of the pulser method	52
4.3.5	Investigation of the causes for system gain drift.....	53
4.4	Conclusions	55
4.4.1	Accuracy and drift stability of the source injection method	55
4.4.2	Accuracy and drift stability of the pulser method	55
4.4.3	Advantages - pulser method	55
4.4.4	Advantages - source injection method.....	55
5	High resolution beta-gamma-muon (anti-) coincidence radioxenon measurement.....	56
5.1	Introduction	57
5.1.1	Radioxenon measurement for treaty verification	57
5.1.2	Calibration of radioxenon spikes.....	58
5.1.3	Re-measurement of xenon samples from stations	58
5.2	Methods	58
5.2.1	High resolution β - γ spectrometer.....	58
5.2.2	Radiation detectors and preamplifiers	58

5.2.3	Measurement cell.....	60
5.2.4	Acquisition system	61
5.2.5	Energy calibration and performance test	64
5.2.6	Data analysis	66
5.2.7	Efficiency calibration	67
5.2.8	Absolute measurement of activity	69
5.2.9	Methods for radionuclide production	70
5.2.10	Monitoring of system performance and data quality	70
5.3	Results and Discussion.....	72
5.3.1	Spectra of different radionuclide isotope mixtures.....	72
5.3.2	Absolute measurement of activity	74
5.3.3	Background reduction by μ - γ anticoincidence	74
5.3.4	Calculation of the minimum detectable activity	78
5.4	Conclusions	81
5.4.1	Operation of the β - γ coincidence measurement system	81
5.4.2	Background reduction and MDA	81
	References.....	83
	Statutory declaration	96
	Curriculum vitae.....	97

List of figures

Fig. 1. Block diagram of the veto electronic.	17
Fig. 2. Distribution of time differences Δt between plastic scintillator and germanium detector.....	19
Fig. 3. Background Spectra without and with veto.	21
Fig. 4. Circuit diagram of the EMI filters used.	22
Fig. 5. Source transport system for testing of portal monitors.....	29
Fig. 6. Drawing of the geometry, the basis for equation 2.....	30
Fig. 7. Relative efficiency depending on off axis distance (OAD) and shielding as a function of source position x , ranging from -2 to 21 m, displayed in semi-logarithmic scale. These are measured points plus fitting function using equation 2.	32
Fig. 8. Relative efficiency depending on off axis distance (OAD) and shielding as a function of source position x , ranging from 0 to 5.1 m, displayed in linear scale.....	33
Fig. 9. MDA depending on the integration time (off axis distances 2.5 m).	37
Fig. 10. MDA in kBq depending on object speed and according (optimum) integration time.	38
Fig. 11. SNR (signal to noise) as function of the integration time for various speeds, at 2.5 m OAD (off axis distance) and for the according MDA (minimum detectable activity).	39
Fig. 12. SNR as function of the integration time for different ^{137}Cs activities, at 2.5 m OAD and for 1.4 m/s (5 km/h).	40
Fig. 13. SNR-optimum integration time (t) depending on ^{137}Cs activity (A), at a speed of 1.4 m/s (5 km/h).	41
Fig. 14. SNR-optimum integration time depending on the speed (v), for an activity of 1 MBq ^{137}Cs	42
Fig. 15. The monitoring system near Vienna consisting of six daisy chained portals.	44
Fig. 16. Schematic drawing of the pneumatic source transport system.	49
Fig. 17. Schematic signal characteristic of the shaped gamma ray (S1) and pulser (S2) signal and the pulse injected into the preamp (P).....	50
Fig. 18. Long term drift of two spectrometers measured by source injection and by pulser method, normalized at 1 MeV	52
Fig. 19. Drift of the energy calibration, stabilized by pulser, normalized at 1 MeV.....	53
Fig. 20. Gain drift of the sole spectrometer, normalized at 1 MeV.....	54

Fig. 21. Schematic drawing of the measurement cell. (copper parts in brown, SSB detector in golden, screw for calibration source in yellow, connectors and bolting in grey and carbon epoxy window in black color)	61
Fig. 22. Schematic drawing of the electronics for data acquisition.	63
Fig. 23. Picture of the ^{166m}Ho β - γ energy calibration sources.	65
Fig. 24. β - γ spectrum of the ^{66m}Ho energy calibration source. The x-axis relates to photon energy, y-axis to electron energy and the z-axis to the number of counts.	66
Fig. 25. Spectra for monitoring of system performance. a) ungated gamma energy spectrum; b) ungated beta energy spectrum; c) coincidence time spectrum; d) gated gamma energy spectrum ; e) gated beta energy spectrum; f) 3D spectrum beta x gamma; g) vetoed gamma energy spectrum; h) myon time distribution RTC; i) myon time distribution TADC	72
Fig. 26. β - γ spectrum of pure ^{131m}Xe	73
Fig. 27. β - γ spectrum of ^{133}Xe and ^{133m}Xe	74
Fig. 28. MDA for ^{133}Xe , ^{133m}Xe , ^{131m}Xe , ^{135}Xe as function of measurement time.	80

List of tables

Table 1 Experimentally determined parameters for the efficiency function of a single pillar.....	27
Table 2 Influence of the off axis distances (OAD) and shielding on the FWHM of the signal.	34
Table 3 Dependence of the MDA on the integration time at various speeds	45
Table 4 Detector specifications.....	59
Table 5 Energy shift of the conversion electrons by the lacquer coating.	65
Table 6 Peak efficiency of selected 3D peaks of radioxenon isotopes	68
Table 7 Comparison of veto implementation by TAC-ADC and RTC method.....	76
Table 8 TAC-ADC processing summary.....	77
Table 9 Improvement of the MDA by application of (anti-) coincidence.....	81

Preface

This thesis is focused on the improvement and the application of measurement techniques for β and γ radiation and associated methods for data analysis. Methods and techniques presented within this work are aimed to improve detection, identification and quantification of radioactive sources in situ and under laboratory conditions. The work covers only a small part of the area of radiation detection and measurement, but the presented principles can be assigned on many similar applications.

Optimization and design of measurement systems requires exact knowledge of the limiting factors related to boundary conditions of applied methods. Application of this knowledge allows to determine, which parameters are not critical and do not need much attention. It allows focusing resources on the important key parameters. This experience resulted in my personal belief, that the knowledge about boundary conditions, the limitations of methods and the resulting identification of the key parameters is the basic prerequisite for successful design and optimization of measurement systems.

The challenge to design a measurement system is not to answer the question, what is needed, but rather what is not needed.

The ultimate measurement system should not only use recent technology to surpass existing performance, but rather make more efficient use of established and proven technology without wasting resources.

My special thank goes to the Technical University of Graz for providing me comprehensive skills and tools for calculating and modeling of error propagation, which have been the most useful tools for me, to assess and identify the limiting system parameters. The application of these skills helped me many times, to locate the major source of uncertainty and to focus on it.

1 Introduction

The demanding requirements for the peer reviewed publications lead to an elevated scientific level of this work which implies an experienced reader. Therefore, the common disquisition on basics of radioactive decay, radiation interaction and radiation measurement, which is part of many theses, has been omitted here. Nevertheless, the common reference books, covering these topics should be cited here for the sake of completeness.

1.1 Radiation origin, propagation and measurement basics

Radiation measurement covers a wide field of physics, including physics of gas excitation and ionization, solid state physics with a strong emphasis on nuclear electronics.

The study-book '***Techniques for Nuclear and particle Physics Experiments***' by **W.R. Leo** is partly focused on high energy physics, but the author presents common measurement electronics and detectors to illustrate their operating mode. The book is very useful to obtain a good overview of radiation detectors and associated electronics. In addition to detectors and electronics, it covers radioactive decay and radiation interaction, radiation protection and statistics of radiation measurement.

The reference-book '***Radiation Detection and Measurement***' by **G. Knoll** is similarly aligned, but a bit more comprehensive and offers more profoundness. It is the best established reference book for radiation measurement and detectors, covering radioactive decay, radiation interaction, statistics, all common and many very specific detectors, spectroscopy, neutron detectors, electronics and background reduction techniques.

The reference book '***Handbook of Radioactive Analysis***' by **M. F. L'Annunziata** is primarily focused on radiochemistry and offers a content very complementary to the two books cited above. It extends in-depth to detection of α -radiation and presents the basics from a slightly different view of a radio chemist. Tracer methods, liquid scintillation counting, Cherenkov counting, flow scintillation counting and radionuclide imaging are explained in a very detailed way.

The reference book '***Gamma and X-Ray Spectrometry with Semiconductor Detectors***' by **K. Debertin and R. G. Helmer** is focused on gamma spectroscopy and presents in detail related techniques and necessary calibrations and provisions. It also deals with problems of practical application like summing correction and nuclear decay data.

1.2 Reliable nuclear data

Although nuclear data should be physically constant, it has to be measured or derived by theoretical considerations. These limitations result in considerable uncertainty and discrepancies between various sources, which can be much higher than reported uncertainties. Therefore, it is important to use the most reliable available sources.

Unfortunately there is no single comprehensive source, but rather a hierarchy based upon the compromise between availability, usability and reliability of the source.

The best validated source for decay data is the '**Table de Radionucléides**' provided by the **Laboratoire National Henri Becquerel**. The data from various sources is evaluated and weighted by an international collaboration (**Decay Data Evaluation Project**) including members of France, Germany, USA, Russia, UK and Spain. The high quality data can be obtained free of charge in the form of a comprehensive Table on CD or by downloading from the BIPM server:

http://www.nucleide.org/Publications/monographies_bipm.htm

or alternatively as separate file for each radionuclide:

http://www.nucleide.org/DDEP_WG/DDEPdata.htm

The work of the Decay Data Evaluation Project does not include all radionuclides; therefore alternative comprehensive sources are necessary.

A very comprehensive and relatively reliable source is provided by the National Nuclear Data Center (**NNDC**) in **Brookhaven**, USA:

<http://www.nndc.bnl.gov/>

The data is mirrored by several other international institutions but to obtain the most recent data it is recommended to access the data directly.

An older, but very useful source is the '**Table of Isotopes**' by **R. B. Firestone**. Although the data is about ten years old, the decay schemes are very descriptive and the whole data is available on CD and can be easily used off line too.

2 Optimization of an active anti cosmic veto shielding

Abstract

The active veto shielding of a low-level gamma spectrometer has been optimized to reduce the background in the energy interval 20-2700 keV by a factor of nine. The signal to noise ratio was increased, due to the reduction of electromagnetic interference coming from the power line, by using an uninterruptible power supply and specifically designed line filters. The overall performance of the veto shielding was improved by using time spectroscopy to find the optimum time duration for the coincidence window.

Keywords: active shielding, veto shielding, anti cosmic, time spectroscopy, background reduction

2.1 Introduction

In the year 2000, a new laboratory was set up to perform gamma spectroscopic measurements of low level environmental samples, especially air filter samples for the Comprehensive Nuclear Test-Ban Treaty Organization (CTBTO). The Laboratory has been certified by the CTBTO for this purpose in December 2001. The required minimum detectable activity (MDA), calculated according to Currie (1968), of 24 mBq ^{140}Ba should be reached within seven days. This limit can be achieved after only 12 hours measurement by the use of an active anti cosmic veto shielding. This paper discusses measures undertaken in the year 2002 and 2003 to extend the energy range of the veto shielding and to optimize the veto time window for coincidence, which is a key parameter for the effectiveness of the active veto shielding. To optimize the coincidence time of the veto shielding, time spectroscopy of the time differences between the signals from the muons in the guard detector and the signals in the germanium detector was used.

2.2 Measurement setup of the active anti cosmic veto shielding

The whole laboratory is located above ground in a former fall-out shelter. The 30 cm thick concrete walls act as a first layer of shielding. Inside the shelter a steel chamber made of 5 cm thick old ^{60}Co free steel has been installed as a second layer of shielding. The main shielding consists of 13 cm thick lead with ^{210}Pb radio impurities below

130 Bq/kg, 8 cm boron doped paraffin and another 2 cm of low level lead with a ^{210}Pb content of less than 20 Bq/kg. The main shielding of the gamma spectrometer is surrounded on top and on the sides by 6 plates of 5 cm thick plastic scintillation detectors manufactured by Bicron (USA). The muon flux through these guard detector plates has been measured during six months to be about 350 muons/s with a fluctuation of about $\pm 30\%$, but due to the dependency on the solar activity bigger deviations can be expected over longer periods. As reported by Pointurier et al. (1996), the energy deposition of the muons in the plastic scintillation detectors is about 2 MeV/cm. The total energy deposition depends on the impact angle, but is always above 10 MeV for the 5 cm thick plates used in the system discussed here. The thresholds for the plastic guard detectors are set to about 2 MeV to make them insensitive for environmental gamma radiation. This is to avoid interference with calibration sources used in the second gamma-spectrometer nearby the system under discussion.

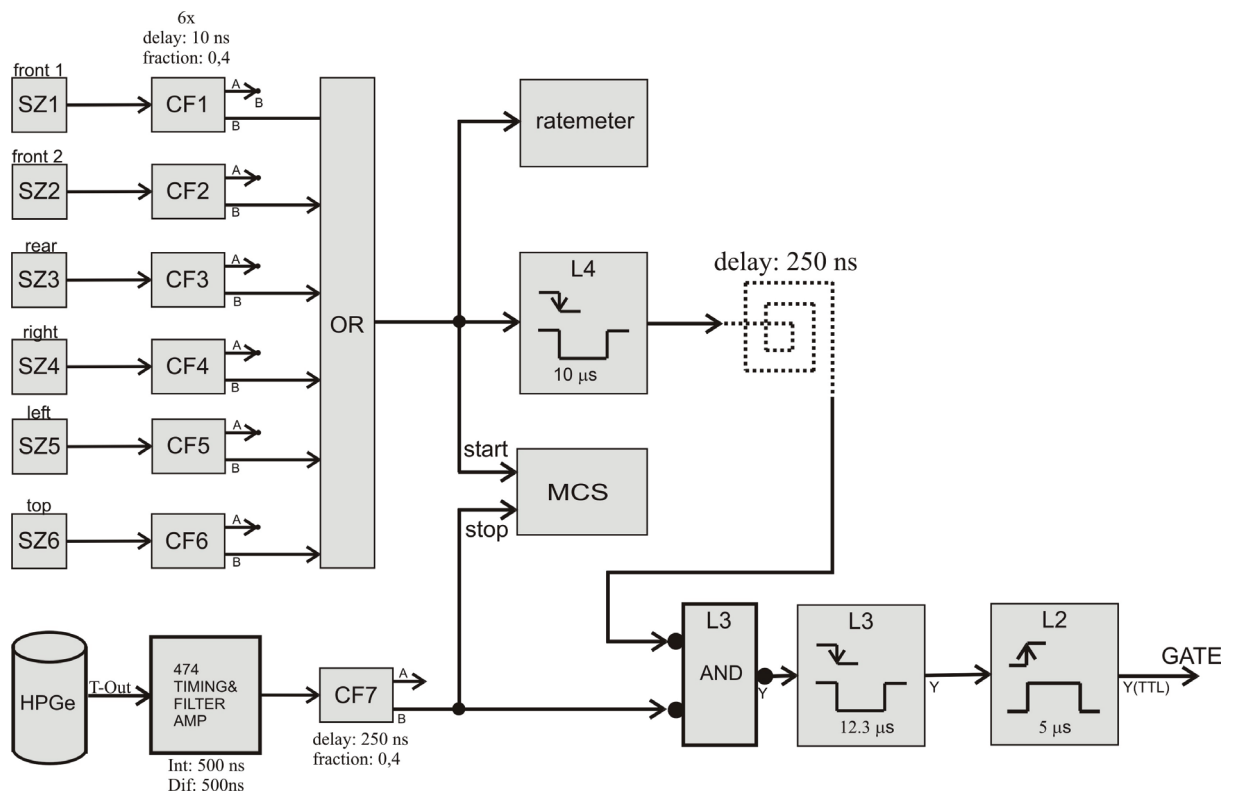


Fig. 1. Block diagram of the veto electronic.

Figure 1 shows a block diagram of the electronics used for the active veto shielding. The signals from all six scintillation plates, labeled in figure 1 as SZ1 – SZ6, are digitalized by six constant fraction discriminators (CF1 to CF6), then OR-combined and the resulting pulse is increased in width to 10 μs by logic gate L4. This time window is the coincidence time of the veto. The second (timing-) output of the germanium detector is first shaped by a timing and filter amplifier and then digitalized by a constant fraction discriminator (CF7). The digital, fast negative NIM, signals of the germanium detector

and the plastic scintillation detectors are then AND-combined. Therefore the output “gate signal” of the active veto shielding is produced only when there is a signal from the germanium detector to be gated off. The digital spectroscopy amplifier used requires the gate signal to overlap the Flat Top section of the shaped signal by a minimum amount of 0.5 μ s. To guarantee this overlap also in the presence of jitter, the gate pulse is extended to 5 μ s by logic gate L2. Because the Flat Top starts about the amount of the Rise Time later than the fast signal from the constant fraction discriminator CF7, the gate signal from the AND-combination has to be delayed by 12.3 μ s to symmetrically overlap the Flat Top using logic gate L3.

All seven constant fraction discriminators used (CF1 to CF7) and the OR-combination of the six channels used for the plastic scintillator plates are performed with a single width NIM module (ORTEC CF8000). The delays, width extensions and AND-gating are done with a quad logic gates, single with NIM module (ORTEC CO4020) containing L1 to L4. Each of the four independent logic gates can be used for all four logic functions AND, NAND, OR, NOR. The single shot at the output can be configured to trigger on falling or rising edge and the width of the output signal can be adjusted in the range from 40 ns to 40 μ s. The delay of the gate signal to overlap the Flat Top at the right time is realized by extending the width of the AND output to the required delay time and then triggering on the falling edge in the next input stage. In addition to the constant fraction and the logic NIM-module, a simple 50 m RG58 coaxial delay cable, an ORTEC 474 timing and filter amplifier, an ORTEC 556 HV power supply and a CANNBERA 1481 rate meter are used.

2.3 Time spectroscopy to optimize the time-window

The length of the time window for coincidence is an important parameter when setting up an active shielding. After the detection of a muon, all signals from the detector are discarded during this time span. Making the time window longer causes more gammas to be removed, but it also increases the probability for random coincidences and the additional dead time associated with it.

The muon flux and the radioactive decay in the sample on the detector are not correlated. Therefore the additional dead time is just the sum of all time windows and can be expressed as a percent value t_D in % by the product of the length of the time window t_w in seconds and the rate of detected muons per second r_μ .

$$\boxed{t_D[\%] = t_w \cdot r_\mu \cdot 100} \quad (1)$$

In general, the duration of the digital signal triggered by the germanium detector, which is AND combined with the veto signal (time window), has to be considered too and should be added to the time window for the calculation of the dead time. Since it is only 100 ns for the system discussed here, it could be neglected compared to the 10 μ s time window. It is important to note that the additional dead time does not depend on

the sample count rate, because the radioactive decay in the sample is not correlated to the muons in the cosmic radiation. For the system under discussion with $r_\mu = (350 \pm 100)$ muons/s and $t_w = 10 \mu\text{s}$, equation 1 gives an additional dead time of about 0.4 %. This additional dead time just decreases the efficiency of the detection system and has no other negative effect on sample measurement, as long as there is no variation of the muon rate over time.

To find the best compromise for the system under discussion, a multi channel scalar (MCS) was used to acquire a time spectrum of the time difference between the digital signals from the plastic scintillators and the germanium detector. The MCS (ORTEC MCS pci) was started with the signal from the plastic scintillator and stopped with the signal from the germanium detector. Figure 2 shows the distribution of time differences Δt between the plastic scintillator and the germanium detector. This time spectrum was acquired in a 20 day period.

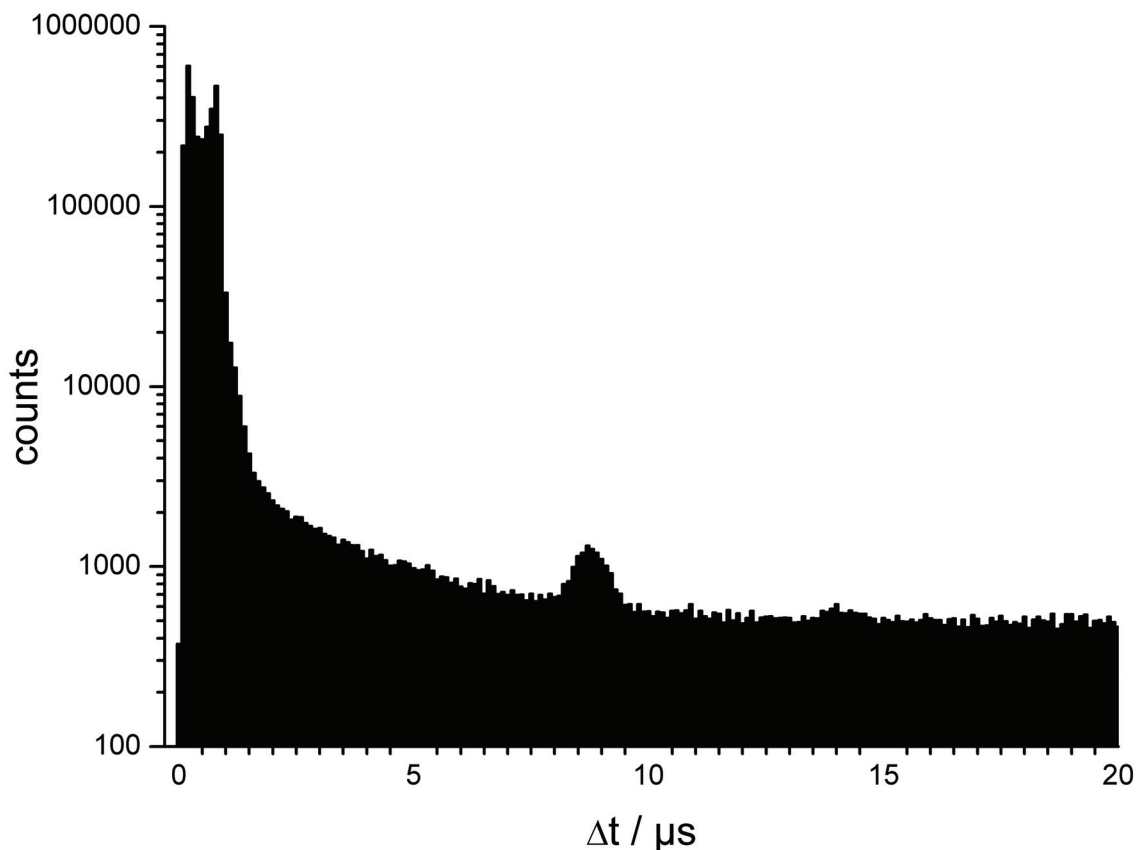


Fig. 2. Distribution of time differences Δt between plastic scintillator and germanium detector.

The two main peaks demonstrate that most of the gamma radiation caused by muon impact on the shielding is registered within the first microsecond. Between 1 and 10 μs appears a continuum with a peak at 8.8 μs . From 10 μs to the end of the time range of the MCS-measurement of 6.5 ms, only time un-correlated gamma background has been observed.

From this time-spectrum it was deduced that the optimal time window is 10 μs , because no gammas correlated to the veto-signal could be detected after this time. This is shorter than usually given in the literature - for instance Laurec et al. (1996) report to use a few hundred microseconds, Reeves (1988) and also Vojtyla (1994) have used 100 microseconds. Heusser (1991) found at least 10 μs to be necessary to cancel all delayed muonic events.

The peak in the time spectrum in figure 2 at 8.8 μs could only be explained by a physical delayed process, since an excitation process would give an exponential decay and not a peak. It is possible that the delayed signal it is caused by neutrons produced at the impact of the muon and than backscattered from the surface to the detector. Further investigations are in progress.

Figure 3 shows a comparison of the background without and with veto. Both spectra were normalized to an acquisition real time of one week. The background suppression ratio in the energy range 20-2700 keV is (9.0 ± 0.1) . The integral count rate in this region of the background with active veto is $(362 \pm 1) \text{ h}^{-1}$.

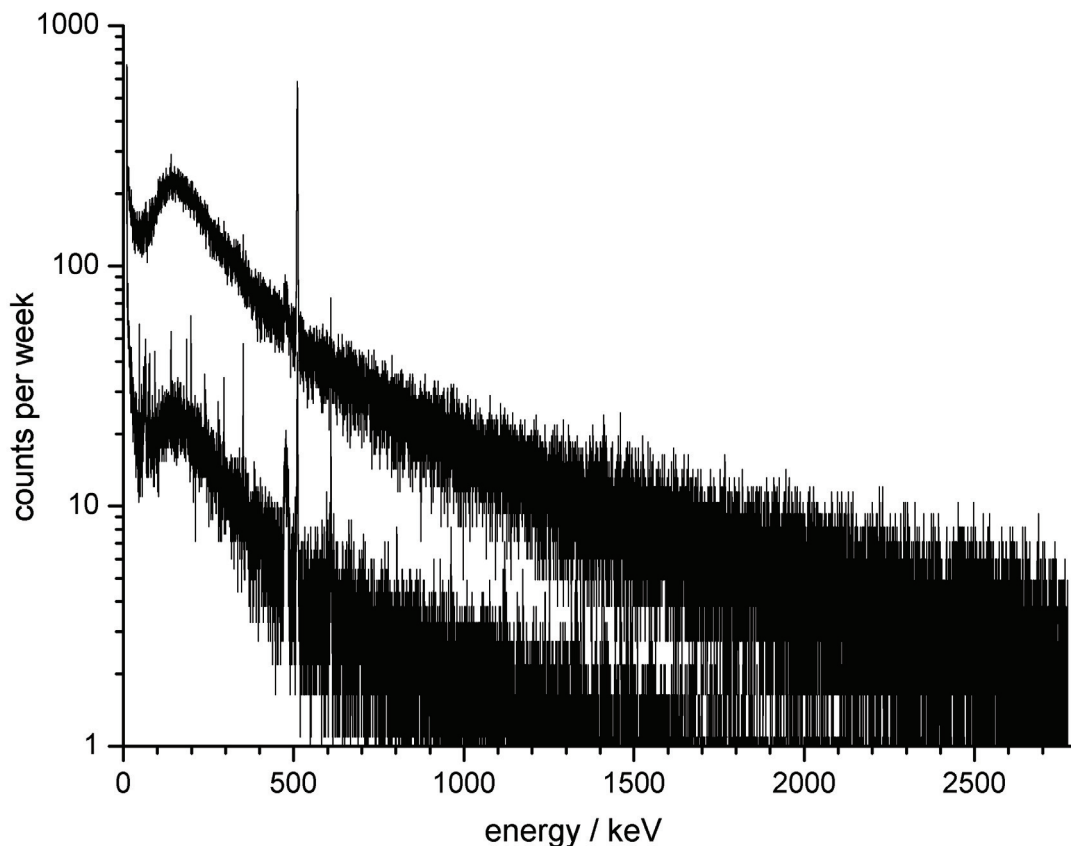


Fig. 3. Background Spectra without and with veto.

2.4 Countermeasures against electromagnetic interference

Before optimization, the baseline of the preamplifier was so noisy, that the noise threshold of the veto had to be set at about 40 keV, causing the veto to not suppress energies below this limit. The measurement range of the detector used goes down to 10 keV so it was reasonable to enlarge the suppression range to lower energies.

Originally, the power line in the laboratory was connected directly to a central uninterruptible power supply (UPS) unit, which also supplies all other laboratories in the research center. This power line is noisy and there are a lot of interferences due to the many loads disturbing the line, such as heavy motors, transformers and switching power supplies. In addition to this internal noise, there is also radio frequency pick up of interferences due to the long wires from the central UPS unit to the laboratory.

Measurements were performed to locate the way of propagation of the electromagnetic interference, since it was not clear whether the transmission path is through cables or wireless.

The interference at the preamplifier output was employed to trigger the scope and a ferrite transformer was used to measure the signals in the cables connecting to the laboratory (power line, network, phone, fire alarm). The noise could be identified as symmetric interference between two of the three phases, which increasingly turns into an asymmetric signal due to parasitic capacities between the conductors and ground. Therefore also the ground conductor was affected by the interference, such that ground had to be isolated also.

To block the interference from the power line, a totally isolated power net for the laboratory was designed. An uninterruptible power supply, which always runs in AC-DC-AC mode, rebuilds a sinusoidal waveform (harmonics below 3 %). To obtain total galvanic isolation, a transformer at the output of the UPS is used. The UPS is capable of driving 6 kVA so that it can supply the whole laboratory. By Austrian law, the neutral conductor has to be connected to ground to enable the use of a ground leakage circuit breaker, which is mandatory. However, in the isolated power net of the laboratory both conductors are equivalent and neither of them is connected to ground so that the line voltage is not related to ground. This is only allowed because an electronic monitoring system for phase to ground faults on both conductors has been installed, which alarms the electrical maintenance service in case of a connection between ground and one of the conductors. In this case, the other conductor would become phase and could be a serious hazard for electric shock. To avoid interference caused by loads inside the isolated power net, computers and other electronic devices were equipped with EMI-filters to block interferences generated in these devices. The filters were designed so that also the ground conductor is filtered, to attenuate not only symmetrical but also asymmetrical interferences. Figure 4 presents a circuit diagram of one of these filters.

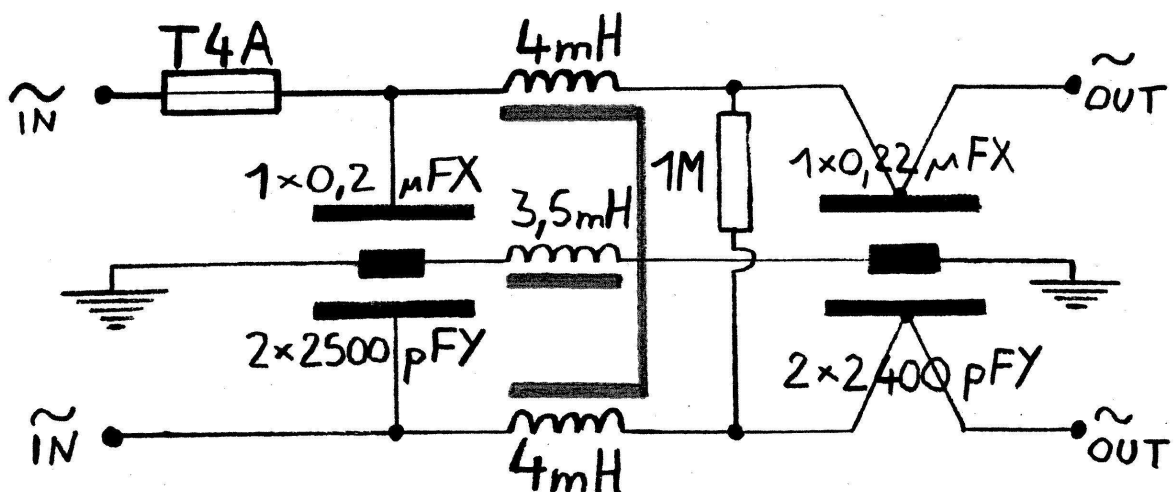


Fig. 4. Circuit diagram of the EMI filters used.

After all these measures, the interferences at the power line have disappeared and the waveform is visibly more accurately sinusoidal with less harmonics.

2.5 Discussion

When the efficiency calibrations are performed with the veto turned on, the additional dead time affects the calibration and the sample measurement in the same way. However, a variation in the muon flux due to fluctuation in the intensity of the cosmic radiation would lead to a proportional change of the associated dead time and efficiency of the system. In the system under discussion the optimum time window found, was so short that the associated dead time could be neglected regardless of possible changes in the muon flux.

When longer dead times are used, the muon flux could be monitored and dead time losses corrected. For a constant flux during measurement or when only long living nuclides are measured this could be done by the pulser method or by using a scalar to count the actual number of employed gate pulses during a spectrum acquisition and correcting the associated dead time. Changing muon flux during measurements of short living nuclides would make it necessary to do these calculations after several short time intervals like it is done in the loss free counting dead time correction method (Westphal, 1982, 1985). The problems related to the use of long time windows lead to the common use of short coincidence times in active veto shielding systems. The choice of the length of the time window is therefore always a compromise of maximum veto effectiveness and minimal additional dead time.

2.6 Conclusion

The measures described improved the overall performance of the active veto shielding and gave an experimental base for the choice of the value for the time-window, which was adjusted before by theoretical considerations only. The optimum coincidence time of 10 μs , found for the system under discussion matches the results obtained by Heuser (1993) who has measured the background count rate in dependence of the duration of the veto signal in the range from 1 μs to 1.8 ms.

When optimizing the electronics of the system, it turned out that improving resistance to electromagnetic interference of the electronics is in conflict with safety regulations.

3 Enhancing sensitivity of portal monitoring at varying transit speed

Abstract

The sensitivity of a portal monitoring system has been improved by introducing speed dependent integration time in the data processing of the count rate signal. Characterization and first tests have been performed using a pneumatically driven ^{137}Cs point source, before deploying the system to a test point at a railway junction near Vienna. At 14 m/s the MDA could be reduced by a factor of two and at 28 m/s by a factor of three compared to a fixed integration time of 1 s, whereas high sensitivity at low speed remained unaffected.

Keywords: train monitoring, portal monitoring, high transit speed, speed-dependent detection algorithm, signal to noise ratio, integration time, sensitivity, minimum detectable activity

3.1 Introduction

In this work the effect of integration time on the sensitivity of a portal monitoring system has been quantified. A single pillar of a typical polystyrene based portal monitoring system has been characterized by measuring the quantum efficiency as a function of the source position. These efficiency functions have been used to calculate the dependence of the minimum detectable activity (MDA) on integration time for different geometries and transit speed. In general, these MDA-functions can be used to select the optimum integration time for a certain measurement situation. Results will be applied to control the automatic variation of integration times adjusting it to an object's transit speed. This method can improve sensitivity in applications with varying transit speed. The implementation of the speed dependent signal processing has been tested under laboratory conditions by using an automatic source transport system, at various transit speeds up to 44 m/s. The system was extended to a combination of six pillars, deployed and tested at a railway junction near Vienna.

3.2 Motivation

Portal monitoring systems using a fixed integration time are only optimized for a certain transit speed. Higher or lower speed degrades the signal to noise ratio (SNR) and the

detection capability. Therefore, only a fixed (slow) transit speed is allowed in most installations. When a wider range of velocities and higher transit speeds are required, variable speed dependent integration time can be used to maintain optimum sensitivity. It has been investigated, how speed dependent signal processing can improve the detection capability of portal monitors at higher and varying speeds. The net signal level increases with the size (efficiency) of the detector and decreases with rising transit speed due to the shorter measurement time. Therefore, it is reasonable to pass the portal at slow speed to increase the detection sensitivity and to reduce the costs for the detectors. Most applications follow this rule and, accordingly, the typical transit speed for scanning vehicles is about 2 m/s. Thus the monitors are placed at a gate or check-point where the vehicles pass at slow speed. Hence, most monitoring systems have been developed and optimized for rather slow speed and are not prepared for the scanning of fast objects. At higher speeds, usual portal monitoring systems lose sensitivity, not only because of the inferior measurement statistics but also because their signal processing algorithms are not intended to automatically adapt for higher transit speed. Most systems can be configured even for higher speeds, by shortening the integration time, but this reduces sensitivity at lower speeds. Therefore, the user has to decide on adjusting the system for a certain speed range. If higher and varying transit speed is required due to technical or economical reasons, more advanced signal processing is needed to reach the theoretical limit for sensitivity, as set by the measurement statistics. Such measurement situation can apply to underground trains or railway junctions, where heavy traffic load is observed, and vehicle slowdown to support the monitoring is very expensive or even impossible.

3.3 Concept and application of speed dependent signal processing

A common way to detect a source is to process the count rate signal from a detector and to trigger the alarm if the count rate exceeds a predefined level, based on the statistical fluctuation of the background. Typically, approximately four times the standard deviation of the background is used as threshold value. It is continuously updated by measuring the background. For this continuous comparison process, a fixed integration interval is selected according to the expected transit speed. Typical values are in the range of 1 s (see Presti et al., 2006; Ely et al., 2006; Schrenk et al., 2004). Selecting a too short interval, results in cutting off the signal, while a very long interval will integrate too much noise and weaken the signal. The optimum interval range should match the width of the signal peak, which narrows at increasing speed. To maintain optimum SNR, the new speed dependent algorithm varies the integration time, which is used to scan the incoming count rate signal. Before implementation of the algorithm, a single pillar of the monitoring portal has been characterized, using a laboratory test system. For a ^{137}Cs source passing the monitor, the quantum efficiency, depending on the position of the source on the track and on the off axis distance (OAD) of the detector to the

track, has been measured. These functions have been used to calculate SNR and MDA, depending on integration time and on the transit speed. An optimum integration time for a given transit speed can be found by determining maximum MDA and minimum SNR. In the given application, transit speed is measured for each object and used to calculate the optimum integration time. By filtering with the optimum integration time, the system integrates less background noise, without cutting off the signal too much. The intended application for fixed integration time processing is vehicle monitoring at constant (slow) speed. Under real conditions, monitoring occurs at varying speeds, especially in the acceleration phase of underground trains. For such applications, the integration time has to be continuously adapted to the changing transit speed during data processing. This requires that the data acquisition system continuously records transit speed, linked to the count rate data. To scale the integration time, a rough figure (30 % uncertainty) of the transit speed would be sufficient. The uncertainty of the speed measurement also influences the radioactivity measurement in the assessed object and unknown self-shielding of the object will also add uncertainty in the same order of magnitude.

3.4 Dependence of sensitivity on the chosen integration time

To reduce the statistical fluctuation and the noise, the count rate signal is filtered by averaging over the so called integration time. Typically, a certain number of smaller intervals are summed up and this process is repeated after shifting the integration interval. The width of the optimum integration time depends on signal width. Neither should the signal be cut off nor should any extra noise be integrated. The signal's shape depends on the source geometry (point vs. volume), the off axis distance of the detector to the track and the transit speed. Shorter duration is observed for point sources, small OAD and high transit speed. A fixed integration time offers good performance within a small range of transit speed, but at varying transit speed the sensitivity deteriorates.

3.5 Comparison with previous work

Past studies used different integration times for passing point sources at different constant velocities (Runkle et al., 2005). Several authors have already recognized the problem of varying speed and fixed integration time (Wahl et al., 2007, Ely et al., 2004). Recent work investigates the dependence of the minimum detectable activity on the integration time, source and detector geometry and transit speed. Although application to spectroscopic systems or energy windowing would be possible, we have chosen a simple gross-counting system for easier comparison and demonstration here. Other signal filtering methods, which are mathematically more sophisticated, like recursive digital filter, filtering with moving average or the time series concept have been investigated and compared by several authors (Presti et al., 2007; Fehlau, 1993) but are not

applied in a speed dependent way. Recently also artificial neural networks have been investigated for signal processing of radiation portal monitors (Kangas et al., 2008).

3.6 Experimental determination of the efficiency

The quantum efficiency of the detection system serves as basis for signal calculation of an object containing a radioactive source. It is a function of the object-position relative to the detector. For laboratory systems usually the ratio of detected photons versus emitted photons is used. A photon can be considered to be detected if measured in the full energy peak (peak efficiency) for spectrometric systems or if detected anywhere (total efficiency) for gross counting systems. Because the polystyrene based systems considered within this work do not have energy measurement capabilities, only the total efficiency has been used. In this study only one single pillar has been characterized, as the results can be easily scaled and linearly combined for a system of two or more pillars. This work has been focused on ^{137}Cs and to make the efficiency more meaningful, the ratio of the detected photons and the activity (instead of emitted photons) has been used. The efficiency has been measured as a function of the source position on the straight trajectory relative to the point closest to the portal. The measurement has been repeated for different off axis distances. This model corresponds to a vehicle or person passing the portal on a straight line parallel to the detector surface. To ease comparison, the functions displayed in the graphs have been scaled for 100 % maximum at the closest off axis distance. The absolute efficiency $\varepsilon_{(x)}$ can be obtained by applying the scale factors ε_0 from Table 1 in equation 2. After corrections for different detector sizes and OAD, the value is in good agreement with other results from measurement or Monte Carlo simulations (Ayaz-Maierhafer and DeVol, 2007; Nafee and Abbas, 2008; Siciliano et al., 2005; Stromswold et al., 2004). A theoretical derivation of the efficiency for parallel-piped detectors and comparison with literature values has been performed by Nafee and Abbas (2008).

Table 1

Experimentally determined parameters for the efficiency function of a single pillar.

measurement condition	scale factor ε_0 in cps per kBq	parameter p_1 in m	parameter p_2 in m
5 m OAD	0.236 ± 0.011	12.3 ± 0.1	0
3 m OAD	0.62 ± 0.04	8.0 ± 0.1	0
2.5 m OAD	0.77 ± 0.05	6.5 ± 0.1	0
1 m OAD	4.4 ± 0.4	3.3 ± 0.1	0
1 m OAD, shielded by 5 mm steel	4.1 ± 0.4	3.3 ± 0.1	0.22 ± 0.01

The first four rows show different off axis distances (OAD), the last row includes self-shielding effect, for the system under consideration the last term can be neglected so $p_3=\infty$.

3.7 Measurement methods and consideration of the uncertainties and error propagation

All uncertainties within this work are quoted at one sigma confidence interval. In close distance the uncertainty of source positioning adds the main contribution to the expanded uncertainty of the efficiency. In far distance the uncertainty of the background count rate becomes the dominating one, as the net signal reaches the background level. Visual inspection of experimental data fit has shown that the uncertainty of the fit can be neglected compared to the uncertainty of the measured data. Two types of measurement have been performed, static measurements to determine the quantum efficiency and dynamic measurements to test the implementation of the speed dependent signal processing.

3.8 Static measurement of quantum efficiency

In static measurements, a system of perpendicular lasers and a laser distance-meter have been used to determine the accurate source position. The measurements were performed by placing one of two ^{137}Cs reference point sources with an activity of (6.0 ± 0.3) MBq and (26 ± 2) MBq at different positions on the trajectory. Self-shielding of the source, sealed in a 2 mm diameter steel capsule (wall thickness 0.7 mm) was neglected as the aim of this study was to test the relative improvement by using speed dependent signal processing and not the absolute performance, which will strongly depend on many other factors, such as detector type and size or self-shielding of the object. The source was moved on a supporting wire along the trajectory. In static mode, the longer measurement duration for each point resulted in higher accuracy compared to dynamic mode. The results were used to plot efficiency functions, which formed the theoretical basis for calculation of the MDA and implementation of the speed dependent algorithms in the test system.

3.9 Dynamic measurement for testing implementation

For characterization of a single pillar and laboratory performance verification of the signal processing algorithm, a point source was used to simulate the signal from a passing train containing a source. A pneumatically driven source transport system has been designed to allow flexible operation, using different sources at various speeds, in the range from 1 to 50 m/s. The path of the source can be adjusted by positioning the pipe of the source transport system in the required way. Speed and position of the moving source is computer controlled by electronic pressure control valves and hall sensors. This allows testing of portal monitors at different speeds and off axis distances. The measured data were used for the development and optimization of the algorithm and for testing its implementation before deployment in field tests. This testing was necessary to prove data processing and speed measurement worked satisfac-

torily and reliably even at higher speeds. Figure 5 shows the test system used for characterization and verification of the algorithm.



Fig. 5. Source transport system for testing of portal monitors.

3.10 Semi-empirical fit of the data

The aim of data fitting was to obtain analytical functions for the efficiency, which can be easily integrated and used to calculate the net counts and the MDA for different transit speeds. This allowed comparing different algorithms for signal processing by calculating the response function of the portal monitor to different source geometry and transit speed. The data from static measurements were processed by using nonlinear least squares fitting. To keep the uncertainties of the data points equal, the time for the static measurement has been adapted within a range from 4 s for close points up to 360 s for distant ones. The basic function was derived by extending the quadratic reciprocity law by adding three terms to account for variation in the shielding thickness, detector response (or effective detector area) and the changing solid angle. The adjustment of the parameters allowed the fit-function, to follow the measured data precisely. The mathematical form of the function is based on theoretical considerations, while the parame-

ters were determined empirically by fitting the experimental data. The resulting parameters for the considered system are listed in Table 1. Uncertainties given in this publication represent a confidence interval of one sigma.

The semi-empirical function used to fit the efficiency is:

$$\varepsilon_{(x)} = \varepsilon_0 \cdot \frac{d^2}{d^2 + x^2} \cdot Abs \left(\sin \left[\tan^{-1} \left(\frac{p_1}{x} \right) \right] \right) \cdot e^{-\left(\frac{\sqrt{d^2 + x^2} \cdot p_2}{d} \right)} \cdot \left\{ 1 - e^{-\left(\frac{\sqrt{d^2 + x^2} \cdot p_3}{d} \right)} \right\} \quad (2)$$

where $\varepsilon_{(x)}$ is the efficiency at position x along the source path, ε_0 is the efficiency in cps/kBq at closest distance ($x=0$), d is the OAD in m and p_1 , p_2 , p_3 are empirical parameters determined from the fit of experimental data. This function has been derived by application of the quadratic distance law and the exponential absorption law, under consideration of the geometry. Trigonometric functions have been introduced, to account for the increase of self-shielding (shielding thickness) and the increase in detector efficiency (detector thickness). Derivation and physical meaning is explained in following paragraph. The variables d and x are real distances, whereas the parameters p_1 , p_2 and p_3 are fitted empirically. Figure 6 shows the geometry.

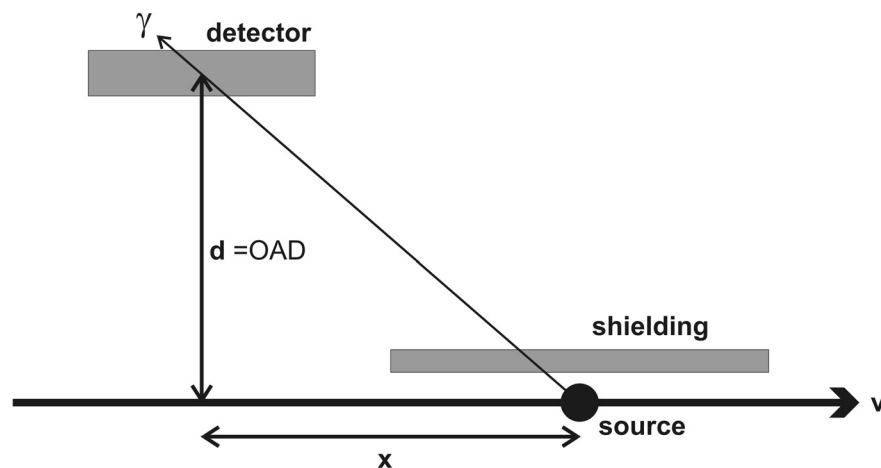


Fig. 6. Drawing of the geometry, the basis for equation 2.

The term containing p_1 accounts for the loss of effective detector area, when moving away from the detector. The sine and tangent functions can be replaced by their square root expression, to speed up integration time, but most numerical tools will do this anyway and the expression is easier to read without this substitution. The term

containing p_2 accounts for increased self-shielding of the object, due to reduction of the incident angle, when increasing the distance. The increase of the effective detector thickness, due to changing angle of incidence when moving away from the detector, is represented in the third term and parameter p_3 . In both cases the path length is increased by the acute incident angle. In contrast to the term containing p_2 , not the transmission but the absorption is taken into account. The parameter p_1 is related to the off axis distance d , p_2 is related to the product of linear attenuation coefficient and thickness of the detector and p_3 stands for the product of linear attenuation coefficient and thickness of the object-shielding. For the detectors considered in this study, the last term in curly brackets was heavily damped because of the 5 mm lead shielding on the sides of the portal monitor. Therefore, parameter p_3 has been set to infinity (term neglected).

Other simple mathematical models for the source count rate as a function of position or time can be found in Runkle et al. (2005) but have a more limited scope of application. The model presented here successfully follows the experimental data in a wide range and is able to adapt for changing off axis distances.

Figure 7 shows the relative efficiency dependence on the off axis distance (OAD) and shielding as a function of source position x , ranging from -2 to 21 m in a semi-logarithmic scale. The error bars indicate the measurement results, while the line represents the fitted function.

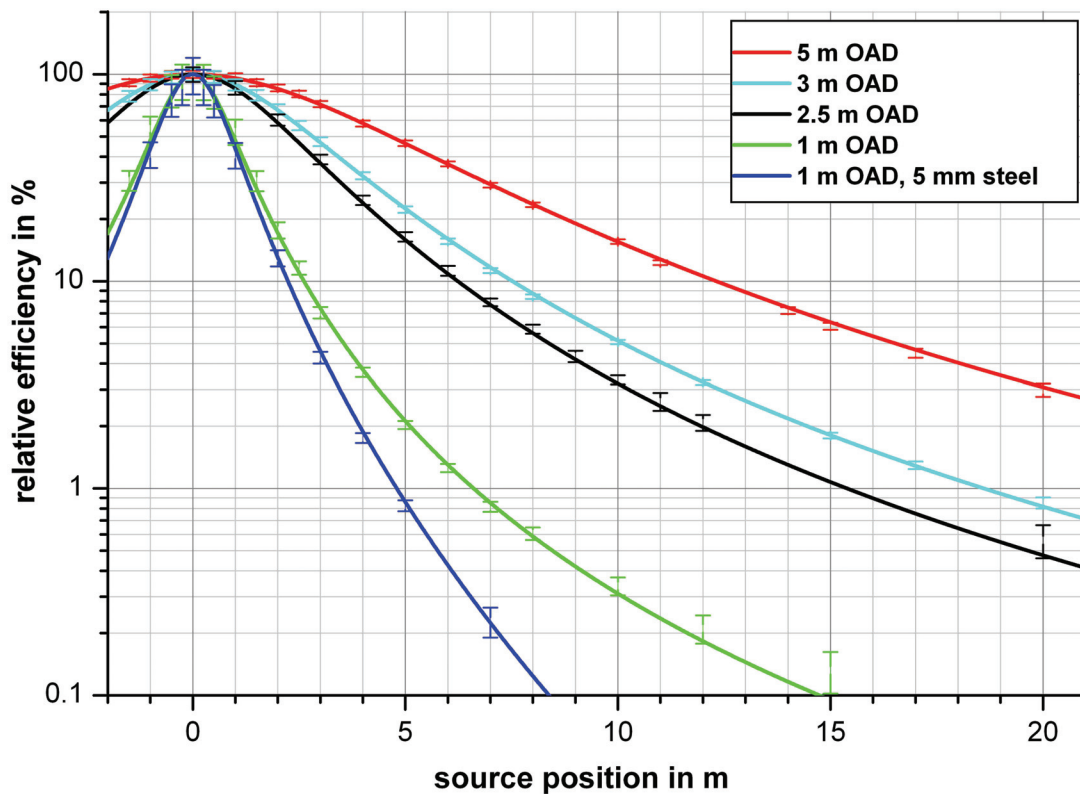


Fig. 7. Relative efficiency depending on off axis distance (OAD) and shielding as a function of source position x , ranging from -2 to 21 m, displayed in semi-logarithmic scale. These are measured points plus fitting function using equation 2.

3.11 Influence of the measurement geometry on the FWHM of the signal shape

When a source passes by a portal at a certain speed, the full width at half maximum (FWHM) of the signal variation in time is not only dependent on the off axis distances, but also on the shielding of the measured object. A similar effect, as for changing OAD, is also expected for a changing height of the source position within the portal's detection zone. In this study, this was not quantitatively investigated, as this information is not needed for the following calculations, which are all based on a fixed reference position (OAD=2.5 m) with the trajectory located at the level of detector reference position (center of detector). For standard portal monitoring situation, the smallest possible OAD will be around 1 m and the widest around 2.5 m, as there are normally two monitors opposite in typically 5 m distance for car and about 6 m for train monitoring. The range of possible source positions causes the range of signal width (FWHM) to span a

ratio of 1:3. As the detection probability for increased OAD decreases, integration time is optimized for these far objects rather than for close ones. If not stated, an OAD of 2.5 m has been used in all subsequent calculations and figures. The FWHM of the measured efficiency as a function of the off axis distance can be taken from figure 8, which shows the same function as figure 7, but uses linear scale and zoom factor for these purpose. When an object passes by, the FWHM is a measure for the length of the interval, inspected by the monitor at a certain point in time.

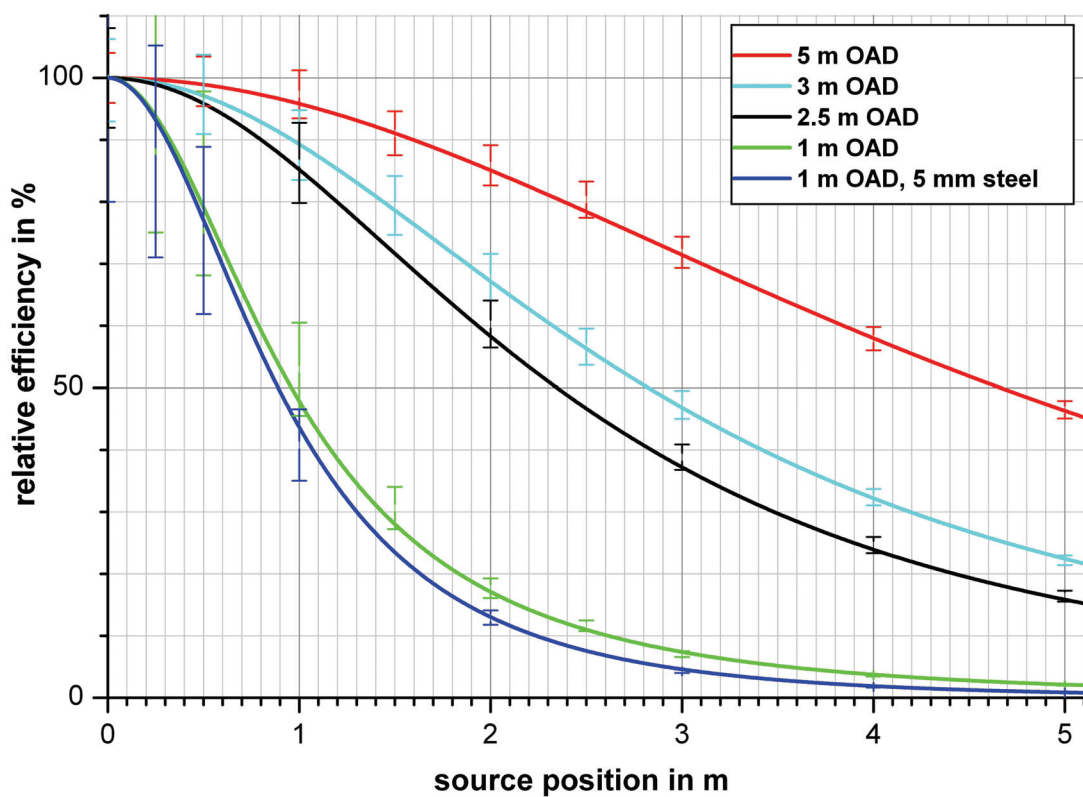


Fig. 8. Relative efficiency depending on off axis distance (OAD) and shielding as a function of source position x , ranging from 0 to 5.1 m, displayed in linear scale.

Table 2 presents the dependence of the signal FWHM on the geometry. The smallest signal is seen, if the OAD is short. Self-shielding of the object's walls leads to a shorter signal. Other shielding structures will have lower influence on the signal duration, but will also cause shadow shielding (Presti et al., 2006; Ely et al., 2006). A comprehensive investigation of shielding effects focused to cargo containers was performed by Schweppe et al. (2006).

Table 2

Influence of the off axis distances (OAD) and shielding on the FWHM of the signal.

measurement condition	FWHM in m	relative change of the FWHM
5 m OAD	9.3 ± 0.3	~ x 5
3 m OAD	8.4 ± 0.3	~ x 3
2.5 m OAD	4.8 ± 0.3	~ x 2.5
1 m OAD	1.9 ± 0.3	reference
1 m OAD, shielded by 5 mm steel	1.8 ± 0.3	- 5 %

Generally, systematic variations caused by shadow shielding are expected to exceed statistical fluctuations of the natural background (Ely et al., 2006). Systematic variations due to shadow shielding of vehicles passing by can cause 10-25 % drop of the count rate during occupancy (Presti et al., 2006; Stromswold et al., 2004). The magnitude and shape of the background modification varies between sites, lanes and panels. Therefore, it is difficult to include this effect into the mathematical model. Consequently, only statistical fluctuations have been considered, while the systematic fluctuations have been neglected for this comparison.

3.12 Calculation of the MDA for different integration times

To calculate the MDA, it is necessary to know the net signal of the source and the background signal within a certain integration time. The efficiency function derived before is multiplied by the activity to calculate the count rate. This function can be integrated on the path or over time, by using the transit speed of the object and time to substitute the position. So the net signal in the detector can be calculated for any integration time.

$$S_{NET} = 2 \cdot A \cdot \varepsilon_0 \cdot d^2 \cdot \int_{t=0}^{\frac{t_I}{2}} \frac{1}{d^2 + v^2 \cdot t^2} \cdot \text{Sin} \left[\text{Tan}^{-1} \left(\frac{p_1}{v \cdot t} \right) \right] \cdot e^{-\left(\frac{\sqrt{d^2 + v^2 \cdot t^2} \cdot p_2 - p_2}{d} \right)} dt \quad (3)$$

For calculation of the MDA the background was assumed to be constant and high enough to follow Poisson statistic. The measurement time of the background was assumed to be much longer than the integration time for the signal (well known background). The MDA has been calculated according to Currie (1968, 1984), by choosing a critical level (decision limit) based on an abscissa $k=4$ standard deviations (σ). This results in approximately 1 of 30,000 false positive alarms per test of an integration interval. An abscissa of $k=2$, which is normally used for MDA calculation, would cause about 5 of 100 decisions to result in a false positive alarm, which is unacceptably high

for portal monitoring applications. The probability of detection has been set to approximately 98 %, requiring 2 additional σ . Both choices reflect typical values for portal monitoring applications, but the absolute values are not critical, as the objective of these calculations is rather to investigate the relative sensitivity, than to calculate absolute MDA for a certain system.

3.13 Influence of varying integration time on MDA and critical level

The duration for an object's passage through a portal decreases at rising speed. Therefore, integration time is decreased in the speed dependent signal processing, too. The number of inspected integration intervals stays constant and also the detection probability and false alarm rate remain constant. In a classical fixed-integration time processing the number of inspected integration intervals would rise at decreasing speed. This would cause a slight rise in false alarm rate and the detection probability. To compensate for this effect, the critical level should be shifted up by increasing the first abscissa k_α above 4 σ ($\sim 4.5 \sigma$ for 10 times more testing). The effect on the MDA is partly compensated, because the second abscissa k_β for the MDA can be decreased below 2, to compensate for the simultaneously increased detection probability. k_α and k_β are abscissas of the standardized normal distribution corresponding to probability levels, $1-\alpha$ and $1-\beta$ (Currie 1968). The deviation, when neglecting this effect, is below 25 %. The mathematically exact solution would add Gauss-integrals into equation 3, reducing numerical evaluation speed and usability.

3.14 Signal and standard deviation at MDA level

The standard deviation at zero signal level σ_{LC} can be calculated from the background count rate r_{BKG} and the integration time t_i by $\sigma_{LC} = (t_i * r_{BKG})^{1/2}$. The standard deviation at a critical level σ_{LD} , elevated 6 σ above the background, can be approximated by $\sigma_{LD} \sim [6 * (t_i * r_{BKG})^{1/2} + t_i * r_{BKG}]^{1/2}$. The deviation, when using the simplification of 6 σ without the second term, is below 15 %, provided that the background exceeds 20 counts within the selected integration time t_i . Using this assumption, the signal at the MDA level is elevated 6 σ above the background. From the detection limit L_D , measured in counts, which is 6 times the standard deviation of the background, the MDA as activity can be calculated by substitution of equation 3, which links activity to count rate.

$$L_D \approx 6 \cdot \sigma_0 = 6 \cdot \sqrt{t_I \cdot r_{BKG}} = S_{NET,MDA} \quad (4)$$

$$A_{MDA} = \frac{3 \cdot \sqrt{t_I \cdot r_{BKG}}}{\varepsilon_0 \cdot d^2 \cdot \int_{t=0}^{\frac{t_I}{2}} \frac{1}{d^2 + v^2 \cdot t^2} \cdot \text{Sin} \left[\text{Tan}^{-1} \left(\frac{p_1}{v \cdot t} \right) \right] \cdot e^{-\left(\frac{\sqrt{d^2 + v^2 \cdot t^2} \cdot p_2}{d} \right)} dt} \quad (5)$$

where A_{MDA} is the minimum detectable activity in Bq, r_{BKG} is the background count rate in cps, v is the speed of the object in m/s and t_I is the integration time in s. The basics for the calculation of the MDA can be found in Currie's (1968, 1984) papers, a detailed illustration of the mathematical background is provided by De Geer (2004).

3.15 Influence of the integration time on the MDA

Generally, the MDA's dependence on the integration time can be plotted using equation 5. The empirical parameters p_1 , p_2 , p_3 and the scale factor ε_0 are determined by fitting the measured data. The background during measurement for the fit of the data was around 1000 cps; this value has been used in the following numerical calculations.

3.16 Optimum integration time

For a single pillar, the MDA as a function of integration time is plotted in figure 9. The graph shows a minimum of the MDA depending on the speed of the object. This minimum depends also on the off axis distances and is influenced by self-shielding of the object. For the selected cases the minimum has been numerically calculated and plotted as function of the object speed. The lowest MDA corresponds to the highest sensitivity of the system. Therefore, the optimum integration time can be deduced from figure 9 by looking at the minimum of the MDA for a certain speed and reading the integration time.

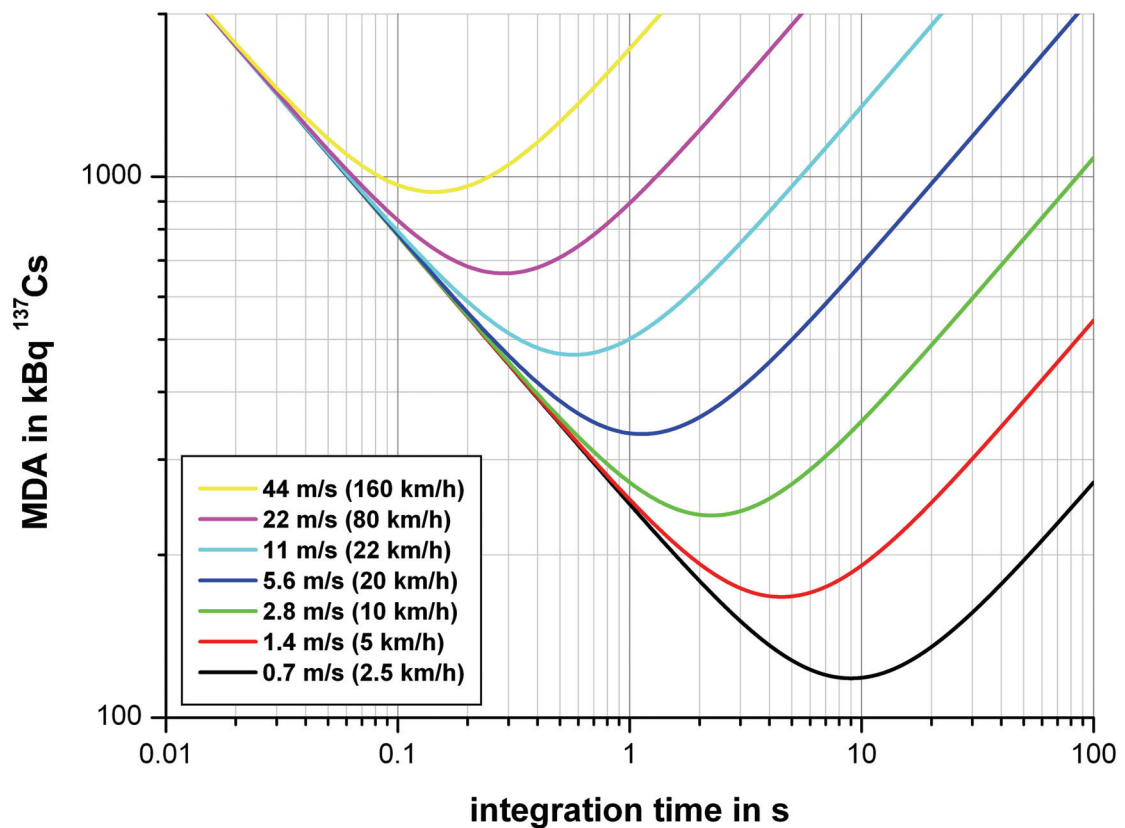


Fig. 9. MDA depending on the integration time (off axis distances 2.5 m).

In speed dependent systems the adaptation of the integration time according to the speed follows the graph. For systems with fixed integration time the graph can help to find a good compromise for the integration time. In figure 10 the dependence of the optimum integration time and the MDA on the speed have been plotted. Both functions were obtained by calculating the minima of the MDA function (the ordinate of figure 9) and plotting this and the corresponding integration time (the abscissa of figure 9), depending on the transit speed. Both functions have been transformed into straight lines by using semi logarithmic scale.

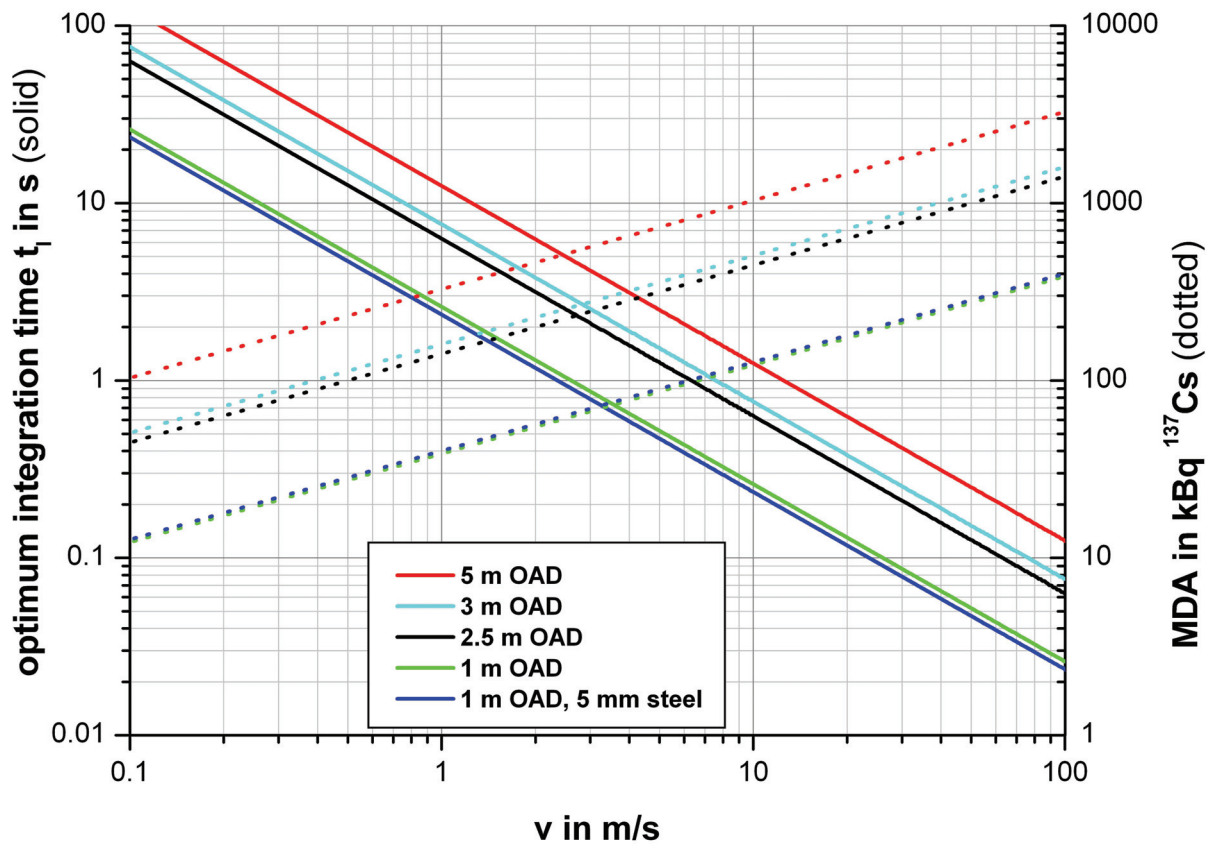


Fig. 10. MDA in kBq depending on object speed and according (optimum) integration time.

3.17 Calculation of the signal to noise ratio

Like the MDA, the *SNR* can be used as measure for the sensitivity. It is defined as the ratio of the net signal (*SIG*) and the noise coming from the statistical fluctuations of the background (*BKG*) and the noise from the signal itself (equation 6). Because of the Poisson nature of both variables, their variances add together under the square root:

$$SNR = \frac{SIG}{\sqrt{BKG + SIG}} \quad (6)$$

Both the signal and the background depend on integration time. The maximum of the *SNR* corresponds to an optimum of the integration time, see figure 11. The maximum is also dependent on the activity; for higher activity the signal is larger and exceeds the noise for longer time.

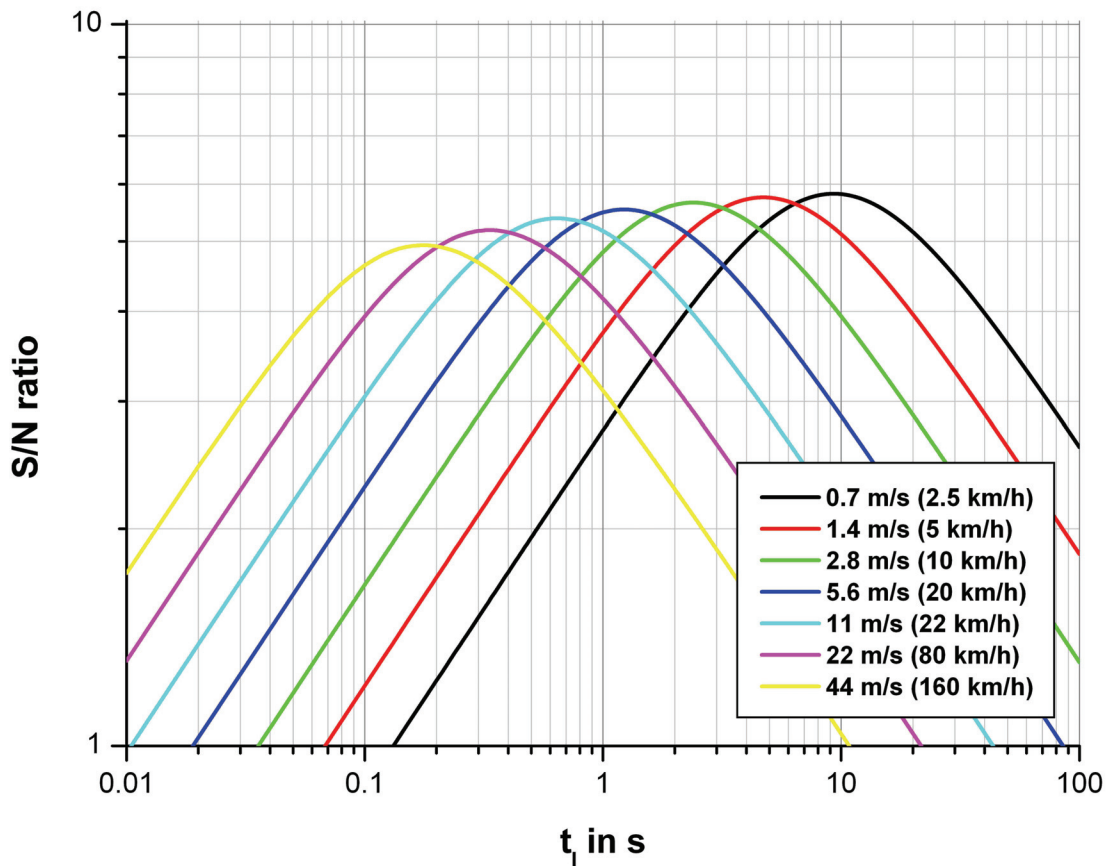


Fig. 11. SNR (signal to noise) as function of the integration time for various speeds, at 2.5 m OAD (off axis distance) and for the according MDA (minimum detectable activity).

For meaningful results the activity of the optimum MDA according to the speed and geometry has been applied. The SNR can be calculated for any signal strength. To allow a comparison of the MDA considerations with the SNR considerations, the SNR has been calculated, by setting the signal level to that of the minimum of MDA, corresponding to the speed. These MDA values are obtained by taking the minima of the MDA in figure 9. As this requires prior MDA calculation, the SNR can only be used to confirm the optimum integration time derived from the MDA. Equation 6 can be evaluated by substitution of the signal SIG with equation 3 and by calculation of the background from product of the integration time t_I and the background count rate r_{BKG} :

$$SNR = \frac{A \cdot \varepsilon_0 \cdot d^2 \cdot \int_{t=0}^{\frac{t_I}{2}} \frac{1}{d^2 + v^2 \cdot t^2} \cdot \text{Sin} \left[\text{Tan}^{-1} \left(\frac{p_1}{v \cdot t} \right) \right] \cdot e^{-\left(\frac{\sqrt{d^2 + v^2 \cdot t^2} \cdot p_2 - p_2}{d} \right)} dt}{\sqrt{t_I \cdot r_{BKG} + A \cdot \varepsilon_0 \cdot d^2 \cdot \int_{t=0}^{\frac{t_I}{2}} \frac{1}{d^2 + v^2 \cdot t^2} \cdot \text{Sin} \left[\text{Tan}^{-1} \left(\frac{p_1}{v \cdot t} \right) \right] \cdot e^{-\left(\frac{\sqrt{d^2 + v^2 \cdot t^2} \cdot p_2 - p_2}{d} \right)} dt}} \quad (7)$$

This function has been plotted in figure 11 for various speeds, with the activity set to the optimum MDA calculated before. The maxima show the optimum integration time for each transit speed, as a higher SNR results in higher sensitivity. Figure 12 shows the influence of rising activity on the maximum of the SNR, which leads to slightly rising optimum integration time, as illustrated in figure 13. Figure 14 shows the dependence of the optimum integration time on the speed based on SNR considerations and has to be compared to figure 10, which shows the same dependency derived from MDA calculations. Figures 13 and figure 14 contain graphs for various OAD.

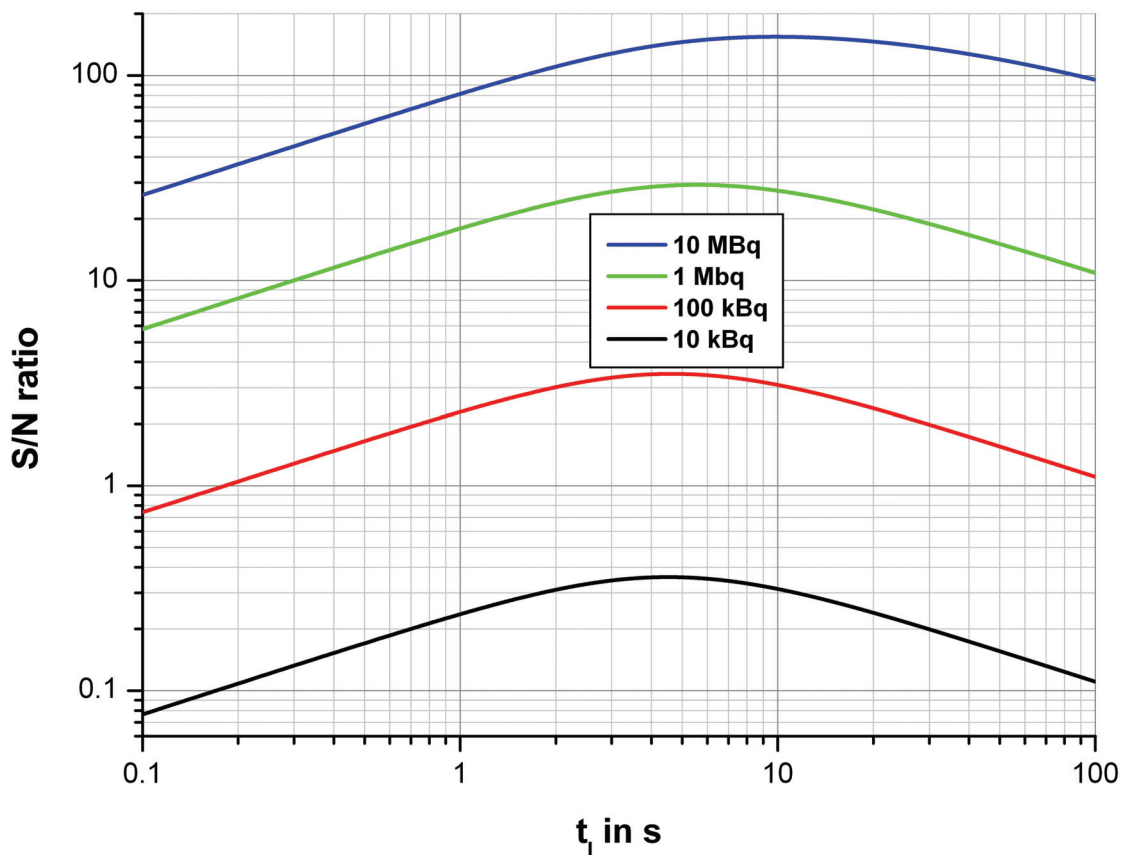


Fig. 12. SNR as function of the integration time for different ^{137}Cs activities, at 2.5 m OAD and for 1.4 m/s (5 km/h).

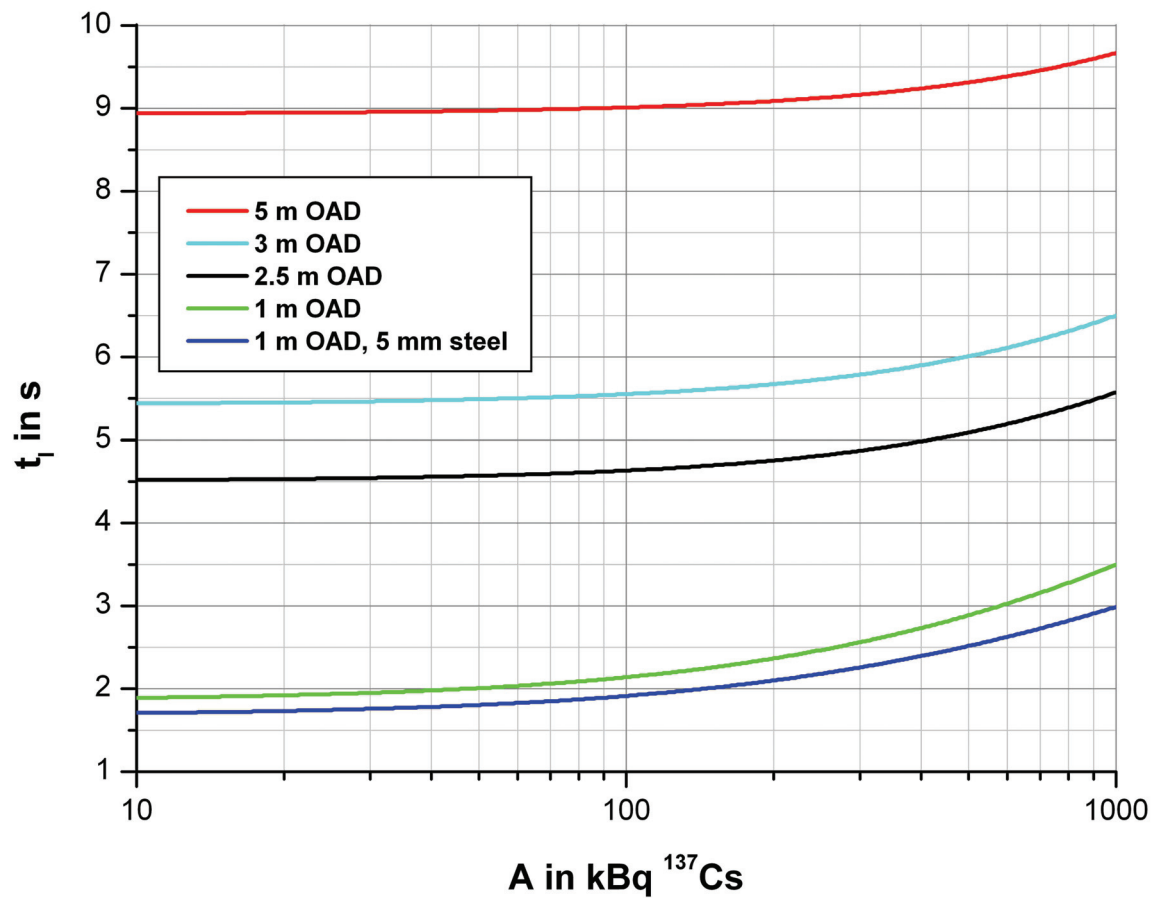


Fig. 13. SNR-optimum integration time (t) depending on ^{137}Cs activity (A), at a speed of 1.4 m/s (5 km/h).

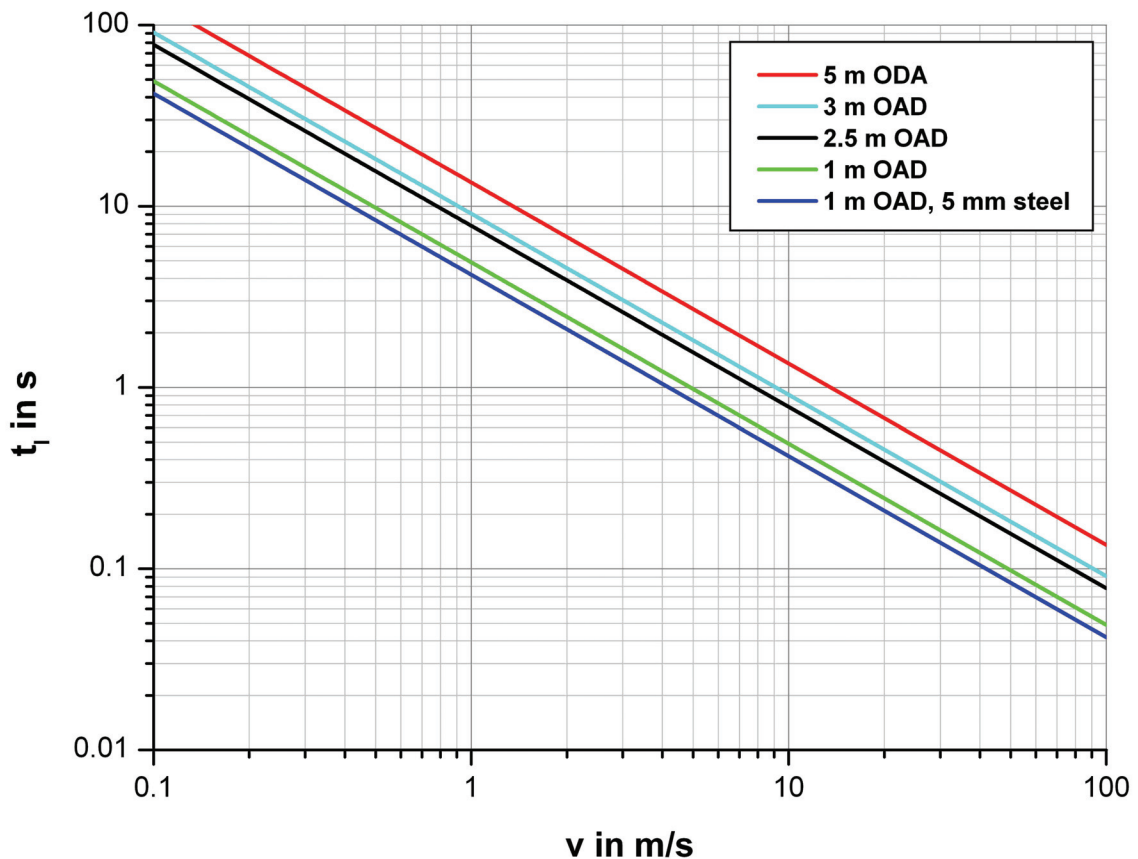


Fig. 14. SNR-optimum integration time depending on the speed (v), for an activity of 1 MBq ^{137}Cs .

3.18 Comparison of optimum MDA vs. optimum SNR consideration

The SNR considerations do not include an assumption on the false alarm rate or detection probability as required for MDA calculation and so both cannot be compared directly. This is not a contradiction, because even under optimal SNR conditions there is no guarantee to detect the signal. The results from the SNR considerations are useful to investigate how the signal behaves at higher activities and how this affects the integration time. The comparison of optimum integration time, derived from the MDA calculation presented in figure 9, 10 and from the SNR calculations in figure 12-14, showed little differences, increasing with smaller OAD. As figure 14 is based on a fixed activity of 1 MBq, whereas figure 10 is based on the respective MDA according to the speed and geometry, there are discrepancies for the smaller OAD, where the MDA is much lower than 1 MBq. Figure 13 illustrates this effect of rising activity on the optimum SNR and integration time.

3.19 Use of speed dependent signal processing in combination with other advanced processing methods

The method tested here can be combined with other methods and algorithms. To discriminate NORM (Ely et al., 2006) and to mitigate shadow shielding (Presti et al., 2006; Ely et al., 2006), energy windowing can be easily complemented with speed dependent signal processing (SPSP). In applications with strongly varying transit speeds, sensitivity can be further increased. More complex methods like matched filtering, weighted nonlinear least squares (Runkle et al., 2005) or recursive digital filtering (Fehlau, 1993) can be extended too, but require more mathematical effort. The S/N ratio can be optimized not only by choosing the best integration time, but also by filtering of the signal (Wahl et al., 2007). Both reduces the noise and can increase the S/N ratio and the sensitivity of the system, accordingly. Due to the more advanced mathematics, filtering by smoothing gives better results. Another important aspect of signal processing includes the choice of the alarm threshold. A detailed investigation of different alarm criteria using injection studies has been presented by Burr et al. (2007).

3.20 Application of the system for train monitoring

Six polystyrene based pillars, providing a total detector volume of about 138 l, have been installed and daisy-chained at a railroad track near Vienna. The train's speed is assumed to be constant and is measured inductively by two Frauscher wheel sensors. The signals from the portals are delayed and synchronized according to the transit speed of the train. Analysis and Monte Carlo simulation of the system showed that summing up the signals of the six portals and applying the source detection algorithm on the sum leads to better sensitivity than applying the algorithm to each independent portal and later combining the alarms. The new algorithm for processing and decision making has been implemented using C++. The system adapts the integration interval according to the width of the signal peak and scans for sources by moving this interval over the measured data. Before field installation, the system was tested at the Seibersdorf test site using the computer controlled source transport system.

To validate operation, different point sources have been packed into small containers for transport of dangerous goods and passed through the monitoring system mounted in a dedicated train at various speeds between 10 km/h and 120 km/h. The test location, where the six portal monitors were installed, was already equipped with measurement systems for acoustic noise, mechanical condition of axles and wheels of the train wagons. Our system has been designed to prove measurement availability at higher transit speeds and to get an initial estimate of the quantity of radioactive goods transported by train within Austria. Figure 15 shows the test system near Vienna consisting of six daisy chained pillars. The personal computer for signal processing, speed measurement and decision making is located in a small hut close to the detectors. Data are stored locally and periodically transferred to a central server.



Fig. 15. The monitoring system near Vienna consisting of six daisy chained portals.

3.21 Comparison of conventional and speed dependent signal processing

To test the sensitivity of the speed dependent signal processing, the detection capability for a point source at various speeds has been compared against a common configuration using a fixed integration time of 1 s, which is a typical choice. For a 60 kBq ^{137}Cs source passing by in 1 m distance, the choice of 1 s gives an optimum S/N ratio at a speed of about 5 km/h. The off axis distance of 1 m has been selected as a convenient geometry for the comparison and does not reflect any assumptions on the expected source position in an application. For laboratory testing of the measurements system, a source of about 6 MBq ^{137}Cs has been passed by the portal monitor at an off axis distance of 1 m using different values of constant transit speed. From the signal of the source and the background, the MDA has been derived. Table 3 presents the MDA for a generic ^{137}Cs point source at different speed for different integration times. The table is calculated for one pillar (23 l polystyrene) located in 1 m OAD to the trajectory; shielding of the vehicle (rail car) has not been considered. The highlighted elements in the table show that speed-dependent signal-processing provides the optimum MDA,

even for higher speeds, whereas the fixed integration time of 1 s is optimized only for a speed of 5 km/h.

Table 3

Dependence of the MDA on the integration time at various speeds

speed		MDA in kBq depending on the integration time							
in km/h	in m/s	10 ms	25 ms	50 ms	100 ms	250 ms	500 ms	1 s	3 s
5	1.4	440	278	196	140	91	71	64	81
10	2.8	440	278	198	142	100	90	100	156
20	5.6	440	280	201	151	127	141	182	305
50	14	318	288	223	200	239	318	442	761
80	22	446	302	256	266	363	500	703	1215
100	28	450	315	283	314	449	314	886	1521
160	44	465	362	376	468	708	994	1403	2430

3.22 Conclusion and Interpretation

Our tests successfully demonstrate that speed dependent signal processing can improve the detection capability of portal monitoring at higher speeds. At 50 km/h the MDA can be reduced by a factor of two and at 90 km/h by a factor of three compared to a fixed integration time of 1 s. A possible improvement of the sensibility is dependent on parameters like source position and self-shielding of the vehicle, which should be further investigated in subsequent studies.

4 Methods to sustain energy calibration in low level gamma-ray spectroscopy

Abstract

Two methods to compensate the gain drift of low level gamma-ray spectrometers are compared. For a period of 4 years, source injection and pulser method have been applied in parallel. The long term stability of a reference peak, injected by a precision pulser, has been validated by periodical source injection to sustain the energy calibration. The pros and cons of both methods and the advantage of active vs. passive energy calibration are discussed. The main cause for gain drift and the critical components have been identified.

Keywords: energy calibration, low level gamma-ray spectroscopy, gain stabilization, electronic drift, reference peak, pulser, gain stabilizer, detector QC

4.1 Introduction

4.1.1 Accuracy and stability of energy calibration

Sustaining an accurate energy calibration is essential for the analysis of spectroscopic gamma-ray measurements (Debertin and Helmer 1989). The required accuracy depends on the complexity of the spectra and the aim of the analysis. This study is focused on high resolution systems, typically utilizing HPGe-detectors. In case of a known nuclide vector, when only a few known key nuclides are surveyed, an accuracy of about one keV may be sufficient. If complex fission and activation spectra are investigated, given the requirement to identify all present radionuclides, the accuracy of the energy calibration should be close to the uncertainty of the peak position, below some tenth parts of a keV (Attrep and Kahn 2007).

In recent literature, different approaches to investigate and sustain the energy calibration of high resolution gamma-ray detectors have been published. Automated methods have been used for gain-matching (calibration) of segmented or composite germanium detectors by Hu et al. (2002), Stézowski et al. (2002) and Pattabiraman et al. (2004). Application of orthogonal distance regression has been applied to refine and study the energy calibration (Hurtado et al., 2006). This method treats the measurement uncertainties more adequate resulting in a better fit of the calibration function. Automated library driven approaches have been realized by Likar and Vidmar (2002) by application of correlation technique. This approach offers automated calibration even after measurement and is especially suitable for in situ measurement and emergency situa-

tions. The current study is focused on testing and practical implementation of methods to sustain the energy calibration of low level gamma-ray spectroscopy systems.

4.1.2 Concept of energy calibration used in the experiment

Energy calibration can be performed in an active (adjusting the system gain) and passive (fitting the calibration function) way. Typically the first step is the active coarse calibration of the electronic gain (defining the energy range), followed by the passive calibration, the determination of the mathematical relation of the energy as a function of the channel number. The compensation for drift can be done either in a passive or active way. The periodical measurement of a reference source is frequently used to determine the deviation (drift) of the energy calibration and if a certain limit is exceeded, the mathematical relation is recalculated to respond to the peak shift. It is easier to implement this passive calibration as it requires no adjustments of the electronics. For the active calibration the (electronic) system gain is adjusted to sustain the fixed mathematical calibration function. The advantage of active recalibration is that an arbitrary function can be selected, deployed and sustained at all detectors within a laboratory. In this study we have chosen the reference energy calibration function to be 0.17 keV/channel. Due to deviant second order coefficients of different spectrometers, the finally applied first order coefficients differ slightly to obtain the best possible match with the reference calibration. This method provides not only stable energy calibration within time but also uniform calibration of different spectrometers within a laboratory. For analysis of low level background spectra, this facilitates direct summing and comparison of spectra without transformations. Not only all spectra of one spectrometer, but also spectra of different spectrometers can be summed up to improve statistics and to assess and identify background peaks. This permits long term comparison and combination of background spectra, as the energy calibration can be sustained over years and reestablished even after system shutdown or major service interventions.

4.1.3 Spectrum stabilization by a reference peak

If there are sufficient strong background lines present, they can be utilized for calibration and stabilization. This is typically done for in-situ measurement or hand-held instruments; sometimes small artificial sources (such as ^{137}Cs) are embedded in the detector to produce a reference peak. The background of a low level spectrometer shows only very small peaks and for statistical reasons the stabilizer function of the spectrometer cannot lock on these. The use of an additional source would deteriorate the sensitivity, as its Compton continuum increases the background. Such a source can only be introduced temporarily to perform energy calibration between sample measurements. A suitable method to introduce a reference peak permanently is, to couple a sufficient stable tail pulser to the test input of the preamplifier (pulser method). The stability of the reference peak depends on the drift of the pulser and the coupling network, which consists of the cable connection, termination resistor and coupling capacitor located in the

cryostat. Of these components the capacitor is the one most difficult to control, as it is located within the vacuum cryostat. In this work the performance and practicability of the permanent pulser method and the temporary injection of radioactive sources has been compared.

4.2 Methods

One aim of this study was to investigate the achievable accuracy of the spectrum stabilization by a reference peak by a long term (4 year) comparison of the pulser method with the injection of a radioactive source (source injection method) being the reference method.

4.2.1 Source injection method

Due to the inherent accuracy of reference sources, the source injection method provides most accurate energy calibration but requires periodical, manual intervention or the implementation of an automatic injection system. The advantage of this method is simultaneous monitoring of other relevant detector parameters as resolution and efficiency. Apart from energy calibration it provides a full detector quality control (QC) as required by good laboratory practice. During this study the performance of two similar full automated detector QC systems has been studied for a period of four years.

Automated source injection has been implemented by using a pneumatically driven pipe transport system. A diaphragm pump is operated in push and pull mode by toggle valves so that only one pipe has to penetrate the shielding. The source is sealed in a small (1.5 mm diameter, 5 mm length) stainless steel capsule, which has a plastic ball (POM) of about 4 mm diameter at each end to reduce friction and to facilitate flight through curved piping. The source activity of 9.5 kBq ^{60}Co is slightly below the governmental exemption limit. ^{60}Co has been chosen, as a compromise between high energy, long half life and availability. The source position is monitored by using an inductive proximity switch. The motion of the source is controlled by a programmable logic controller (PLC) which communicates with the spectrometer bidirectional by using the sample changer (ready) signals. Figure 16 shows a schematic drawing of the source transport system. The transport pipe is fed from the air-flow control unit to the source-shielding, containing an inductive proximity switch. It continues about 10 m to the detector-shielding. A bolt stops the source at each end and final position is retained by gravity. To avoid penetration of background gamma-radiation, the feed through the detector-shielding is V-shaped.

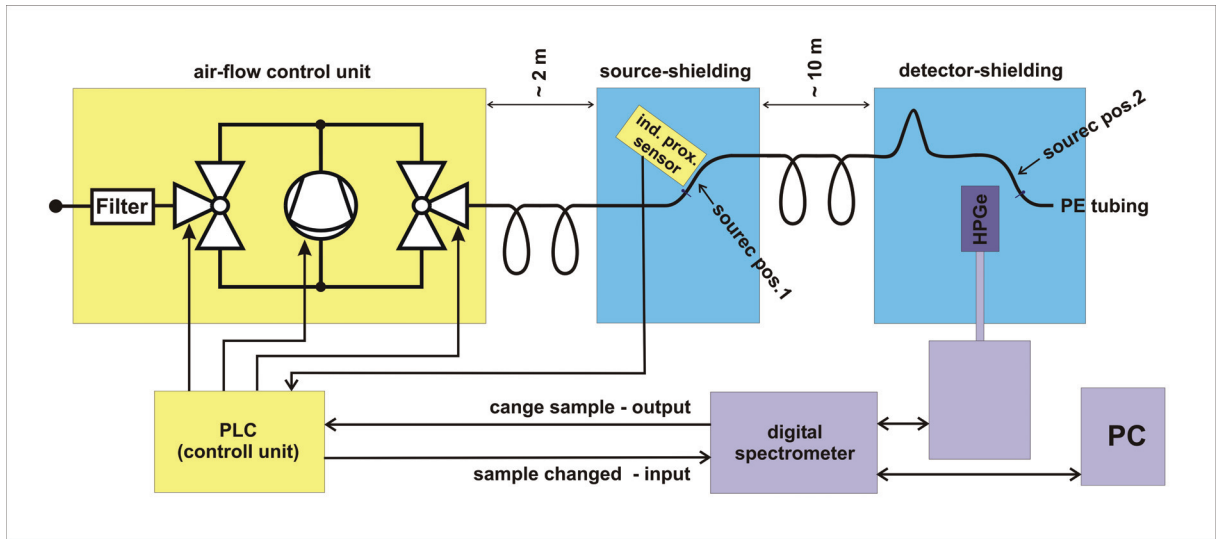


Fig. 16. Schematic drawing of the pneumatic source transport system.

4.2.2 Pulser method

A precision pulse generator (BNC, PB-5) has been used to maintain a reference peak at the end of the spectrum (around 2700 keV). The tail pulses have been directly injected into the test input of the preamplifier (Canberra 2002). Figure 17 shows the shaped signal of a gamma-ray (S1), the shaped signal of the pulser signal (S2) and the pulser signal injected into the preamp (P). Electrical connection is trivial, but the inevitable return of the pulser signal to the baseline generates negative components in the shaped pulse which perturb signal acquisition in the spectrometer. These negative components have been delayed behind the peak detection (capture) point, by introducing a flat top period in the pulser signal. The optimum pulser flat top time (delay of the negative component) depends on the shaping time (shaping rise time and shaping flat top) and has been adjusted experimentally by decreasing the pulser flat top time (delay) until beginning distortion of the peaks in the spectrum. For a signal shaping by 13 μs rise time and 1.1 μs flat top time the optimum of pulser flat top width has been found to be 15 μs . The rise and fall time have been set to their minimum values (0.05 and 0.5 μs). The resulting pulse shows a 15 μs flat period, after which it decays within about 5 μs (0.5 μs time constant). For the comparison in this study, the reference peak of the pulser has been processed in the same way as the reference peak from the ^{60}Co source, by fitting a Gaussian peak (including tailing) to determine exact peak location. Implementation of this method to sustain the energy calibration of a low level gamma-ray spectroscopy system could be done much easier by applying the gain stabilizer of the spectrometer on the (pulser) reference peak.

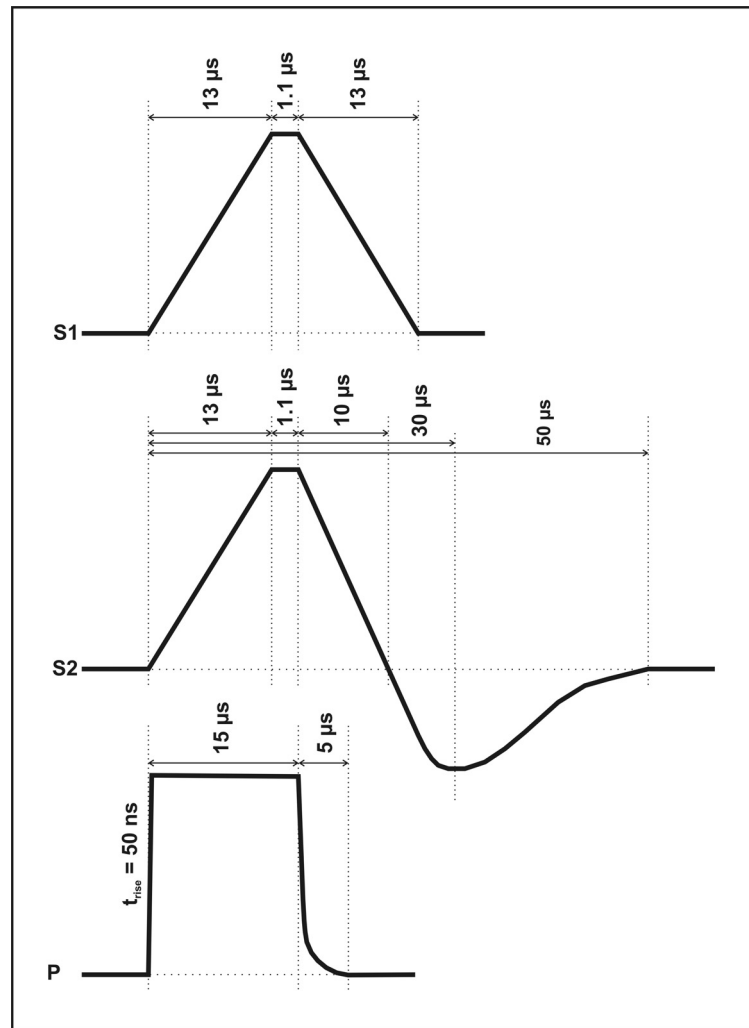


Fig. 17. Schematic signal characteristic of the shaped gamma ray (S1) and pulser (S2) signal and the pulse injected into the preamp (P)

4.2.3 Investigation of the possible causes for the drift of energy calibration

Another aim of this study has been to locate the reasons for the drift of the energy calibration. Therefore, a precision tail pulser (BNC, PB-5) has been directly connected to a digital spectrometer (ORTEC, DSPEC+) without a preamplifier. This setup eliminates the influence of the detector and the preamplifier, both suspected to be the major sources for drift. The amplitude drift of the pulser is sufficiently small (typically ± 20 ppm) compared to the observed drift of the whole spectrometer (around ± 100 ppm) to allow investigation of the drift sources. The digital spectrometer has been set up identically to the previous measurements with the HPGc detector. Only the pole zero has been adjusted to match the different return of the pulser signal

to the baseline. The pulser has been set up to imitate the signal from the preamplifier by injecting a long tail (100 μ s fall time) signal at a constant rate of 1 kHz.

4.3 Results and Discussion

4.3.1 Drift of offset and gain

The employed digital electronics (ORTEC, DSPEC+) exhibits sufficiently small drift of the offset and gain, but detector and preamplifier (Canberra 2002) still employ analog electronics. Any drift of the DC offset caused by the preamplifier or detector will be filtered out by the band pass filter of the spectrometer, whereas a drift of the preamp gain will directly influence the total system gain and cause peak shift. Therefore, for the systems under consideration, no check or correction of the offset is required and only the system gain has to be monitored and adjusted. Hence, only a single line, preferable at the high energy end of the spectrum has been used for gain stabilization.

4.3.2 Initial energy calibration

The offset has to be measured only once and is adjusted as close as possible to zero during installation. The remaining rest is considered by a constant in the energy calibration equation. Multiline calibration sources are used for this purpose since a long time (Blagojevic and Wood 1982). The spectrometers considered within this study are intended for measurement of low level samples and so the uncertainty of the peak location is limited to about 0.1 keV by statistics, but for higher activities much smaller deviation can be achieved. Reference data for energy calibration is available with uncertainties of less than 10 ppm. The data from 1979 has been revised and published by Helmer and van der Leun (1999, 2000). For short time, precise measurements can provide uncertainties as small as (1-10) eV (Helmer et al., 1978, Vanin et al., 1997, Helene et al., 1999) within a limited energy range. Precise investigations of the accuracy of the peak localization showed decay (count rate) dependent effects, as the accuracy is statistically limited by the peak fitting algorithms. Liu et al. (1999) reported these effects within a scale of 10 eV.

4.3.3 Long term study of the source injection method

Twice per day the actual measurement of the detector has been stopped and saved, before the ^{60}Co source was injected by the automated source injection method. Several measurements were performed, the fine gain adjusted and the results were documented automatically. After finishing of the service, the previous measurement was restored and measurement started again. Figure 18 shows the deviation of the energy calibration as it would be without adjustments (measured using the restored original fine gain). Over the four year period from June 2005 to June 2009 the measured deviation is ± 1.2 keV for the first (DET1-blue triangles) and ± 0.8 keV for the second (DET2-

green circles) detector under study. The first detector has been sent to the manufacturer for a LabSOCS calibration in 2008, causing a four month interruption of the graph. The ambient temperature (black stars) has been plotted for the last two years, to look for a correlation with the gain drift. Despite the low resolution of the temperature measurement, the correlation of gain and ambient temperature is clearly visible by the synchronous course of the graphs.

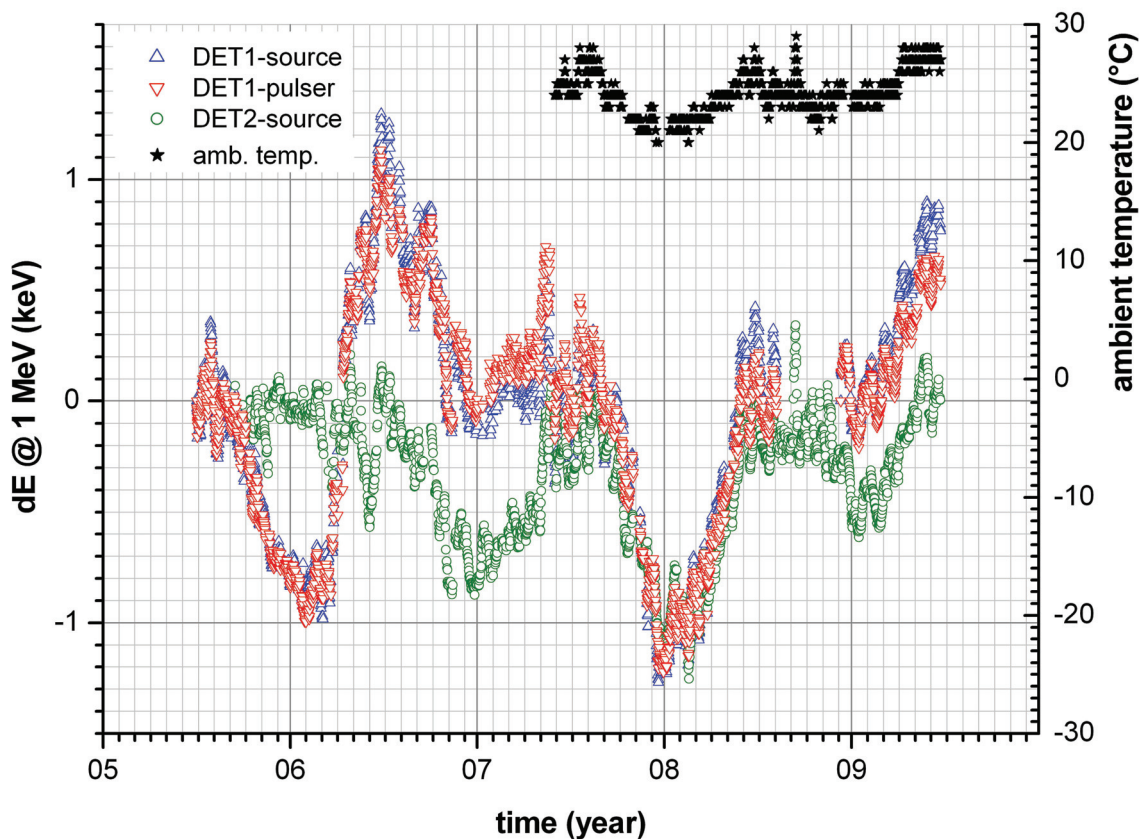


Fig. 18. Long term drift of two spectrometers measured by source injection and by pulser method, normalized at 1 MeV

4.3.4 Long term comparison of the pulser method

In the second part of the study, the inherent stability of the source injection method has been used to assess the stability of the pulser method. Although the pulser (BNC, PB-5) is stable within ± 20 ppm, the resulting overall stability also depends on the coupling network. To investigate the achievable stability, the pulser method has been compared with the source injection method, used as reference, for about four years. Figure 19 shows the drift of the pulser peak, normalized to 1 MeV, compared to the calibration

sustained by the source injection method. Statistical analysis gives a standard deviation of ± 0.1 keV and a maximum deviation of ± 0.3 keV at 1 MeV. The standard deviation of about ± 100 ppm goes considerably above the ± 20 ppm caused by the pulser showing that the coupling network is the main source for the observed drift. As the stability of the coupling network can deviate for different systems, it is recommended to prove its stability by using the source injection method in parallel, before practical implementation of the pulser method. If the measured stability is sufficient for the application, the pulser method can successfully replace the source injection.

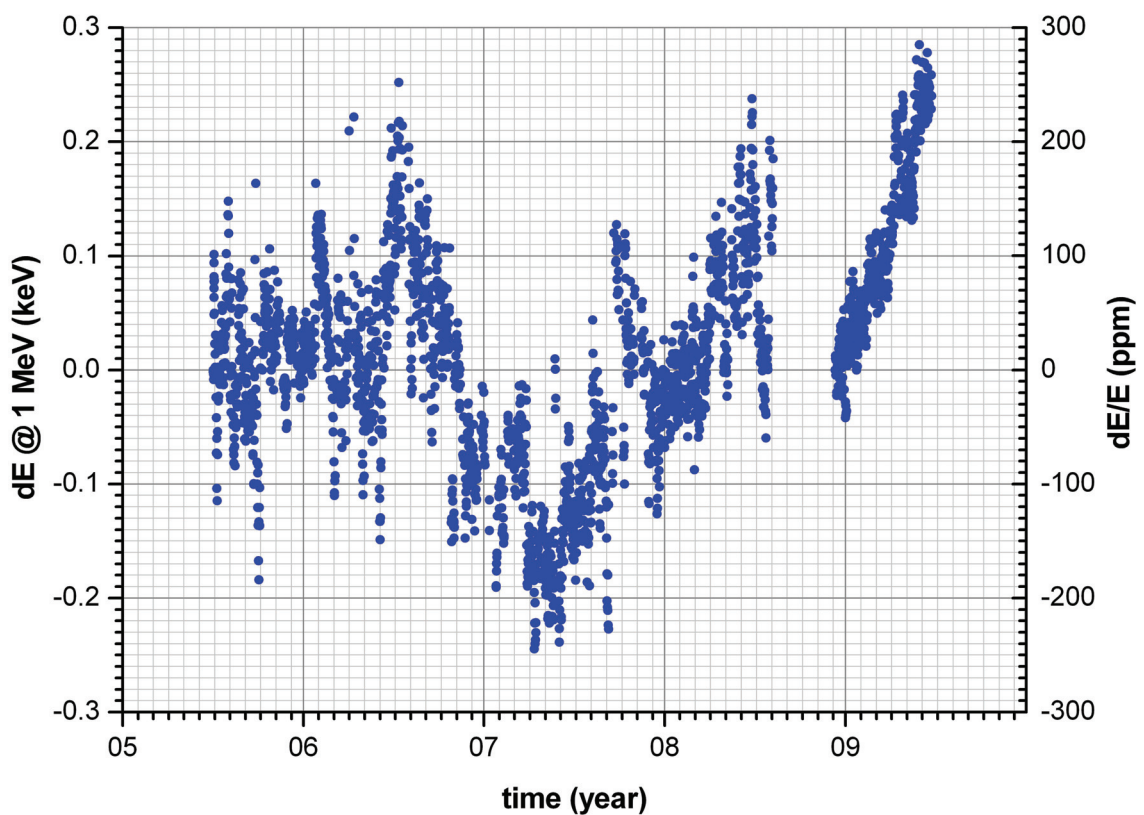


Fig. 19. Drift of the energy calibration, stabilized by pulser, normalized at 1 MeV.

4.3.5 Investigation of the causes for system gain drift

The investigation of the drift of the system gain should identify the cause for this phenomenon, which could be temperature, ambient pressure etc. and the affected component, which could be detector, preamplifier or spectrometer. As the detector and preamplifier were suspected to be the major drift sources, their influence has been eliminated by connecting a precision tail pulser (BNC, PB-5) directly to the digital spectrometer (ORTEC, DSPEC+). The drift of the pulser of ± 20 ppm is sufficient small,

compared to the gain drift of the complete spectrometer of about ± 100 ppm/K. The sole spectrometer has been configured (gain, shaping, etc.) identical to the two complete systems described and tested before. Figure 20 shows the drift of the gain (energy calibration) normalized to 1 MeV during a period of two months. The standard deviation is ± 15 ppm and the maximum deviation is ± 30 ppm. No correlation with the environmental temperature could be verified. The absolute drift of the spectrometer can be narrowed down below 20 ppm, as the observed ± 30 ppm are close to the drift of the pulser of ± 20 ppm. The deviation of the sole spectrometer is more than one magnitude below the deviation of the complete system, indicating that the detector and pre-amplifier are the main sources of the gain drift. The cause for the drift has been investigated by comparing the drift vs. the ambient temperature and air pressure. No influence of the ambient pressure could be verified, but the drift showed strong positive correlation with the ambient temperature, which is plotted in figure 18 (black stars). This can be seen from the parallel course of the ambient temperature (asterisks) and the deviation of the energy calibration of the three detectors (circles and triangles).

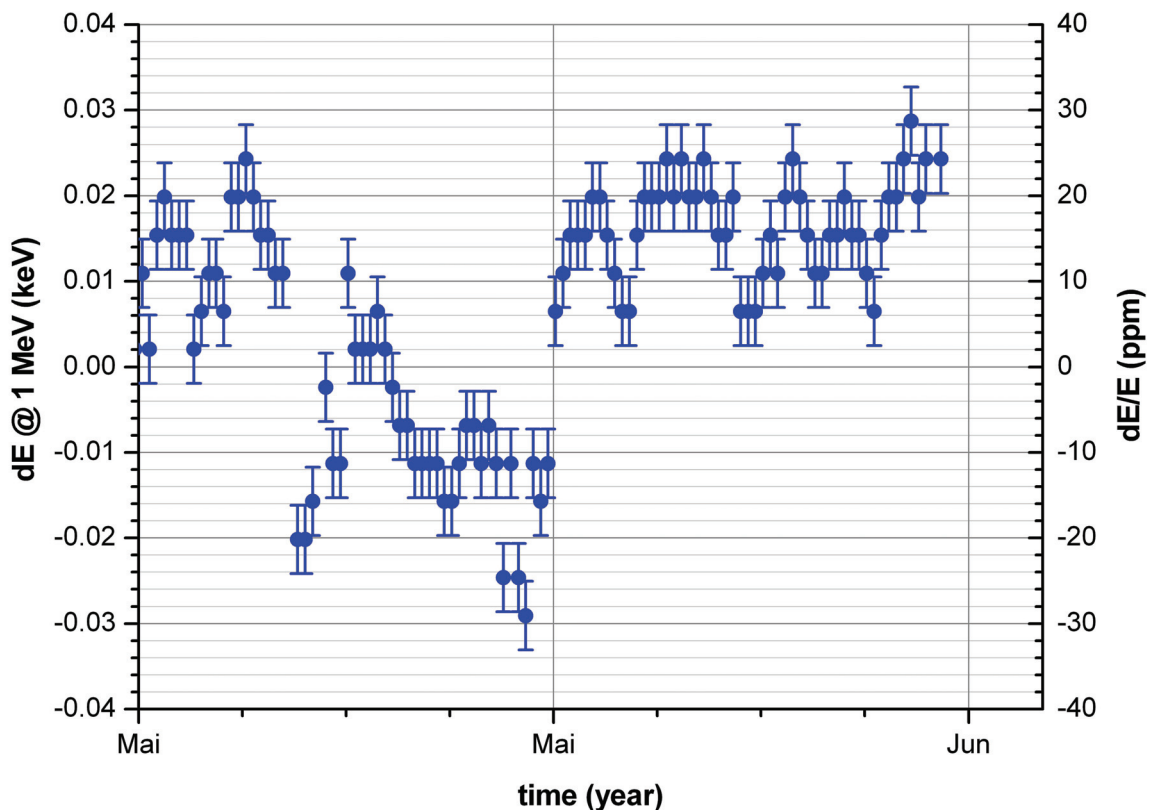


Fig. 20. Gain drift of the sole spectrometer, normalized at 1 MeV.

4.4 Conclusions

4.4.1 Accuracy and drift stability of the source injection method

When using this method, the error of the reference peak position is the major source of uncertainty for energy calibration. This observation can be derived from the known inherent drift stability of the radioactive source and the high accuracy of the reference data. Finally, this uncertainty will be increased by the uncertainty of the sample peak position, which is typically higher, because the smaller (low level) sample peak will exhibit poor statistics. As the same algorithm is used in both cases, the systematic uncertainty of both peak positions will partly cancel out. Therefore, this method provides the best achievable energy calibration. For the two spectrometers under study, the drift stability by application of the source injection method, showed a standard deviation below 10 eV (normalized to 1 MeV) corresponding to a change in gain of 10 ppm.

4.4.2 Accuracy and drift stability of the pulser method

The drift stability of the pulser method is limited by the drift stability of the coupling network (see discussion above) and will therefore deviate for different detectors. For the spectrometer under study the long term drift over four years of operation showed a standard deviation of ± 0.1 keV (100 ppm) and a maximum deviation of ± 0.3 keV (300 ppm) - both normalized to 1 MeV.

4.4.3 Advantages - pulser method

The advantage of the pulser method is its easy implementation. Care should be taken by setting up the pulser timing (rise, flat top, fall-time), as the reverse going signal should not disturb the shaping amplifier. Despite of this adjustment, the connection of the pulser to the preamp is easy and the signal can be split to supply several detectors. There is no need for additional hardware or software, as the available gain stabilizer can be used.

4.4.4 Advantages - source injection method

The advantages of the source injection method are inherent drift stability and the possibility to monitor other relevant system parameters such as resolution and detection efficiency, therefore providing a fully automated quality control measurement. As an option, a multi-radionuclide source or a multiline gamma-emitting radionuclide could be employed to cover a wider energy range and to provide offset check and stabilization. For the digital gamma-ray spectrometer considered in this study, the drift of the offset has been found to be negligible compared to the drift of the system gain and therefore only gain stabilization has been applied. However, the implementation of the source injection method requires a source transport system, modification of the detector shielding and development of software to control and monitor the process.

5 High resolution beta-gamma-muon (anti-) coincidence radioxenon measurement

Abstract

A high resolution β - γ coincidence measurement system has been developed by combining a high purity broad energy germanium and a silicon surface barrier detector. The system is intended for calibration of reference spikes and re-measurement of CTBT samples, by detection of coincident β - γ or conversion electron and x-ray radiation of the four radioxenon isotopes ^{131m}Xe , ^{133m}Xe , ^{133}Xe and ^{135}Xe . The use of a high resolution, list mode, multi parameter data-acquisition system allows off line setup and optimization of the (anti-) coincidence. A ^{166m}Ho β - γ source has been produced and validated for energy calibration and system check. The β - γ coincidence has been further enhanced by a cosmic myon veto based on six plastic scintillation detectors. The μ - γ anticoincidence has been implemented by using a 50 ns resolution real time clock for time spectroscopy. This method has been verified by running conventional TAC-ADC (combined time-amplitude & analogue-digital converter) based time spectroscopy in parallel. The whole measurement system has been characterized, by measuring various radioxenon spikes and backgrounds with and without (anti-) coincidence. Peak efficiencies and minimum detectable activities (MDA) for the main radioxenon isotopes have been determined. Application of μ - γ anticoincidence reduced the MDA by about a factor of two for all four radioxenon isotopes. Complementary adoption of β - γ coincidence further reduced the MDA for the metastable isotopes by more than an order of magnitude. The MDA for ^{135}Xe reaches about 6 mBq after one day of measurement. For ^{131m}Xe , ^{133}Xe and ^{133m}Xe a MDA of about 2 mBq is obtained after one week measurement.

Keywords: β - γ coincidence, μ - γ anticoincidence, high resolution, high purity germanium, silicon surface barrier, radioxenon, multi parameter, list mode, conversion electron

5.1 Introduction

5.1.1 Radioxenon measurement for treaty verification

The importance of radioxenon measurement in samples of atmospheric air or soil gases for verification of the Comprehensive Nuclear Test Ban Treaty (CTBT) (Hoffmann et al., 1999; Dahlman et al., 2009; UN 50/245, 1996; CTBTO-PTS, 1996) has been explained in detail by many authors (Bjurman et al., 1990; De Geer, 1996; Perkins et al., 1996; De Geer, 1996; Carrigan et al., 1996, De Geer, 2001; Auer et al., 2004; Saey and De Geer, 2005; Auer et al., 2009; Zähringer et al., 2009). The CTBTO detection network for radioxenon, part of the International Monitoring System (IMS) (CTBTO/WGB/TL-115/Rev.8, 2000; PrepCom, 2001; Wernsperger and Schlosser, 2004), consists of globally allocated stations for sampling and measurement (Bowyer et al., 1999, Bowyer et al., 2002), which are supported by laboratories. These laboratories are used for re-measurement of samples and for provision of reference spikes to facilitate quality assurance at the stations. The measurement is focused on four radioxenon isotopes, namely ^{133}Xe , ^{135}Xe , $^{133\text{m}}\text{Xe}$ and $^{131\text{m}}\text{Xe}$. In particular the isotope ratios are consulted to differentiate between the releases from nuclear power plants and weapon testing (Finkelstein, 2001; Miley et al., 2008). These isotopes decay with half lives between 9 hours and 12 days under emission of β -radiation or conversion electrons in coincidence with γ -radiation or characteristic x-rays (JEF-2.2, 1997, Be, 2004; Haas et al., 2008). Such coincident emissions have been utilized by different β - γ coincidence measurement systems for radioxenon (Reeder and Bowyer, 1998; Russ et al., 1999; Reeder et al., 1998; Luca et al., 2000). Adoption of delayed coincidence between β and conversion electrons ($t_{1/2}=6.4$ ns) can improve sensitivity and discrimination from ^{133}Xe against $^{133\text{m}}\text{Xe}$ (Reeder and Bowyer, 1998, Reeder et al., 2001). Most systems for coincident measurement have been designed by implementation of scintillation detectors (Bowyer et al., 1998; Ringbom et al., 2003; Cooper et al., 2007; Prelovskii et al., 2007). These detectors allow good resolution for the electron energy, but the resolution for the photons (γ and x-rays) is limited. The measurement system developed under this study combines a High Purity Germanium (HPGe) detector and a Silicon Surface Barrier (SSB) detector to obtain high energy resolution for electron and γ -radiation. The improved energy resolution for photons allows easier differentiation of the four radioxenon isotopes. While SSB detectors have already been used as electron detector (Lamaza, 1997; Lopes et al., 2003) and broad energy HPGe detectors as photon detectors (Le Petit et al., 2006; Zhang et al., 2009; Fontaine et al., 2004), the combination of these systems is a new and successful approach for improved radioxenon measurement.

5.1.2 Calibration of radioxenon spikes

The presented system is suited for re-measurement of xenon samples from the sampling stations and for calibration of reference spikes to be used for quality assurance at the stations. The higher complexity of the measurement system compared to conventional low level gamma spectroscopy with only HPGe detectors (Miley et al., 1992; Schulze et al., 2000; Schwaiger et al., 2002; Stocki et al., 2004) is justified by the better differentiation of the four radioxenon isotopes, allowing easier and more accurate quantification of reference spikes. For ^{131m}Xe the coincidence system allows absolute (direct) measurement of the activity, without previous efficiency calibration. Absolute measurement of ^{131m}Xe has also been used to verify the detection efficiencies.

5.1.3 Re-measurement of xenon samples from stations

The use of $\mu\text{-}\gamma$ anticoincidence for re-measurement of radioxenon samples consequently arises from previous application of this technique in gamma spectroscopy (Schroettner et al., 2004). Additional application of $\beta\text{-}\gamma$ coincidence results in higher sensitivity and better discrimination of the four radioxenon isotopes. Especially the sensitivity for the two metastable isotopes, which have rather low gamma emission probabilities, is considerably improved by detecting their conversion electron radiation.

5.2 Methods

5.2.1 High resolution $\beta\text{-}\gamma$ spectrometer

Within this paper, the terms beta, gamma include not only β and γ -radiation but also conversion electrons and characteristic x-rays. While application of β/γ coincidence for radioxenon measurement is a well established technique (Bowyer et al., 1998; Ringbom et al., 2003; Cooper et al., 2007; Prelovskii et al., 2007), the novelty of the present measurement system is the combination of two high resolution detectors and the extension by $\mu\text{-}\gamma$ anticoincidence. This leads to high resolution 3D spectra exhibiting very narrow peaks and an ultra low background of about one count per week in the region of interest.

5.2.2 Radiation detectors and preamplifiers

The electrons from β -decay or internal conversion are detected by a fully depleted silicon surface barrier detector (ORTEC 44108E) with a thickness of 1 mm and a circular

sensitive area of about 300 mm². The signal from the detector is integrated on a charge sensitive preamplifier (Amptek A250CF) which delivers a fast signal for timing and a slow signal for energy. To reduce the stray capacity and noise pick up of the connection cable, the preamplifier is located close to the detector, within the lead shielding. The γ and x-ray radiation is detected by a planar broad energy high purity germanium detector (Canberra BE5035) with a crystal size of 80 mm diameter and 35 mm height. Its relative detection efficiency according to IEEE 325 (IEEE 325-1996) is 52 %. The low level mounting features a carbon entrance window to reduce absorption of the xenon x-rays at 33 keV. The charge sensitive preamplifier (Canberra 2002CSL) is integrated into the cryostat and delivers two identical signals for the fast timing and the slow energy channel. Cosmic myons are detected by six guard detectors, which surround the lead shielding (Schroettner et al., 2004). These detectors are made of 50 mm thick plates of plastic scintillator and read out by a PMT with a hemispherical cathode. The anode signal of each PMT is adjusted and amplified by a fast amplifier (Phillips Scientific 777). Relevant detector specifications are summarized in Table 4.

Table 4

Detector specifications

	detector 1	detector 2	detector 3
radiation	β & conversion electrons	γ & characteristic x-ray	μ (cosmic radiation)
detector type	fully depleted SSB	planar broad energy HPGe	scintillation (plastic)
manufacturer, type	ORTEC, 44108E	Canberra, BE5035	BICRON, -
size of sensitive volume	300 mm ² x 1 mm	5000 mm ² x 35 mm	5 m ² x 50 mm
energy resolution (FWHM)	9 keV @ 45 keV	1.9 keV @ 1.3 MeV	-
time resolution (FWHM)	~ 50 ns @ 100 keV	~ 600 ns @ 30 keV, ~ 20 ns @ 1.3 MeV	~ 8 ns

5.2.3 Measurement cell

The measurement cell is designed to contain a sample gas volume of 4.6 ml at negative pressure compared to ambient. It is made of 99.99 % oxygen free electrolytic copper (type CU-OF-1 or CR/CW007A). This material offers an adequate compromise between the requirements for opaqueness, good electromagnetic screening (conductivity), low content of radionuclide impurities, good machining properties and costs. The bottom side of the cell consists of a carbon epoxy resin window, which adjoins the (carbon) window of the HPGe detector. The carbon window is clamped vacuum tight between two o-rings by a copper ring, which is bolted together with the main body of the measurement cell. The application of two carbon windows ensures a minimum absorption of the low energy characteristic x-ray photons. To maximize the detection efficiency, the SSB electron detector is placed in the middle of the sample cell. The electrical contacts are fed through by a vacuum tight LEMO 00 connector (type HGP.00.250.NTLPV), which is directly connected to the input of the preamp. The measurement cell can be flushed and charged by a self-locking stainless steel miniature-quick-connector (Swagelok SS-QM2-D-1PM). Besides these two connectors, there is an inside thread, in the center of the cell, which is sealed by a slotted head screw under normal operation. For energy calibration and system check this screw is replaced by the calibration source (see chapter "Energy calibration and performance test"). Figure 21 shows a schematic drawing of the measurement cell (copper parts in brown, SSB detector in golden, screw for calibration source in yellow, connectors and bolting in grey and carbon epoxy in black color).

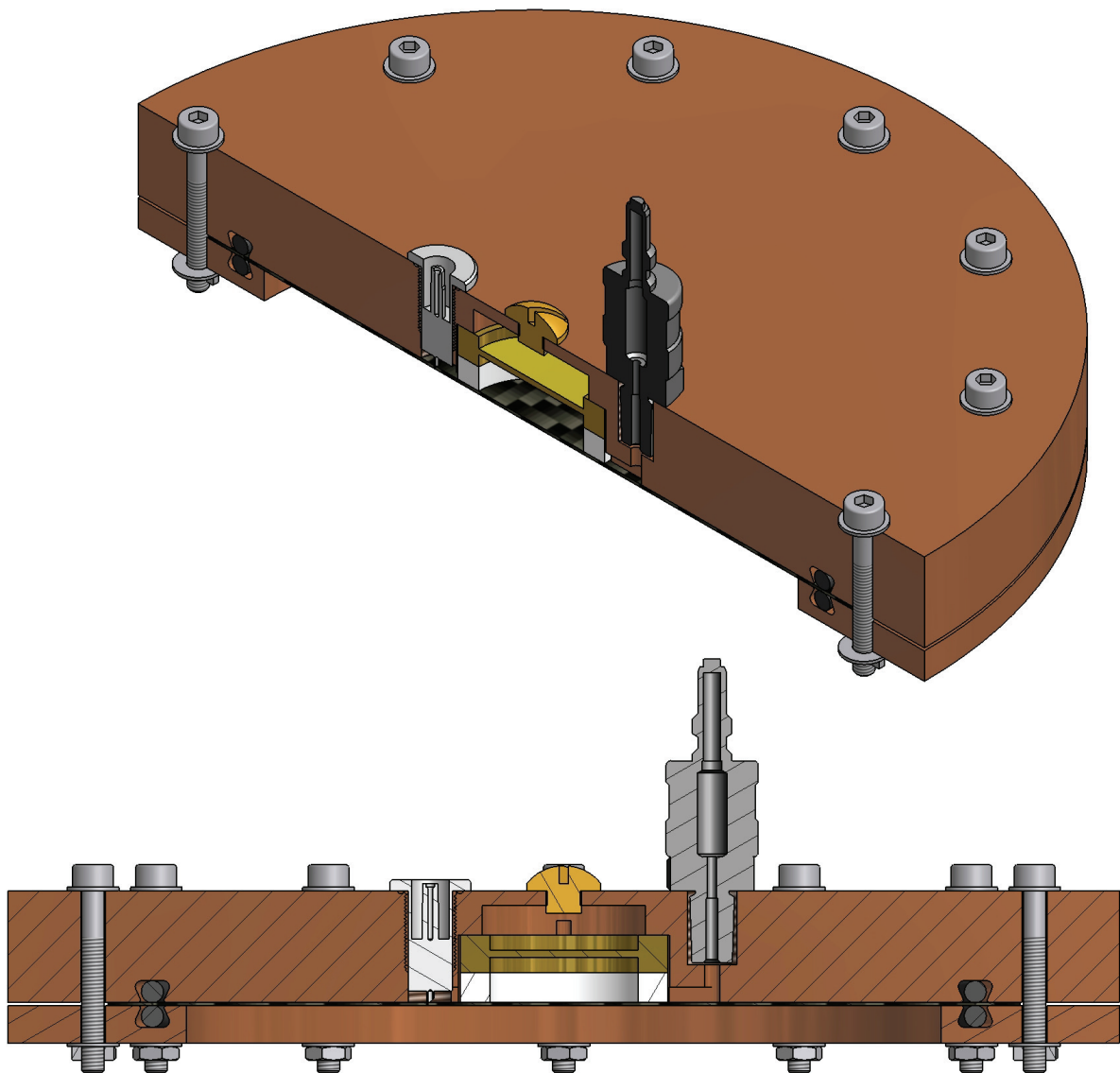


Fig. 21. Schematic drawing of the measurement cell.

(copper parts in brown, SSB detector in golden, screw for calibration source in yellow, connectors and bolting in grey and carbon epoxy window in black color)

5.2.4 Acquisition system

5.2.4.1 Analog electronics

The analog part of the acquisition system consists of a fast timing and a slow energy channel for each detector. After pre-amplification by a charge sensitive preamplifier, the signal of the SSB detector is split up into a fast and a slow signal. The fast signal is filtered by a timing filter amplifier (ORTEC 474) and digitized by a constant fraction dis-

criminator (ORTEC CF8000). The slow signal is shaped (500 ns) by a spectroscopy amplifier (Canberra 2026) and digitized by a fast (500 ns conversion time) 8k ADC (FAST ComTec 7072T). The charge sensitive preamplifier of the HPGe detector provides two identical signals. One is filtered (INT: 500 ns, DIF: 20 ns) by a timing filter amplifier (ORTEC 579) and digitized by a constant fraction discriminator (ORTEC CF8000). The other is shaped (3 μ s) by a spectroscopy amplifier (CAEN N968) and digitized by a fast (500 ns conversion time) 8k ADC (FAST ComTec 7072T). The amplified signals from the myon guard detectors are digitized and combined by OR-gating of the six independent channels of a constant fraction discriminator (ORTEC CF8000). The combined signal marks the transit of a myon through any of the guard detectors.

5.2.4.2 Digital electronics

The digital signals are matched by delays to ensure proper timing before employing them for time spectroscopy. The time difference between the fast electron and photon channel is measured by a combined Time to Amplitude and Analog to Digital Converter (TADC, FAST ComTec 7072T). The β - γ coincidence determination is carried out with software, by setting a ROI in the time spectrum, which forms the time window. The time difference between the recent myon and a photon is measured by using the real time clock (RTC) of the acquisition system. In contrast to the TADC method, this technique avoids system dead time caused by a high rate (\sim 600 cps) of start without stop signals. Every myon signal is used to reset the RTC by reload of a predefined start value. Any succeeding photon triggers the capture of the RTC time to record the time difference. The RTC-resolution of 50 ns is sufficiently small compared to the anticoincidence window of 15 μ s. The time difference between myon and photon is mapped into a time spectrum. Again the anti-coincidence determination is carried out per software. For verification of RTC method, a second TADC channel has been used for parallel measurement of the time difference.

5.2.4.3 Multi parameter data acquisition

The data from the (T)ADCs is processed by a multi-parameter data acquisition system (FAST ComTec MPA3). This system transfers the data to a PC by a high speed bus (PCI card). Data can be counted directly into spectra and/or recorded into a list-file for offline analysis. The later allows changing of the (anti-)coincidence windows during analysis. Repeated analysis of the same measurement and applying different (anti-) coincidence settings, allows to optimize the position and width of the time windows.

Figure 22 shows a schematic drawing of the electronics for data acquisition. Each of the ADCs for β/γ energy can trigger an event by opening a time window of $10\ \mu\text{s}$ for recording of data. Data from the other ADC or one of the two TADCs is recorded, when arriving within this time window. The fast conversion (500 ns) and short shaping time (β : 0.5 and γ : 3 μs) reduce system dead time. Therefore, dead time correction, which is elaborated for multi-parameter spectra (Hwang et al., 1998; Hwang et al., 2002; Smith, 1978), can be omitted for low and medium count rates (below 1000 counts).

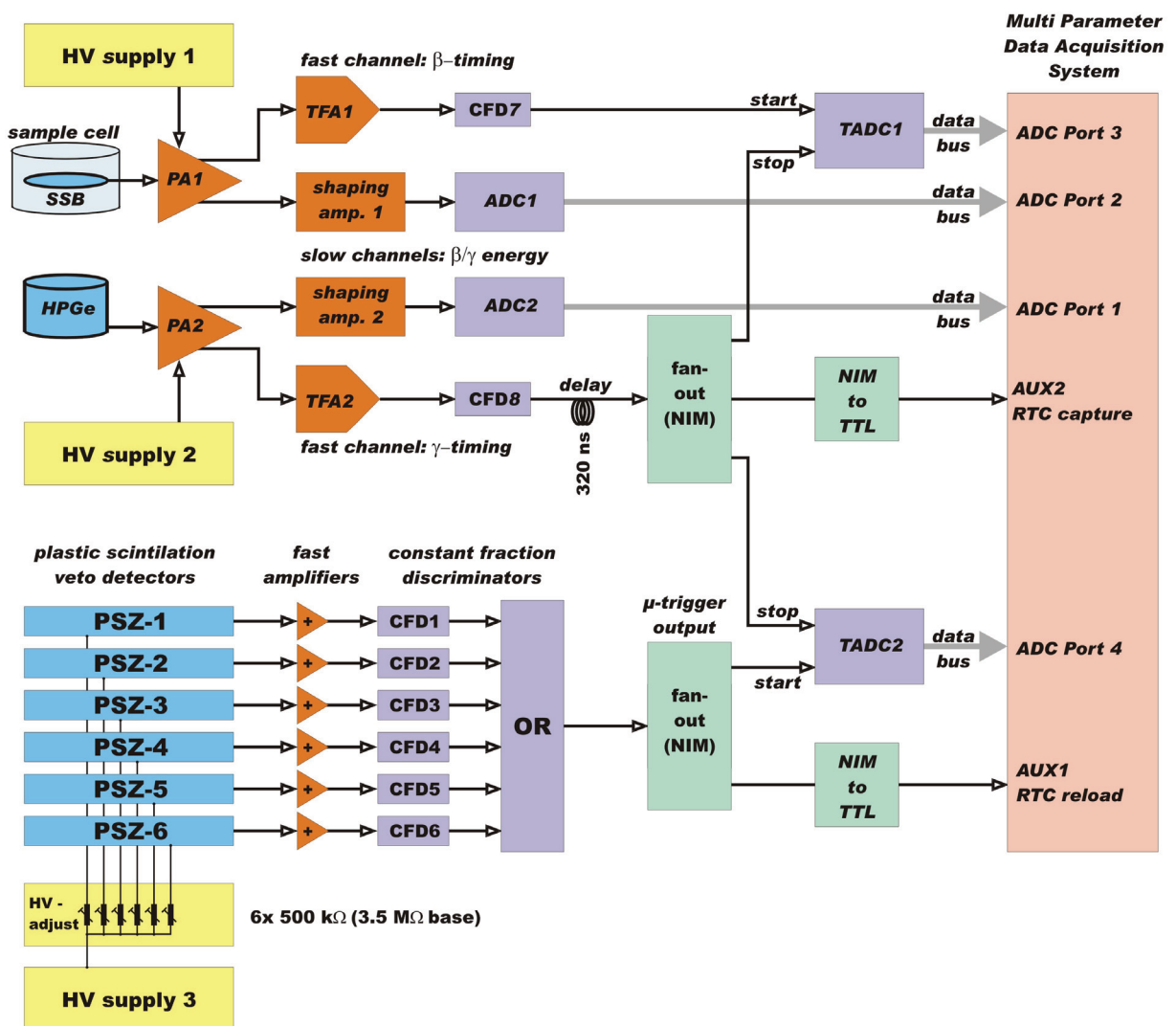


Fig. 22. Schematic drawing of the electronics for data acquisition.

5.2.5 Energy calibration and performance test

Energy calibration and performance testing is straightforward for the γ -channel. For the β -channel it is complicated by the fact, that the calibration source has to be placed inside the measurement cell and the difficulty to find a monoenergetic electron source of suitable half life. The applicability of alternative methods depends on the detector type and geometry. Implementation of a combined (phoswich) detector (Ely et al., 2005; Henning et al., 2006; Henning et al., 2007; La Fuente et al., 2008; Ward et al., 2009) for electron and photon radiation allows transfer of the energy calibration from the γ -channel to the β -channel, but its energy resolution for photons is inferior compared to a HPGe detector. Coincident measurement of Compton electrons in the β -detector and the scattered photons in the γ -detector can provide an elegant alternative (Schell et al., 1999; Reeder et al., 2004). In a 4π -measurement geometry, the whole Compton continuum can be utilized and an external gamma source creates a diagonal line in the β - γ spectrum, which can be used to transfer the energy calibration from the gamma to the β -detector. The present 2π -measurement geometry of opposite β γ detectors limits the detectable Compton scattering angle and complicates the applicability of this method for this system.

Therefore, a reference source for energy check and calibration, providing coincident monoenergetic β - and γ -radiation, has been developed. The radionuclide ^{166m}Ho has been selected because of its long half life of (1200 ± 180) years (Table de Radionucléides, Be, 2004) and the relatively low β -energy. The fact, that most of the β -energy is below 74 keV reduces the distortion of the conversion electron peaks by β -radiation. Holmium offers many gamma lines for energy calibration of the HPGe-detector (γ -channel) and coincident conversion electrons for energy calibration of the SSB-detector (β -channel) and it is also convenient for characterization of the time resolution and optimization of the coincidence time window. The reference source has been produced in house. The active area is located at the top of a brass screw in a small hollow to prevent contact. A volume of 10 μl standardized ^{166m}Ho (1M HCl) solution has been pipetted into the cavity and evaporated. The hygroscopic precipitate has been annealed at 300 °C and 500 °C for one hour to convert it into the more stable oxide (Hino et al., 2000). The active area has been covered with a thin lacquer coat for mechanical protection. The resulting retardation of the emitted conversion electrons has been measured by using un-attenuated gaseous sources of radioxenon (^{133g}Xe and ^{133m}Xe) as reference. Table 5 shows the energy shift, which is stronger at lower electron ener-

gies. Figure 23 shows a picture of the source and the storage box made of Perspex (a second source is retained in the box).



Fig. 23. Picture of the $^{166\text{m}}\text{Ho}$ β - γ energy calibration sources.

Table 5

Energy shift of the conversion electrons by the lacquer coating.

production mode	unattenuated electron energy ¹ (keV)	measured electron energy of the check-source (keV)	energy shift caused by lacquer coat (keV)
ec _{1,0} L	70.828 - 72.222	55.6 ± 0.1	15.9 ± 0.8
ec _{2,1} K	126.925 ± 0.001	117.7 ± 0.1	9.2 ± 0.1
ec _{2,1} L	174.659 - 176.053	168.3 ± 0.1	7.1 ± 0.8
ec _{3,2} K	222.978 ± 0.004	216.7 ± 0.1	6.3 ± 0.1
ec _{3,2} L	270.711 - 272.105	266.5 ± 0.1	4.9 ± 0.8

¹ from Table de Radionucléides (Be, 2004)

To insert the reference source in the measurement cell, the blind bolt in the center is unscrewed and removed. Then, the source is screwed into the cell carefully and the

active surface is positioned at the reference position close to the center of the SSB detector. Figure 24 shows the measured β - γ spectrum of the reference source. The better energy resolution of the HPGe-detector causes the narrow appearance of the conversion electron peaks as “mountain chains”, which are somewhat blurred by the weak β -radiation. The last channel of the gamma spectrum (very right side) shows a mountain chain, an interference caused by gamma energies above the upper level discriminator (ULD) of the ADC. For system check and energy calibration of the SSB detector, the ungated electron spectrum is used too, as its acquisition needs shorter measurement time.

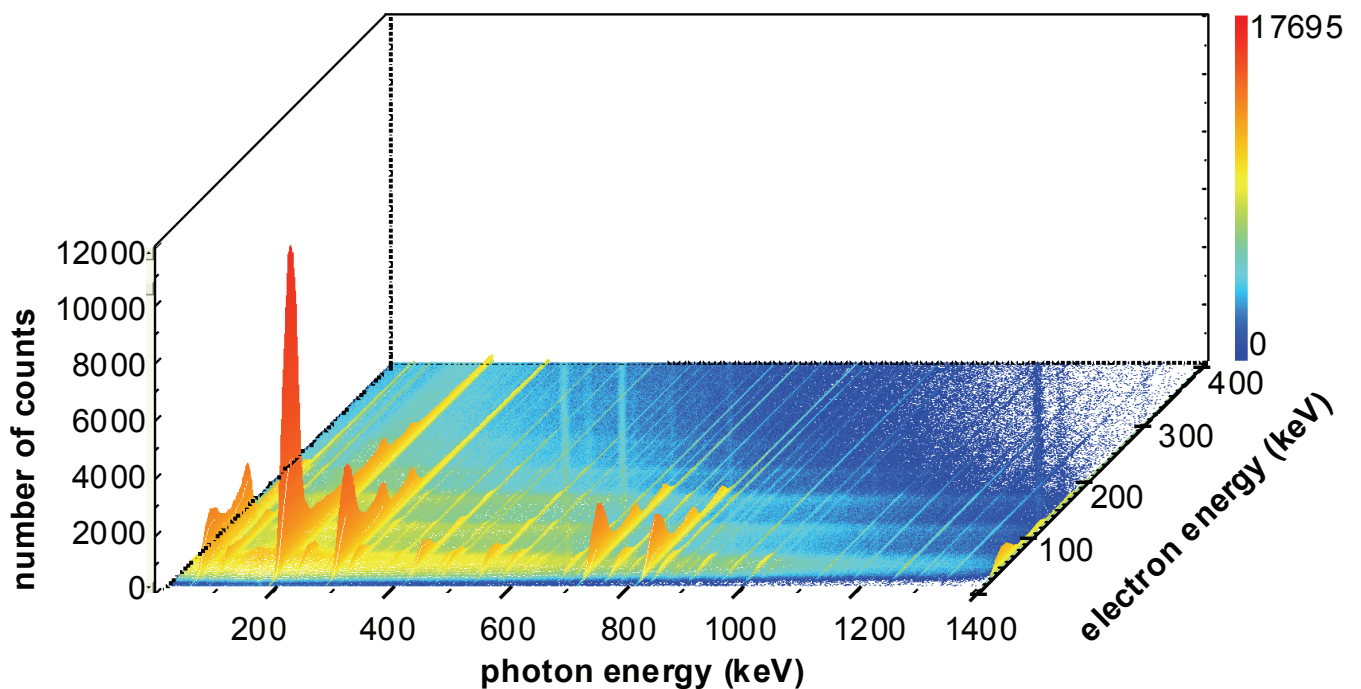


Fig. 24. β - γ spectrum of the ^{66m}Ho energy calibration source.

The x-axis relates to photon energy, y-axis to electron energy and the z-axis to the number of counts.

5.2.6 Data analysis

5.2.6.1 Dead time correction and accidental coincidences

For 2D spectra, live time is measured and dead time losses are automatically corrected in the common way (Knoll, 3rd ed). The short (3 μs) shaping time and the fast pulse processing reduce total dead time below 10 μs . For low and medium count rates (below 1000 counts), the resulting loss is below 1 % and can be neglected. For 3D spectra, dead time depends on both channels and correction is more complex. Moreover,

measured data has to be corrected for accidental chance coincidences too (Hwang et al., 1998; Hwang et al., 2002; Smith, 1978). Accidental coincidences have been estimated by shifting the coincidence window (ROI in the time spectrum) and re-analysis of the measurement. To correct for chance coincidences, the counts in the rectangular ROIs of the β - γ spectrum with shifted coincidence window are subtracted from the counts obtained before (with correctly aligned coincidence window).

5.2.6.2 Peak fit and background subtraction

In 2D spectra, the peak area is calculated by fitting a Gaussian function to account for a continuous background. Blank measurements of the empty measurement cell before sample transfer are used to subtract corresponding background peaks, induced by memory effect (radioxenon from previous measurements). In 3D spectra, the peak area has been calculated from a rectangular ROI. The continuous background is estimated and subtracted by using the mean value of a surrounding ROI. The estimation error of the multidimensional background has been identified as the major source of uncertainty for the net peak area. Even for huge peaks (negligible statistical error), it results in a typical uncertainty of 5-10 % for the peak area, which is high, compared to 2D Gaussian fit. The main reason for this difficulty is the unsteady structure of the background, typically showing mountain chains, crossing the peak and complicating a correct fit.

5.2.7 Efficiency calibration

5.2.7.1 Detection efficiency for photons

The γ -detection efficiency for gaseous samples has been determined by using a multi-nuclide area source, which has been moved through the 12 mm height of the sample cell in steps of 1 mm. The absorption of the photons by the electron detector has been simulated by placing an adequate layer of aluminum at the position of the SSB detector. The efficiency functions of each of the steps have been averaged to obtain the efficiency function of the whole sample volume. The energy range of the source has been extended down to 24.1 keV by employing the characteristic x-rays of the ^{137}Cs , ^{109}Cd and ^{113}Sn decay. X-ray emission probabilities have been taken from the Table de Radionucléides (Be, 2004). Starting with $(22.9 \pm 1.7) \%$ around 33 keV, the photon detection efficiency reaches a maximum of $(28.5 \pm 1.9) \%$ around 80 keV and drops to $(4.3 \pm 0.3) \%$ at 1 MeV.

5.2.7.2 Detection efficiency for electrons

The detection efficiency for electrons has been determined at four different electron energies (45, 129, 161 and 199 keV), by using the $^{131\text{m}}\text{Xe}$, ^{133}Xe and $^{133\text{m}}\text{Xe}$ activity determined by gamma spectroscopic measurement as a reference (parallel analysis of the ungated 2D γ -spectrum). Within an energy range from 45 keV to 199 keV, the average electron detection efficiency has been found to be $(8.5 \pm 1.1) \%$.

5.2.7.3 Peak efficiency of selected radioxenon isotopes in 3D spectra

The peak efficiency for selected peaks has been determined as basis for activity and MDA calculation. Because of the unsteady structure of the background, the uncertainty of the net areas of these 3D peaks is high, compared to 2D analysis (see previous chapter "Peak fit and background subtraction"). The peak efficiencies have been determined by using the ratio of the net-areas of the corresponding β - γ peak and a γ -reference peak to scale the peak efficiency of this γ -reference peak. The area of the γ -reference peak has been fitted by a Gaussian function and the area of the β - γ peak has been calculated by using a rectangular ROI of a width of 2.5 FWHM ($\sim 6 \sigma$). For β -radiation the length of the ROI has been extended to cover the whole continuum. Table 6 shows the peak efficiencies for selected coincident radiation pairs.

Table 6

Peak efficiency of selected 3D peaks of radioxenon isotopes

isotope	photon emission	electron emission	detection efficiency (cps/kBq)
$^{131\text{m}}\text{Xe}$	x-ray at 29.6 keV	ce at 129.4 keV	7.4 ± 0.6
$^{131\text{m}}\text{Xe}$	x-ray at 33.7 keV	ce at 129.4 keV	1.88 ± 0.16
$^{133\text{m}}\text{Xe}$	x-ray at 29.6 keV	ce at 198.6 keV	10.2 ± 1.4
$^{133\text{m}}\text{Xe}$	x-ray at 34 keV	ce at 198.6 keV	2.3 ± 0.2
^{133}Xe	x-ray at 31 keV	ce at 45 keV	5.8 ± 1.8
^{133}Xe	γ at 81 keV	β , 0-346 keV	13.4 ± 1.3
^{135}Xe	γ at 250 keV	β , 0-905 keV	23.6 ± 3.8

5.2.8 Absolute measurement of activity

Under specific conditions, coincident measurement of electron and photon radiation allows absolute (direct) measurement of activity, without reference to any supplementary data (efficiency calibration) obtained from previous experiments (Campion, 1959; Houtermans and Miguel, 1962; NCRP Rep. No. 58, 1985; ICRU Rep. 58, 1997, Park et al., 1998). Application of this method requires finding two coincident radiations, emitted at a known rate, which can be exclusively attributed to one isotope. For metrology purposes, this method is typically applied to pure isotopes, possessing 100 % probability for β - γ decay. A high resolution measurement system allows to apply this method also to isotope mixtures, provided that the corresponding peaks in all three spectra (γ , β , β - γ) can be calculated accurately (complicated by background mountain chains) and assigned to a single isotope. Application to mixed radioxenon spectra is complicated by the interference of the characteristic x-ray peaks from different isotopes which are very difficult to separate. Therefore, this method could only be used to assess the activity for a pure $^{131\text{m}}\text{Xe}$ sample. The activity has been determined by using the 129 keV and 159 keV conversion electrons in coincidence with the corresponding characteristic x-ray photons.

For the present measurement geometry both (β and γ) efficiencies are functions of the position. Therefore their local product may deviate from the product of the mean efficiency, which is averaged over the whole volume source. This deviation has been considered by introducing a correction factor K , which is the ratio of the averaged product of the efficiencies and the product of the averaged efficiencies. The common expression for direct calculation of the activity (Knoll, 3rd ed.) is given by the ratio of the product of the β and γ countrate r_β and r_γ divided by the coincident rate $r_{\beta\gamma}$. This equation has to be corrected by multiplication with the correction factor K :

$$A = \frac{r_\beta \cdot r_\gamma}{r_{\beta\gamma}} \cdot K \quad \text{in which} \quad K = \frac{\iiint_{V_{\text{source}}} \varepsilon_\beta \cdot \varepsilon_\gamma dV}{\iiint_{V_{\text{source}}} \varepsilon_\beta dV \cdot \iiint_{V_{\text{source}}} \varepsilon_\gamma dV} \quad (8)$$

For the present geometry K has been deduced from detector-source geometry by numerical integration of the solid angle functions given by Pommé et al. (2003). The resulting value of $K = (0.997 \pm 0.001)$ corresponds to only -0.3 % correction which is neglectable compared to the other sources of uncertainty. As the correction has been deduced from geometry, without using previously obtained experimental data, the measurement can still be considered as an absolute (direct) method.

To validate the results of the absolute measurement, the $^{131\text{m}}\text{Xe}$ activity has been also calculated from the ungated 2D γ -spectrum by using the x-ray at 29.6 keV or 33.7 keV and the gamma at 163.9 keV together with the appropriate detection efficiency.

5.2.9 Methods for radioxenon production

The radioxenon has been produced by using three different methods, which are complementary. The first well known method (McIntyre et al., 2003) employed neutron irradiation of small amounts of highly enriched uranium (1 μg , 90 % ^{235}U) at the TRIGA research reactor of the Atomic Institute of the Austrian Universities in Vienna. Although this method gives high flexibility in isotope ratio and activity range, preparation of the sealed fused silica ampullae and the transport of the irradiated fuel is tedious. To avoid the transport and the fabrication of the ampullae, a ^{252}Cf based generator has been used as second source for radioxenon. Similar to neutron irradiation of enriched uranium, such a generator provides radioxenon at various isotope ratios by spontaneous fission of ^{252}Cf (Dubasov et al., 2007). As third method a ^{131}I generator was used as source for pure $^{131\text{m}}\text{Xe}$. This generator allows continuous production of radioxenon for several weeks. For the two fission based production methods, the fraction of $^{131\text{m}}\text{Xe}$ is the lowest of all four isotopes and the third method could be successfully used to augment this isotope to the mixture. Therefore, these methods are used in a complementary way. Activation of stable xenon as reported by other authors (Haas et al., 2009) has not been implemented within this study. A detailed description of the production methods and purification process will be subject of another publication.

5.2.10 Monitoring of system performance and data quality

A series of eight 2D spectra and one 3D spectrum has been configured to monitor system performance during data acquisition. Figure 25 shows the combined view of these spectra. The first two energy spectra show the ungated photon (GAMMA) and electron (BETA) events (see Fig. 25 a, b). The low level threshold (LLD) of the β -energy channel (ADC) is set very low (around 15 keV) and extends into the noise, which causes the pronounced rise of counts at the low energy end. This is also the reason, why the ungated beta spectrum has much more counts than the gamma spectrum. Increasing the cut off energy for the beta channel to 35 keV, which is slightly above the noise level at about 3 times the FWHM of 9 keV, would make the count rate in the beta channel even smaller than in the gamma channel. The coincidence time spectrum (Fig. 25c) shows the time distribution between beta (start) and gamma (stop) radiation. The gamma channel is delayed by about 1 μs compared to the beta channel. The combined time

resolution (FWHM) of the β - γ detectors is 0.6 μ s. The total number of counts in the spectrum corresponds to all events within the priming coincidence time of 10 μ s. The main coincidence window (1.4 μ s width) is tuned by adjusting the ROI (marked red) in this spectrum. For this coincident calibration source spectrum, only 6 % of the events are outside the ROI and have to be rejected. For uncorrelated background radiation the number of events, rejected by this main coincidence is considerably higher (around 86 %) as their number is proportional to the width of the coincidence window (1.4 μ s vs. 10 μ s). The gated beta and gamma energy spectra (Fig. 25 d, e) show a slightly smaller and a little different number of counts. The reason is that the coincidence time spectrum is triggered by the fast beta and the fast gamma channel, having a slightly different energy threshold compared to the energy channels. Therefore, some coincident events from the coincidence time spectrum have invalid beta or gamma energy and do not appear in the associated gated spectrum. The slightly lower number of counts in the gated beta and gamma spectra compared to the coincidence time spectrum results from conversions which have been below the low level threshold (LLD) or above the high level threshold (ULD) of the ADC. These pulses triggered both fast channels but no energy information has been recorded. The thresholds of the fast timing channels are set somewhat below the thresholds of the corresponding energy channels to avoid that valid conversions from an energy channel are rejected, just because they have been missed, by the corresponding fast timing channel. By applying the coincidence, the noise in the beta gated spectrum is shifted down to approximately 20 keV compared to about 35 keV in the ungated spectrum. The application of the coincidence extends the available energy range of the detector towards lower energies into the noise. The gamma vetoed spectrum (Fig. 25 g) monitors the operation/rejection of the anti-cosmic veto. It shows the photons, arriving within the anti-coincidence time after detection of a muon in one of the guard detectors. These photons are suppressed in the main spectra. The two spectra MYON-RTC and MYON-TADC (Fig. 25 h, i) show the time distribution between muons and photons measured with RTC or TADC to monitor and optimize the anti cosmic veto. The time range of the TADC is limited by the resulting dead time and has been set to 5 μ s, whereas the time range of the RTC is open and only the displayed range has been limited to 400 μ s. The RTC time spectrum is used to perform the anticoincidence by setting the ROI (time window) there. The TADC spectrum has been used to validate the RTC-based time spectroscopy and will be removed for routine operation. The 3D spectrum BETA x GAMMA (see Fig. 25 f) shows the coincidence events selected by the time window (ROI) in the time spectrum COINCIDENCE TIME (Fig. 25 c).

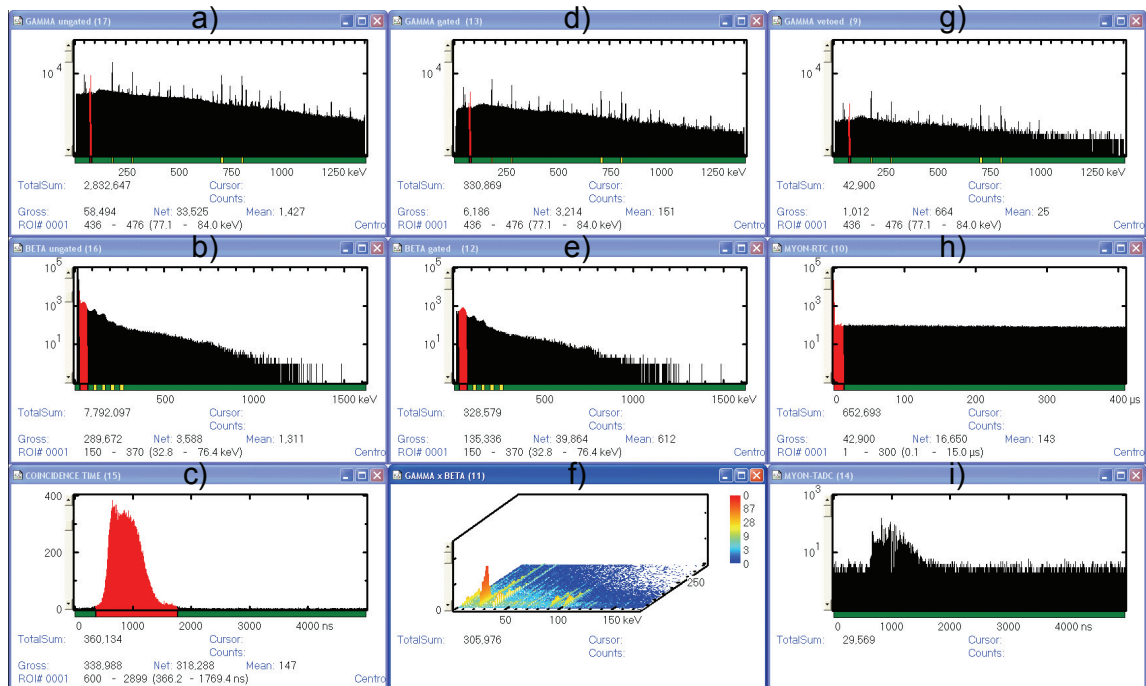


Fig. 25. Spectra for monitoring of system performance. **a)** ungated gamma energy spectrum; **b)** ungated beta energy spectrum; **c)** coincidence time spectrum; **d)** gated gamma energy spectrum ; **e)** gated beta energy spectrum; **f)** 3D spectrum beta x gamma; **g)** vetoed gamma energy spectrum; **h)** myon time distribution RTC; **i)** myon time distribution TADC

5.3 Results and Discussion

5.3.1 Spectra of different radioxenon isotope mixtures

Spikes of different isotope mixtures have been measured to demonstrate the system performance. Figure 26 shows the β - γ spectrum of a pure ^{131m}Xe spike, which allowed absolute measurement of activity. The x-axis relates to photon energy, y-axis to electron energy and the z-axis to the number of counts. The activity of (16.3 ± 1.1) kBq generated more than 3 million coincident counts, during an acquisition time of about 2.4 hours. The good statistics leads to a precise view in the 3D spectrum and allows observation of small details. The two main peaks result from joint detection of the 129.4 keV K-conversion electrons and the succeeding 30.6 keV (K_{α}) or 33.7 keV (K_{β}) xenon x-ray. Behind these peaks, chance coincidence with 160 keV conversion electrons and continuous electron background causes two tiny peaks and lines. On the left side of the two main peaks, they are accompanied by their germanium x-ray escape peaks at a photon energy of 9.9 keV (K_{α}) and 11 keV (K_{β}) below the characteristic xenon x-rays. The electron continua (mountain chains) prolonging the main peaks from

129 keV towards lower energies, are caused by variable energy losses due to detector surface and backscatter effects.

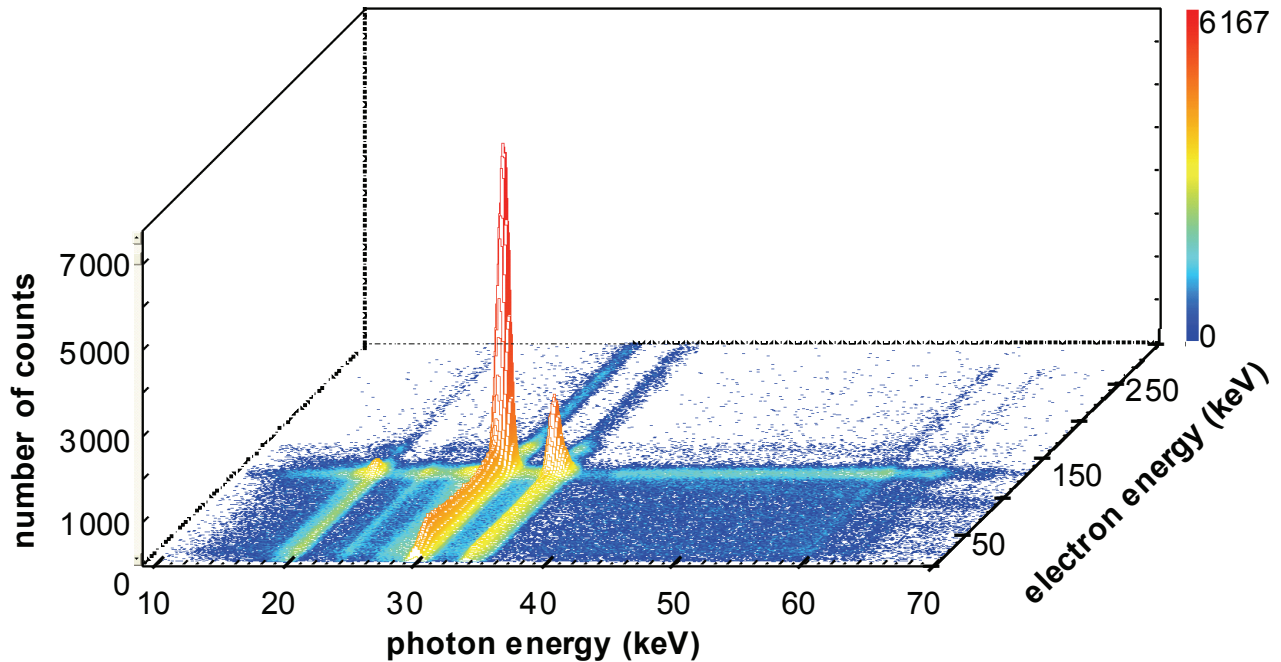


Fig. 26. β - γ spectrum of pure ^{131m}Xe .

Figure 27 shows a radioxenon spike consisting of (600 ± 40) Bq ^{133}Xe and (17 ± 1) Bq ^{133m}Xe . The measurement time of about 10.1 days led to a total of more than 13 million coincident counts. Coincident detection of the ^{133}Xe , 81 keV γ -radiation and 0-346 keV β -continuum creates the mountain chain on the left side in figure 27. The converted 81 keV γ -transition leads to 32 or 45 keV conversion electrons in coincidence with the β -continuum and the 30.8 keV (K_α) or 35 keV (K_β) Cs x-rays. These two mountain chains at 31 and 35 keV are accompanied by their Ge x-ray escape chains at 9.9 keV (Ge- K_α) and 11 keV (Ge- K_β) lower photon energy. The main peaks of ^{133m}Xe appear closely but well separated to the β -continuum of ^{133}Xe . The 29.7 keV (K_α) and 33.6 keV (K_β) Xe x-ray in coincidence with 198.6 keV conversion electrons create only two small spots, as the ^{133m}Xe activity is more than 30 fold lower than ^{133}Xe .

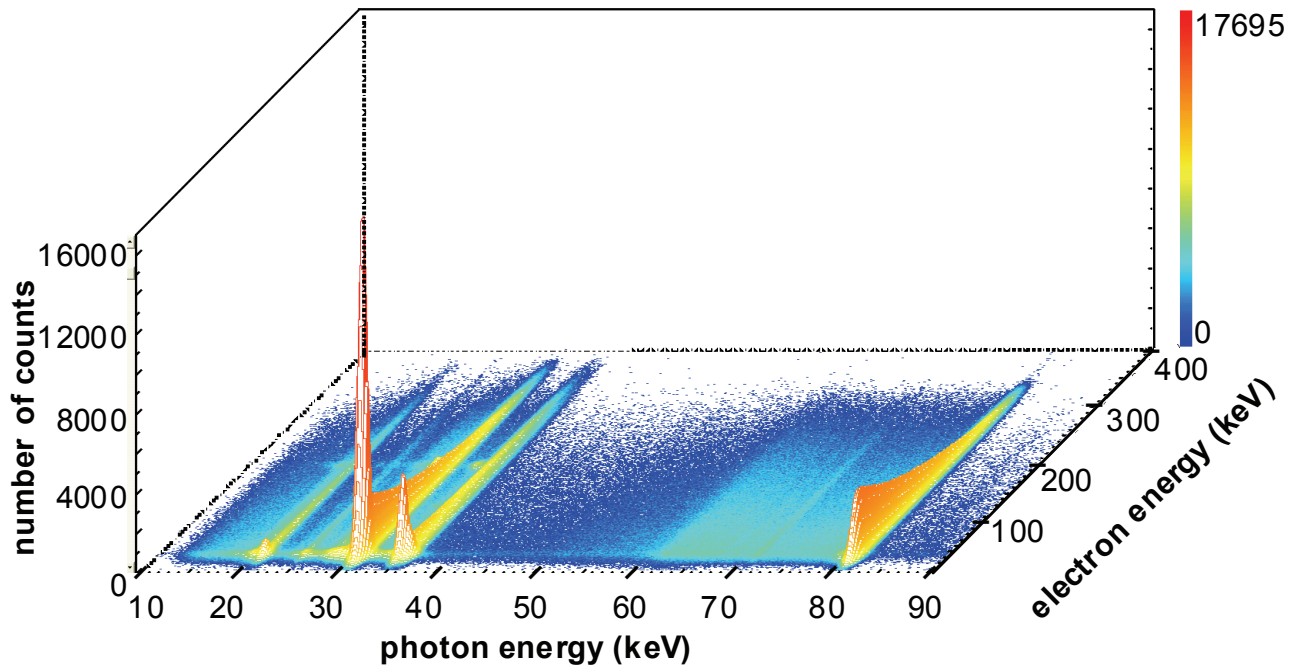


Fig. 27. β - γ spectrum of ^{133}Xe and $^{133\text{m}}\text{Xe}$.

5.3.2 Absolute measurement of activity

The absolute measurement method has been successfully used to assess the activity for a pure $^{131\text{m}}\text{Xe}$ sample (Campion, 1959; Houtermans and Miguel, 1962; NCRP Rep. No. 58, 1985; ICRU Rep. 58, 1997, Park et al., 1998). Although no detection efficiency is needed, the emission probability of $(61.0 \pm 2.6) \%$ (Table of Radionuclides, Be, 2004) for the conversion electron has to be considered for activity calculation. By using the 129 and 159 keV conversion electrons in coincidence with the corresponding characteristic x-ray photons an activity of (15.9 ± 0.7) kBq has been determined. Alternative calculation from the ungated 2D γ and β spectrum by using the x-ray at 29.6 or 33.7 keV and the gamma at 163.9 keV together with the appropriate detection efficiency leads to an activity of (16.3 ± 1.1) kBq which is in good agreement with the value obtained by absolute measurement.

5.3.3 Background reduction by μ - γ anticoincidence

The possible reduction of the background by applying an anticoincidence between cosmic muons and photons (anti cosmic veto) has been investigated. By reducing the photon background, the anticoincidence affects also the coincident β - γ background. The aim was to investigate, how much the already very low count rate of the β - γ coincidence system could be further reduced by μ - γ anticoincidence. Muons and their sec-

ondary particles can coincidentally trigger β and γ detector counts and annul the coincidence. Myon anticoincidence should reduce this effect.

5.3.3.1 Validation and comparison of veto implementation

An alternative method for implementation of the anti cosmic veto by using a 100 MHz real time clock (RTC) has been implemented, validated and compared with the well known TAC-ADC method (Poinurier et al., 1996; Laurec et al., 1996). Figure 22 shows the parallel implementation of both methods. The main advantage of the RTC method is that the start time for the measurement it is retriggerable. Therefore, only the (shortest) time difference between the most recent μ and a following γ is recorded. In conventional TAC-ADC based time spectroscopy, after triggering of the TAC, other arriving muons are missed, as they cannot restart the time measurement. To reduce the number of missed muons, the time range of the TAC has to be set considerably smaller than the average time difference between succeeding muons. Table 7 presents a comparison of the two methods and shows their advantages and limitations. On one hand, the RTC method provides a better background suppression factor of 4.8 compared to only 4.0 for the TAC-ADC method. On the other hand, the measurement efficiency drops by 2.2 % compared to only 0.8 % for the TAC-ADC method. In practical use the 1.4 % higher loss of efficiency, is compensated by the 20 % lower background and the better usability of the RTC method. Therefore, it will be retained in routine operation.

Table 7

Comparison of veto implementation by TAC-ADC and RTC method

	fraction of valid γ -counts (15 – 1380 keV)					
veto implementation	TAC-ADC			RTC		
veto ROI	2 μ s width; centered on cosmic μ -signal			10 μ s – 26.2 ms after recent μ		
	clean signal	cosmic back-ground	untagged	clean signal	cosmic background	untagged
localization in μ - γ time spectrum	outside veto ROI or not time-tagged	inside veto ROI	not included	within veto ROI	outside veto ROI	not included
limitation / advantage	- TAC time range limited by lack of ability to retrigger and by dead time	+ good time resolution results in a sharp peak	- untagged noise is treated as signal and increases the background	+ more cosmic removed	- higher efficiency drop	+ almost all events tagged
background (one week)	(25.0 \pm 0.1) %	(75.0 \pm 0.1) %	(21.7 \pm 0.1) %	(21.0 \pm 0.1) %	(79.0 \pm 0.1) %	< 1E-3 %
sample (^{166m}Ho)	(99.2 \pm 0.1) %	(0.8 \pm 0.1) %	(98.2 \pm 0.1) %	(97.8 \pm 0.1) %	(2.2 \pm 0.1) %	< 1E-5 %
cosmic suppression	1 : 4.0 \pm 0.02			1 : 4.8 \pm 0.02		
efficiency drop	0.8 %			2.2 %		

The TAC-ADC method has been used to validate and benchmark the RTC method. Table 8 shows the processing summary of the TAC-ADC method. Only γ -counts within the energy range of 15 to 1380 keV are considered of being “valid”. The processing summary has been calculated for two types of spectra, sample (^{166m}Ho reference source) and background, each listed in a separate column. Emphasis is put on the effect of the not tagged γ -counts. In the background, 78.3 % of the γ -counts are tagged and almost all of them (95.8 %) are cosmic induced and removed. Most of the γ -counts of the sample had no succeeding muon within the 5 μ s time range of the TAC and are not tagged. Therefore only 1.8 % γ -counts of the sample are tagged and 44.4 % of these are removed as being in the cosmic-ROI. The tagging probability of not muon correlated γ -counts (chance coincidences) is set by the ratio of the time window width (2 μ s) and the total TADC range (5 μ s) to 40 %. In the mixture of sample and cosmic

signal, this value is averaged up to 44 % by the 96 % tagging probability for the cosmic counts (real coincidences).

Table 8

TAC-ADC processing summary.

TAC-ADC processing summary for valid γ -counts (15 – 1380 keV)		
background	sample	result
78.3 %	1.8 %	total γ tagged by TAC-ADC
95.8 %	44.4 %	of these tagged within ROI and removed;
75.0 %	0.8 %	totally removed
25.0 %	99.2 %	remaining rest

background: 0.80 cps; sample: 1010 cps (^{166m}Ho reference source)

5.3.3.2 Background reduction for the β - γ coincidence by μ - γ anticoincidence

The validated RTC based μ - γ anticoincidence has been applied to the β - γ coincidence system. The high background reduction of the β - γ coincidence results in an ultra low background of around 0-1 count per week in the ROIs of the main radioxenon isotopes. For statistical reasons, the small number of counts within a ROI couldn't be used as a measure for background reduction. Therefore, the effect of the μ - γ anticoincidence on the total counts in the 3D β - γ spectrum has been measured. Since the distribution of these counts within the 2D energy plane showed no regions of cumulation, the reduction in the total number of background counts is representative also for comprised ROIs. The background in the 2D plane of γ -energy from 15 to 350 keV and β -energy from 20 to 1500 keV shows a total count rate of 635 counts per week. This could be further reduced down to 320 counts per week by application of the μ - γ anticoincidence. The background reduction factor of 1.98 ± 0.14 is lower than for pure gamma spectroscopy background (4.8 for γ -energies 15-1380 keV), but demonstrates very clearly, that one half of the remaining background of the β - γ coincidence is of cosmic origin and could be suppressed. Measurement of the ^{166m}Ho reference showed the same efficiency drop of $(2.3 \pm 0.6) \%$ as in the application on the sole gamma spectrum $(2.2 \pm 0.1) \%$ and confirmed valid operation of the measurement system.

5.3.4 Calculation of the minimum detectable activity

The minimum detectable activity (MDA) has been calculated as a function of measurement time for the relevant radioxenon isotopes. The common Currie (Currie, 1968, 1999, 2004) equations could not be applied, due to the very low background of only 0-3 counts per ROI during a two week background measurement. The approximation of Poisson by Gauss distribution would not be correct for such small numbers (De Geer, 2004; Knoll, 3rd ed.). Therefore, the MDA has been calculated by strictly using Poisson distribution. A set of subroutines has been implemented in Origin script (OriginLab, Northampton, MA) to calculate the mean value μ as function of the abscissa k and the confidence level and vice versa. Implementation is facilitated by the fact, that Origin provides a function `poisscdf(k, μ)` to compute the lower tail probability up to a position k , associated with a Poisson distribution using the corresponding mean value μ . A confidence level (CL) of 95 % has been assigned for both kinds of errors (false negative and false positive). For false positive detection, this 95 % CL has been divided into two equal parts of 97.5 % CL ($0.975^2 \sim 0.95$); one for the estimate of the background and the other for the assumption, that background fluctuations do not extent the critical level (LC).

5.3.4.1 Estimate of background

Two dimensional, rectangular ROIs of a width of 2x2 times the corresponding energy resolution (FWHM) in both dimensions have been defined, to calculate the MDA and to make the decision about detection. To reduce the uncertainty for the background estimate, an 8-fold of this area has been used to calculate its average counts. The increasing density for lower β -energies and the proximity of some ROIs to the β -energy cutoff have been considered by preferably expanding the ROI in the γ -energy axis. Practically, the number of channels for the ROI used to come to a detection decision (2x2 FWHM) has been calculated and multiplied by the mean number of counts per channel, averaged from the extended ROI for background estimation (3 β -FWHM x 10 γ -FWHM).

5.3.4.2 Calculation of critical level, detection limit and MDA

The calculation of the MDA in principle follows the Curie (Currie 1968, 1999, 2004) approach, but uses discrete Poisson instead of Gaussian distribution. First step is the calculation of an estimate for the background mean value μ_B . It is calculated iteratively, by increasing μ , until the lower tail probability up to a position k is above the accepted risk level of 2.5 % (97.5 % CL). The number of measured background counts is used

as the value for k . The estimated mean μ_B of the background measurement is then scaled by the ratio of (measured/simulated) live time and channels (expanded/real ROI) to derive the mean value μ_B of the simulated measurement time. The critical level (LC) is calculated from this μ_B by iteratively increasing the value of k until the lower tail probability exceeds the confidence level of 97.5 % (2.5 % risk). This ensures that the combined risk for false positive is 5 % (95 % CL). The discrete nature of Poisson distribution causes steps of LC, which result in steps in the MDA too (see figure 28). The detection limit is obtained analog to the first step. At first, the mean of combined signal and background μ_{SB} is calculated by iteratively increasing μ , until the lower tail probability up to a position k ($k=LC$) is above the accepted risk level of 5 % (95 % CL). Subtraction of the background mean μ_B from the combined mean μ_{SB} gives the signal mean μ_S , which corresponds to the detection limit LD. To calculate the MDA from LD, the same approach as for the Gaussian model can be applied; see (Currie, 1968 or DeGeer, 2004). Figure 28 shows the MDA for the four radioxenon isotopes as a function of measurement time in the range from 0.1 to 100 days.

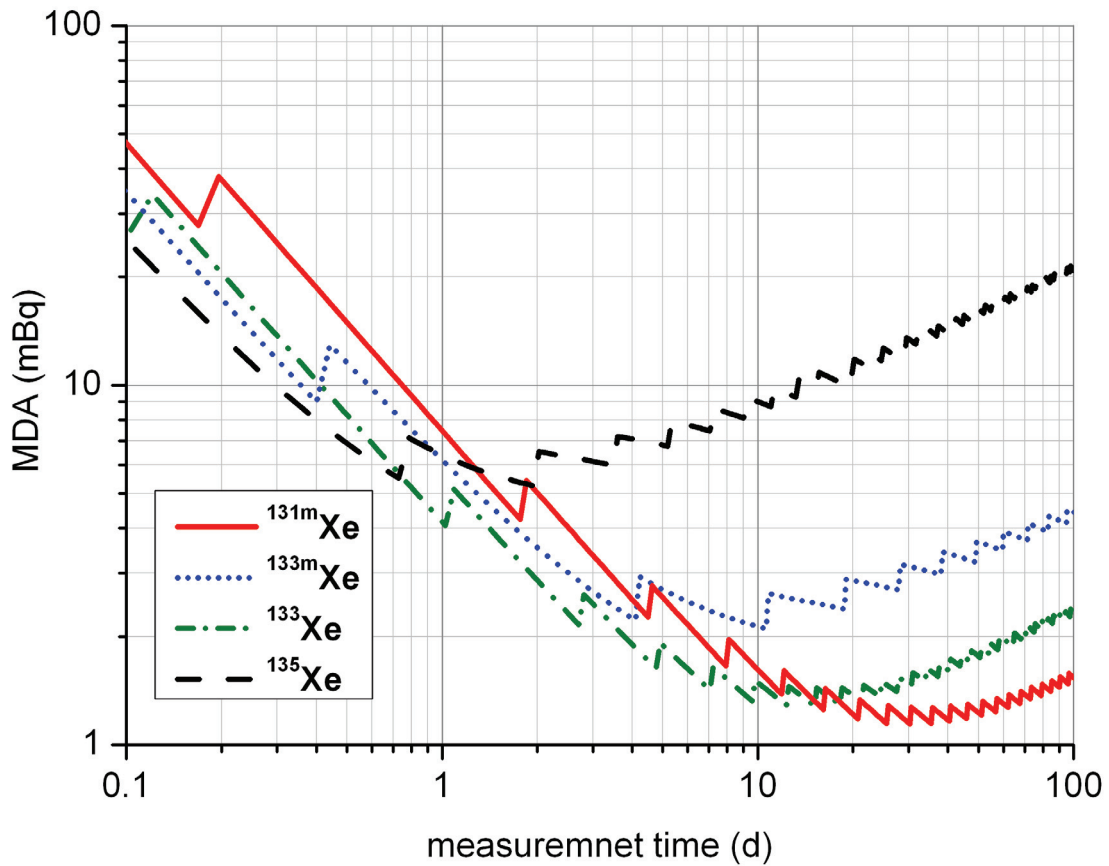


Fig. 28. MDA for ^{133}Xe , $^{133\text{m}}\text{Xe}$, $^{131\text{m}}\text{Xe}$, ^{135}Xe as function of measurement time.

5.3.4.3 Improvement of the MDA by μ - γ anticoincidence and β - γ coincidence

The reduction of the MDA of the four major radioxenon isotopes by application of (anti-) coincidence methods has been investigated. Table 9 presents the MDA obtained by the β - γ coincidence and μ - γ anticoincidence compared to ungated gamma spectroscopy. The MDA for the ungated system and the μ - γ anticoincidence could be calculated according to Curie (Curie, 1968) by using a 95 % confidence level, as their higher background rates justify the approximation of Poisson by Gauss distribution.

Table 9

Improvement of the MDA by application of (anti-) coincidence.

Isotope	Measurement time	MDA ¹ (mBq)		
		β - γ coincidence & μ - γ anticoincidence	μ - γ anticoincidence	ungated
^{131m} Xe	7 days	1.8	61	163
¹³³ Xe		1.4	2.8	7.0
^{133m} Xe		2.4	30	78
¹³⁵ Xe	1 day	6.4	9	23

¹At equal 95 % confidence level (5 % probability for both kinds of risk respectively)

5.4 Conclusions

5.4.1 Operation of the β - γ coincidence measurement system

Routine use of the new ^{166m}Ho energy calibration and check source has improved the reliability and stability of the measurement system. The high energy resolution of the detectors could be verified by demonstrating the peak discrimination in spectra containing ¹³³Xe, ^{133m}Xe and ^{131m}Xe. The peak efficiency for selected 3D peaks has been determined as a basis for activity determination and MDA calculation. Absolute measurement has been successfully applied to a pure ^{131m}Xe source and showed good agreement with conventional 2D gamma spectroscopy.

5.4.2 Background reduction and MDA

It could be demonstrated, that complementary application of an μ - γ anticoincidence further reduces the already low background of a β - γ coincidence system by a factor of about two. The RTC based μ - γ anticoincidence has been verified and showed better performance compared to the TAC based method. Due to the 2π -measurement geometry, the detection efficiency for each channel is around 10-20 % and the resulting product is below 3 %. Consideration of the emission probabilities leads to peak efficiencies in the range of only 0.01 cps/Bq. Nevertheless, the low detection probability is

compensated by the dramatic background reduction (0-1 counts per week within ROI), which leads to an increased overall sensitivity of the measurement system.

The application of μ - γ anticoincidence reduced the MDA by about a factor of two for all four radioxenon isotopes, compared to conventional ungated gamma spectroscopy. Complementary adoption of β - γ coincidence further reduced the MDA for the metastable isotopes by more than an order of magnitude. The MDA for ^{135}Xe reaches about 6 mBq after one day of measurement. For $^{131\text{m}}\text{Xe}$, ^{133}Xe and $^{133\text{m}}\text{Xe}$ a MDA of about 2 mBq is obtained after one week measurement.

References

(in order of appearance)

Chapter 1

Schroettner, T., Schwaiger, M., Kindl, P., 2004. Optimization of an Active Anti Cosmic Veto Shielding. *Applied Radiation and Isotopes*, Vol. 61, pp 133-138 (2004).

Schroettner, T., Kindl, P., Presle, G., 2009. Enhancing sensitivity of portal monitoring at varying transit speed. *Applied Radiation and Isotopes*, Vol. 67, pp 1878-1886.

Schroettner, T., Kindl, P., 2010. Long term comparison of methods to sustain energy calibration in low level gamma-ray spectroscopy and investigation of possible sources for drift. *Applied Radiation and Isotopes*, Vol. 68, pp 164–168.

Schroettner T., Schraick I., Furch T., Kindl P., A high resolution, multi parameter, β - γ coincidence, μ - γ anticoincidence system for radioxenon measurement. *Nuclear Instruments and Methods in Physics Research, Section A: Accelerators, Spectrometers, Detectors and Associated Equipment*, submitted to NIM A on 30.1.2010.

W. R. Leo. *Techniques for Nuclear and Particle Physics Experiments*. 2nd ed. Springer-Verlag, ISBN 0-387-57280-5.

G. F. Knoll. *Radiation detection and measurement*. 3rd ed. J. Wiley & Sons, ISBN 0-471-07338-5.

Michael F. L'Annunziata. *Handbook of Radioactivity Analysis*. Academic Press, ISBN 0-12-436255-9.

K. Debertin and R. G. Helmer. *Gamma and x-ray Spectroscopy with Semiconductor Detectors*. North-Holland/Elsevier Science Publishing Company Inc., ISBN 0-444-871071.

M.-M. Bé, V. Chisté, C. Dulieu, E. Browne, et al. *Table de Radionucléides*. LNE-LNHB/CEA, monographie BIPM-5 (2004).

Chapter 2

Currie L. A., 1968, Limits for Qualitative Detection and Quantitative Determination. Analytical Chemistry, Vol. 40, No.3, 586–593.

Pointurier F., Laurec, Blanchard X, 1996. Cosmic-ray Induced Background reduction by Means of an Antic cosmic Shield. Appl Radiat. Isot., 47 (9/10), 1043-1048.

Laurec J., Blanchard X., Pointurier F., 1996. A new low background gamma spectrometer equipped with an anti-cosmic device. Nuclear Instruments and Methods in Physics Research A, 369, 566-571.

Reeves J. H., Arthur R. J., 1988, Antic cosmic-shielded ultralow-background germanium detector systems for analysis of bulk environmental samples. Journal of Radioanalytical and Nuclear Chemistry, Articles, 124 (2), 435-447.

Vojtyla P., Beer J., Stavina. P., 1994, Experimental and simulated cosmic muon induced background of a Ge spectrometer equipped with a top side anticoincidence proportional chamber. Nuclear Instruments and Methods in Physics Research B 86, 380-386.

Heusser G., 1991, Studies of γ -ray background with a low level germanium spectrometer. Nuclear Instruments and Methods in Physics Research B 58, 79-84.

Westphal G. P., 1982. Real time correction of counting losses in nuclear pulse spectroscopy. Journal of Radioanalytical and Nuclear Chemistry, Articles, 70 (1-2), 387-410.

Westphal G. P., 1985. Instrumental correction of counting losses in nuclear pulse spectroscopy. Nuclear Instruments and Methods in Physics Research B, 10/11, 1047-1050.

Heusser G., 1993, Background in ionizing radiation detection - Illustrated by Ge-spectroscopy. Proceedings of the 3rd International Summer School on Low-Level Measurement of Radioactivity in Environment: Techniques and Applications. Huelva, Spain 1993, pp. 69-112.

Chapter 3

- Presti**, C.A., Weier, D.R., Kouzes, R.T., Schweppe, J.E., 2006, Baseline suppression of vehicle portal monitor gamma count profiles - a characterization study, *Nucl. Instrum. Methods A*, 562, 281-297.
- Ely**, J.E., Kouzes, R., Schweppe, J., Siciliano, E., Strachan, D., Weier, D., 2006, The use of energy windowing to discriminate SNM from NORM in radiation portal monitors, *Nucl. Instrum. Methods A*, 560, 373-387.
- Schrenk**, M., Arlt, R., Beck, P., Boeck, H., Koenig, F., Leitha, T., 2004, A Real Time Isotope Identifying Gamma Spectrometer for Monitoring Pedestrians, *Nuclear Science Symposium Conference Record*, Vol. 1, 190-195.
- Runkle**, R.C., Mercier, T.M., Anderson, K.K., Carlson, D.K., 2005, Point Source Detection and Characterization for Vehicle Radiation Portal Monitors, *IEEE Trans. Nuc. Sci. NS-52* (6), 3020-3025.
- Wahl**, C.G., Alderson, D., Pibida, L., 2007, Studies for software optimization for gross counting portal monitors, *Nucl. Instrum. Methods A*, 574, 185-191.
- Ely**, J.H., Siciliano, E.R., Kouzes, R.T., 2004, Comparison of NaI(Tl) Scintillators and High Purity Germanium for Vehicle Portal Monitoring Applications, *IEEE Nuclear Science Symposium Conference Record*, Vol. 3, 1584-1587.
- Presti** L.P., Milbrath B., Tardiff M., McBride S.H., 2007, Results From Application of Time Series Concept to Vehicle Gamma Count Profiles, In: *Proceedings of the IEEE Conference on Technologies for Homeland Security*, 133-138.
- Fehlau**, P.E., 1993, Comparing a Recursive Digital Filter with the Moving-Average and Sequential Probability Detection Methodes, for SNM Portal Monitors, *IEEE Trans. Sci.*, Vol. 40 (2), 143-146.
- Kangas**, L.J., Keller, P.E., Siciliano, E.R., Kouzes, R.T., Ely, J.H., 2008, The use of artificial neural networks in PVT-based radiation portal monitors, *Nucl. Instrum. Methods A*, 587, 398-412.
- Ayaz-Maierhafer**, B., DeVol, T.A., 2007, Determination of absolute detection efficiencies for detectors of interest in homeland security, *Nucl. Instrum. Methods A*, 579, 410-413.

- Nafee**, S.S., Abbas, M.I., 2008,
A theoretical approach to calibrate radiation portal monitor (RPM) systems,
Appl. Radiat. Isot. 66, 1474-1477.
- Siciliano**, E.R., Ely, J.H., Kouzes, R.T., Milbrath, B.D., Schweppe, J.E., Stromswold, D.C., 2005, Comparison of PVT and NaI(Tl) scintillators for vehicle portal monitor applications, *Nucl. Instrum. Methods A*, 550, 647-674.
- Stromswold**, D.C., Darkoch, J.W., Ely, J.H., Hansen, R.R., Kouzes, R.T., Milbrath, B.D., Runkle, R.C., Sliger, W.A., Smart, J.E., Stephens, D.L., Todd, L.C., Woodring, M.L., 2004, Field tests of a NaI(Tl)-Based Vehicle Portal Monitor at Border Crossing, *IEEE Nuclear Science Symposium Conference Record*, Vol. 1, 196-200.
- Schweppe**, J.E., Ely, J.H., McConn, R.J., Pagh, R.T., Robinson, S.M., Siciliano, E.R., 2006, The Effect of the Three-Dimensional Geometry of Cargo on the Detection of Radioactive Sources in Cargo, Containers, *IEEE Nuclear Science Symposium Conference Record*, Vol. 1, 295-299.
- Currie**, L.A., 1968,
Limits for qualitative detection and quantitative determination – application to radiochemistry, *Anal. Chem.* 40, 586-593.
- Currie**, L.A., 1984,
Lower limit of detection: Definition and Elaboration of a Proposed Position for Radiological Effluent and Environmental Measurements,
Report issued by the US Nuclear Regulatory Commission. NUREG/CR-4007, 1-139.
- De Geer**, L.E., 2004,
Currie detection limits in gamma-ray spectroscopy,
Appl. Radiat. Isot. 61, 151–160.
- Burr**, T., Gattiker, J.R., Myers, K., Tompkins, G., 2007,
Alarm criteria in radiation portal monitoring,
Appl. Radiat. Isot. 65, 569-580.

Chapter 4

Debertin K., Helmer R. G. 1989.

Gamma-ray-And X-Ray Spectrometry With Semiconductor Detectors.

published by Elsevier Science Ltd., ISBN 0444871071 and 9780444871077.

Attrep M., Kahn B. 2007.

Gamma-ray Spectral Analysis of a Solution of Mixed Fission Products.

Springer New York, 978-0-387-46914-0 (Print) 978-0-387-46925-6.

Hu, Z., Glasmacher, T., Mueller, W. F., Wiedenhöver, I. (2002).

An automatic energy-calibration method for segmented germanium detectors.

Nuclear Instruments and Methods, 482(3), 715-719.

Stézowski, O., Astier, A., Prévost, A., Smith, A. G., Wall, R. (2002).

Automatic energy calibration of germanium detectors using fuzzy set theory.

Nuclear Instruments and Methods, 488(1-2), 314-322.

Pattabiraman, N. S., Chintalapudi, S. N., Ghugre, S. S. (2004).

A novel iterative energy calibration method for composite germanium detectors.

Nuclear Instruments and Methods, 526(3), 439-446.

Hurtado, S., García-León, M., García-Tenorio, R. (2006).

A revision of energy and resolution calibration method of Ge detectors.

Nuclear Instruments and Methods, 564(1), 295-299.

Likar, A., Vidmar, T. (2002).

Analysis of gamma-ray spectra from HPGe detectors in field conditions without explicit energy calibration. Applied Radiation and Isotopes, 57(1), 67-72.

Blagojevic, N., Wood, N. R. (1982).

Holmium-166m sources for energy and efficiency calibration of γ -spectrometry systems. The International Journal of Applied Radiation and Isotopes, 33(2), 153-154.

Helmer, R. G., van der Leun, C. (1999).

Recommended standards for γ -ray energy calibration.

Nuclear Instruments and Methods, 422(1-3), 525-531.

Helmer, R. G., van der Leun, C. (2000).

Recommended standards for γ -ray energy calibration (1999).

Nuclear Instruments and Methods, 450(1), 35-70.

Helmer, R.G., Greenwood, R.C., Gehrke, R.J., 1978.

Reevaluation of precise γ -ray energies for calibration of Ge(Li) spectrometers.

Nuclear Instruments and Methods, 155(1-2), 405-423.

Vanin, V.R., Kenchian, G. , Morales, M., Helene, O., 1997.

An experimental method for a precise determination of gamma-ray energies with semiconductor detectors. Nuclear Instruments and Methods, 391(2), 338-344.

Helene, O., Vanin, V. R., Tsai, S. P. (1999).

Improvement of ^{192}Ir and ^{152}Eu gamma-ray calibration energies by using a self-calibration procedure. Nuclear Instruments and Methods, 433(3), 592-602.

Liu, Z., Peng, L., Wei, L., Chang, T. (1999).

Fine analysis of the calibration curve for a HPGe spectrometer in gamma-ray energy measurement. Nuclear Instruments and Methods, 432(1), 122-129.

Chapter 5

W. Hoffmann, R. Kebeasy, P. Firbas. Introduction to the verification regime of the comprehensive nuclear-test-ban treaty. *Phys Earth Planet Inter.* 113 (1999) 5-9.

O. Dahlman, S. Mykkeltveit, H. Haak. Nuclear Test Ban: converting political visions to reality. (2009) 1st edn. ISBN-13: 978-1402068836.

United Nations General Assembly Resolution Number 50/245, UN. New York, USA, 1996.

Comprehensive Nuclear-Test-Ban Treaty (CTBT), provisional Technical Secretariat, test on the Establishment of a Preparatory Commission for the Comprehensive Nuclear-Test-Ban Treaty Organization, 1996.

B. Bjurman, L.-E. De Geer, I. Vintersved, A.L. Rudjord, F. Ugletveit, H. Aaltonen, K. Sinkko, A. Rantavaara, S.P. Nielsen, A. Aarkrog, W. Kolb. The detection of radioactive material from a venting underground nuclear explosion. *J Environ Radioact.* 11 (1990) 1-14.

L.-E. De Geer. Sniffing out clandestine tests. *Nature.* 382 (1996) 491-492.

R.W. Perkins, L.A. Casey. Radioxenons: their role in monitoring a comprehensive test ban treaty. (1996) Rep. DOE/RL-96-1. Pacific Northwest National Laboratory, Richland, Washington.

L.-E. De Geer. Atmospheric radionuclide monitoring: a Swedish perspective. (1996) In: Huseby ES, Dainty AM (eds) *Monitoring a Comprehensive Nuclear Test Ban Treaty*. Kluwer Academic Publishers, The Netherlands, pp 157–177.

C.R. Carrigan, R.A. Heinle, G.B. Hudson, J.J. Nitao, J.J. Zucca. Trace gas emissions on geological faults as indicators of underground nuclear testing. *Nature.* 382 (1996) 528-531.

L.-E. De Geer. Comprehensive nuclear-test-ban treaty: Relevant radionuclides. *Kerntechnik.* 66 (2001) 113-120.

M. Auer, A. Axelsson, X. Blanchard, T.W. Bowyer, G. Brachet, I. Bulowski, Y. Dubasov, K. Elmgren, J.P. Fontaine, W. Harms, J.C. Hayes, T.R. Heimbigner, J.I. McIntyre, M.E. Panisko, Y. Popov, A. Ringbom, H. Sartorius, S. Schmid, J. Schulze, C. Schlosser, T. Taffary, W. Weiss, B. Wernsperger. Intercomparison experiments of systems for the measurement of xenon radionuclides in the atmosphere. *Applied Radiation and Isotopes.* 60 (2004) 863-877.

P.R.J. Saey, L.-E. De Geer. Notes on radioxenon measurements for CTBT verification purposes. *Applied Radiation and Isotopes*. 63 (2005) 765-773.

M. Auer et al (2009, in press) Ten years of development of equipment for measurement of atmospheric radioactive xenon for the verification of the CTBT. In: Becker A, Schurr B, Kalinowski MB, Koch K, Brown D (eds) Recent advances in nuclear explosion monitoring PAGEOPH topical volume. Birkhäuser Verlag AG, Basel.

M. Zähringer, A. Becker, M. Nikkinen, P. Saey, G. Wotawa. CTBT radioxenon monitoring for verification: Today's challenges. *J Radioanal Nucl.* (2009) 1-6.

Operational Manual for Radionuclide Monitoring and the International Exchange of Radionuclide Data, Preparatory Commission for the Comprehensive Nuclear-Test-Ban Treaty Organization, CTBTO/WGB/TL-115/Rev.8, 2000.

Preparatory Commission for the Comprehensive Nuclear-Test-Ban Treaty Organization (CTBTO), Basic Facts: The Global Verification Regime and the International Monitoring System. (2001), ISBN 92-95021-06-1.

B. Wernsperger, C. Schlosser. Noble gas monitoring within the international monitoring system of the comprehensive nuclear test-ban treaty. *Radiat Phys Chem*. 71 (2004) 775-779.

T.W. Bowyer, K.H. Abel, C.W. Hubbard, M.E. Panisko, P.L. Reeder, R.C. Thompson, R.A. Warner. Field testing of collection and measurement of radioxenon for the comprehensive test ban treaty. *J Radioanal Nucl.* 240 (1999) 109-122.

T.W. Bowyer, C. Schlosser, K.H. Abel, M. Auer, J.C. Hayes, T.R. Heimbigner, J.I. McIntyre, M.E. Panisko, P.L. Reeder, H. Satorius, J. Schulze, W. Weiss. Detection and analysis of xenon isotopes for the comprehensive nuclear-test-ban treaty international monitoring system. *J Environ Radioact.* 59 (2002) 139-151.

Y. Finkelstein. Fission product isotope ratios as event characterization tools - part II: Radioxenon isotopic activity ratios. *Kerntechnik*. 66 (2001) 229-236.

H.S. Miley, T.W. Bowyer, L.R. Greenwood, R.J. Arthur. Fission product ratios as treaty monitoring discriminants. *J Radioanal Nucl.* 276 (2008) 483-487.

JEF-2.2 nuclear dataset (1997).

M.-M. Bé, V. Chisté, C. Dulieu, E. Browne, et al. Table de Radionucléides. LNE-LNHB/CEA, monographie BIPM-5 (2004).

K. Peräjärvi, J. Turunen, J. Hakala, A. Jokinen, I.D. Moore, H. Penttilä, A. Saastamoinen, T. Siiskonen, H. Toivonen, J. Äystö. The decay of ^{133m}Xe . *Applied Radiation and Isotopes*. 66 (2008) 530-534.

- D.A. Haas**, S.R. Biegalski, K.M. Foltz Biegalski. Modeling β - γ coincidence spectra of ^{131m}Xe , ^{133}Xe , ^{133m}Xe and ^{135}Xe . *J Radioanal Nucl.* (2008) 1-5.
- P.L. Reeder**, T.W. Bowyer. Xe isotope detection and discrimination using beta spectroscopy with coincident gamma spectroscopy. *Nuclear Instruments and Methods in Physics Research, Section A: Accelerators, Spectrometers, Detectors and Associated Equipment.* 408 (1998) 582-590.
- W.R. Russ**, D.O. Stuenkel, J.D. Valentine, K.C. Gross. An evaluation of radioxenon detection techniques for use with a fluid-based concentration system. *IEEE Trans Nucl Sci.* 46 (1999) 296-301.
- P.L. Reeder**, T.W. Bowyer, R.W. Perkins. Beta-gamma counting system for Xe fission products. *J Radioanal Nucl.* 235 (1998) 89-94.
- A. Luca**, P. De Felice, G. Tanase. Low level gamma spectrometry by beta-gamma coincidence. *Applied Radiation and Isotopes.* 53 (2000) 221-224.
- P.L. Reeder**, T.W. Bowyer. Delayed coincidence technique for ^{133g}Xe detection. *Nuclear Instruments and Methods in Physics Research, Section A: Accelerators, Spectrometers, Detectors and Associated Equipment.* 408 (1998) 573-581.
- P.L. Reeder**, T.W. Bowyer, J.I. McIntyre, W.K. Pitts. Determination of ^{131m}Xe and ^{133m}Xe in the presence of ^{133g}Xe via combined beta-spectroscopy and delayed coincidence. *J Radioanal Nucl.* 248 (2001) 617-622.
- T.W. Bowyer**, K.H. Abel, C.W. Hubbard, A.D. McKinnon, M.E. Panisko, R.W. Perkins, P.L. Reeder, R.C. Thompson, R.A. Warner. Automated separation and measurement of radioxenon for the comprehensive test ban treaty. *J Radioanal Nucl.* 235 (1998) 77-81.
- A. Ringbom**, T. Larson, A. Axelsson, K. Elmgren, C. Johansson. SAUNA - A system for automatic sampling, processing and analysis of radioactive xenon. *Nuclear Instruments and Methods in Physics Research, Section A: Accelerators, Spectrometers, Detectors and Associated Equipment.* 508 (2003) 542-553.
- M.W. Cooper**, J.I. McIntyre, T.W. Bowyer, A.J. Carman, J.C. Hayes, T.R. Heimbigner, C.W. Hubbard, L. Lidey, K.E. Litke, S.J. Morris, M.D. Ripplinger, R. Suarez, R. Thompson. Redesigned β - γ radioxenon detector. *Nuclear Instruments and Methods in Physics Research, Section A: Accelerators, Spectrometers, Detectors and Associated Equipment.* 579 (2007) 426-430.

- V. V. Prelovskii**, N. M. Kazarinov, A. Yu. Donets, V. Yu. Popov, I. Yu. Popov, N. V. Skirda. The ARIX-03F mobile semiautomatic facility for measuring low concentrations of radioactive xenon isotopes in air and subsoil gas. *Instruments and Experimental Techniques*. 50 (2007) 393–397.
- G.P. Lamaze**. A high efficiency device for the detection of radioactive xenon isotopes. *Nuclear Instruments and Methods in Physics Research, Section A: Accelerators, Spectrometers, Detectors and Associated Equipment*. 385 (1997) 285-289.
- J.A.M. Lopes**, R.E. Morgado, C.A.N. Conde. A metastable xenon isotope detector for treaty verification. *Nuclear Instruments and Methods in Physics Research, Section A: Accelerators, Spectrometers, Detectors and Associated Equipment*. 501 (2003) 623-629.
- G. Le Petit**, C. Jutier, P. Gross, V. Greiner. Low-level activity measurement of $^{131}\text{Xe}^m$, $^{133}\text{Xe}^m$, ^{135}Xe and ^{133}Xe in atmospheric air samples using high-resolution dual X- γ spectrometry. *Applied Radiation and Isotopes*. 64 (2006) 1307-1312.
- W. Zhang**, K. Ungar, M. Bean. Improved radioxenon gamma-spectrometry counting system and its efficiency calibration: Monte carlo simulation and experimental results at enriched xenon counting environment. *J Radioanal Nucl.* 279 (2009) 83-91.
- J.-. Fontaine**, F. Pointurier, X. Blanchard, T. Taffary. Atmospheric xenon radioactive isotope monitoring. *J Environ Radioact.* 72 (2004) 129-135.
- H.S. Miley**, R.L. Brodzinski, J.H. Reeves. Low-background counting systems compared. *J Radioanal Nucl.* 160 (1992) 371-385.
- J. Schulze**, M. Auer, R. Werzi. Low level radioactivity measurement in support of the CTBTO. *Applied Radiation and Isotopes*. 53 (2000) 23-30.
- M. Schwaiger**, F. Steger, T. Schroettner, C. Schmitzer. A ultra low level laboratory for nuclear test ban measurements. *Applied Radiation and Isotopes*. 56 (2002) 375-378.
- T.J. Stocki**, M. Bean, R.K. Ungar, H. Toivonen, W. Zhang, J. Whyte, D. Meyerhof. Low level noble gas measurements in the field and laboratory in support of the comprehensive nuclear-test-ban treaty. *Applied Radiation and Isotopes*. 61 (2004) 231-235.
- T. Schroettner**, M. Schwaiger, P. Kindl. Optimization of an active anti cosmic veto shielding. *Applied Radiation and Isotopes*. 61 (2004) 133-138.
- IEEE Std 325-1996**. Standard Test Procedures for Germanium Gamma-Ray Detectors. Approved 6 January 1997 American National Standards Institute. ISBN 1-55937-885-9.

H.Y. Hwang, T.S. Park, P.J. Oh, J.M. Lee. An improved technique for estimating accidental coincidences in β - γ coincidence counting. *Nuclear Instruments and Methods in Physics Research, Section A: Accelerators, Spectrometers, Detectors and Associated Equipment*. 413 (1998) 228-232.

H.-. Hwang, J.H. Lee, Y.H. Cho, J.I. Byun, T.S. Kim, T.S. Park, J.M. Lee. Measurement of accidental coincidences in β - γ coincidence counting using non-equal dead times. *Nuclear Instruments and Methods in Physics Research, Section A: Accelerators, Spectrometers, Detectors and Associated Equipment*. 488 (2002) 562-565.

D. Smith. Improved correction formulae for coincidence counting. *Nucl Instrum Methods*. 152 (1978) 505-519.

J.H. Ely, C.E. Aalseth, J.I. McIntyre. Novel beta-gamma coincidence measurements using phoswich detectors. *J Radioanal Nucl*. 263 (2005) 245-250.

W. Hennig, H. Tan, W.K. Warburton, J.I. McIntyre. Single-channel BetaGamma coincidence detection of radioactive xenon using digital pulse shape analysis of phoswich detector signals. *IEEE Trans Nucl Sci*. 53 (2006) 620-624.

W. Hennig, Y.X. Chu, H. Tan, A. Fallu-Labruyere, W.K. Warburton, R. Grzywacz. The DGF pixie-4 spectrometer - compact digital readout electronics for HPGe clover detectors. *Nuclear Instruments and Methods in Physics Research, Section B: Beam Interactions with Materials and Atoms*. 263 (2007) 175-178.

W. Hennig, H. Tan, A. Fallu-Labruyere, W.K. Warburton, J.I. McIntyre, A. Gleyzer. A phoswich well detector for radioxenon monitoring. *Nuclear Instruments and Methods in Physics Research, Section A: Accelerators, Spectrometers, Detectors and Associated Equipment*. 579 (2007) 431-436.

R. de la Fuente, B. de Celis, V. del Canto, J.M. Lumbreras, B. de Celis Alonso, A. Martín-Martín, J.L. Gutierrez-Villanueva. Low level radioactivity measurements with phoswich detectors using coincident techniques and digital pulse processing analysis. *J Environ Radioact*. 99 (2008) 1553-1557.

R.M. Ward, S.R.F. Biegalski, D.A. Haas, W. Hennig. Comparison of phoswich and ARSA-type detectors for radioxenon measurements. *J Radioanal Nucl*. (2009) 1-5.

W.R. Schell, J. Vives-Batlle, S.R. Yoon, M.J. Tobin. High-pressure plastic scintillation detector for measuring radiogenic gases in flow systems. *Nuclear Instruments and Methods in Physics Research, Section A: Accelerators, Spectrometers, Detectors and Associated Equipment*. 421 (1999) 591-600.

- P.L. Reeder**, T.W. Bowyer, J.I. McIntyre, W.K. Pitts, A. Ringbom, C. Johansson. Gain calibration of a β/γ coincidence spectrometer for automated radioxenon analysis. Nuclear Instruments and Methods in Physics Research, Section A: Accelerators, Spectrometers, Detectors and Associated Equipment. 521 (2004) 586-599.
- Y. Hino**, S. Matui, T. Yamada, N. Takeuchi, K. Onoma, S. Iwamoto, H. Kogure. Absolute measurement of ^{166m}Ho radioactivity and development of sealed sources for standardization of γ -ray emitting nuclides. Applied Radiation and Isotopes. 52 (2000) 545-549.
- G. F. Knoll**. Radiation detection and measurement. 3rd ed. J. Wiley & Sons, ISBN 0-471-07338-5.
- P.J. Campion**. The standardization of radioisotopes by the beta-gamma coincidence method using high efficiency detectors. Int J Appl Radiat Isot. 4 (1959) 232-240, IN15-IN16, 241-248.
- H. Houtermans**, M. Miguel. $4\pi\text{-}\beta\text{-}\gamma$ coincidence counting for the calibration of nuclides with complex decay schemes. Int J Appl Radiat Isot. 13 (1962) 137-142.
- NCRP**. A Handbook of Radioactivity Measurements Procedures, NCRP **Report No. 58** (2nd ed.), (1985), National Council on Radiation Protection and Measurements.
- ICRU**. International Commission on Radiation Units and Measurements, Dose and Volume Specification for Reporting Interstitial Therapy, ICRU **Report 58** (International Commission on Radiation Units and Measurements, Bethesda); 1997.
- T.S. Park**, H.Y. Hwang, J.M. Lee. An improved coincidence counting technique for standardization of radionuclides. Applied Radiation and Isotopes. 49 (1998) 1147-1151.
- S. Pommé**, L. Johansson, G. Sibbens, B. Denecke. An algorithm for the solid angle calculation applied in alpha-particle counting. Nuclear Instruments and Methods in Physics Research, Section A: Accelerators, Spectrometers, Detectors and Associated Equipment. 505 (2003) 286-289.
- J. I. McIntyre**, M. E. Panisko, T. W. Bowyer, K. W. Pitts. Generation of Radioxenon Isotopes. PNNL-14338 (2003) Pacific Northwest National Laboratory, Richland, Washington 99352.
- Y.V. Dubasov**, N.V. Skovorodkin, E.I. Biryukov. ^{252}Cf -based generator of radioactive xenon isotopes. Radiochemistry. 49 (2007) 297-298.
- D.A. Haas**, S.R. Biegalski, K.M. Foltz Biegalski. Radioxenon production through neutron irradiation of stable xenon gas. J Radioanal Nucl. (2009) 1-4.

F. Pointurier, J. Laurec, X. Blanchard, A. Adam. Cosmic-ray induced background reduction by means of an anticoincidence shield. *Applied Radiation and Isotopes*. 47 (1996) 1043-1048.

J. Laurec, X. Blanchard, F. Pointurier, A. Adam. A new low background gamma spectrometer equipped with an anti-cosmic device. *Nuclear Instruments and Methods in Physics Research Section A: Accelerators, Spectrometers, Detectors and Associated Equipment*. 369 (1996) 566-571.

L.A. Currie. Detection and quantification limits: Basic concepts, international harmonization and outstanding ("low-level") issues. *Applied Radiation and Isotopes*. 61 (2004) 145-149.

L.A. Currie. Detection and quantification limits: Origins and historical overview. *Anal Chim Acta*. 391 (1999) 127-134.

L.A. Currie. Limits for qualitative detection and quantitative determination: Application to radiochemistry. *Anal Chem*. 40 (1968) 586-593.

L.-E. De Geer. Currie detection limits in gamma-ray spectroscopy. *Applied Radiation and Isotopes*. 61 (2004) 151-160.

Statutory declaration

EIDESSTATTLICHE ERKLÄRUNG

Ich erkläre an Eides statt, dass ich die vorliegende Arbeit selbstständig verfasst, andere als die angegebenen Quellen/Hilfsmittel nicht benutzt, und die den benutzten Quellen wörtlich und inhaltlich entnommene Stellen als solche kenntlich gemacht habe.

Graz, am 16.3.2010

.....

(Unterschrift)

Curriculum vitae

Name: Thales Schröttner
Date and Place of Birth: 6th August, 1973, Graz, Austria
Citizenship: Austria
Address: Neubaustrasse 2, 3435 Dürnrohr, Austria
Phone: +43 664 620 7781
E-mail: thales.schroettner@seibersdorf-laboratories.at

Education and Scope of Work

1993-2001

University of Technology Erzherzog Johann, Graz, Austria;
finished study of Technical Physics in 2001; (Graduated Engineer (DI.);
during this time short and medium term contracts for the set up of the Austrian Radionuclide Laboratory ATL03 to support the CTBTO (comprehensive test ban treaty organization);

2001-2003

PHD contract; Monte Carlo Simulation of Radiation Transport in gamma spectrometers;

since June 2003 regular employed of ARC Seibersdorf research; responsible for operation of the Austrian Radionuclide Laboratory ATL03;

2003-2005

design and characterization of ultra low background gamma-spectroscopy systems;
set up of a laboratory for Radioxenon measurement to support the international monitoring system of the CTBTO; development of density gauging systems for industrial applications;

since 2005

in charge of a small (8 people) working group "System Development";
development, testing, installation and support of portal monitoring systems and other nuclear security related equipment; cooperation with IAEA within coordinated research program (CRP); currently expanding testing capabilities of in house test facilities to include special nuclear materials;

Publications

Schwaiger, M., Steger, F., **Schroettner**, T., Schmitzer C., 2002. A ultra low level Laboratory for Nuclear Test Ban Measurements. Applied Radiation and Isotopes, Vol. 56, pp 375-378.

Schroettner, T., Schwaiger, M., Kindl, P., 2004. Optimization of an Active Anti Cosmic Veto Shielding. Applied Radiation and Isotopes, Vol. 61, pp 133-138 (2004).

Feichtinger, J., **Schröttner**, T., Schwaiger, M., Kindl, P., 2004. Characterization of selected cadmium-zinc-telluride detectors. Applied Radiation and Isotopes, Vol. 61, pp 113-115.

Schroettner, T., Putz, O., Presle, G., Zottl, W., 2007. Testing and Improving the detection Capability of Portal monitoring Systems at Higher Transit Speeds. IAEA-CN-154/015P, Proceedings of an international conference "Illicit Trafficking: Collective Experience and the Way Forward", Edinburgh, 19-22 November 2007, ISSN 0074-1884, ISBN 978-92-0-103408-3.

Schröttner, T., Munoz, D., Wästerby, P., Foghelin, J., Broekhuijsen, M., Miller, M., Beckmann, J., Ewert, U., Strebl, F., 2009. CBRNE Related Testing and Certification Facilities – a Network to strengthen Cooperation and Knowledge Exchange within Europe. Proceedings of 3rd Int. Conf. Safety and Security Systems in Europe. Micromaterials and Nanomaterials 10: 42-46.

Schroettner, T., Kindl, P., Presle, G., 2009. Enhancing sensitivity of portal monitoring at varying transit speed. Applied Radiation and Isotopes, Vol. 67, pp 1878-1886.

Schroettner, T., Kindl, P., 2010. Long term comparison of methods to sustain energy calibration in low level gamma-ray spectroscopy and investigation of possible sources for drift. Applied Radiation and Isotopes, Vol. 68, pp 164–168.

Schroettner T., Schraick I., Furch T., Kindl P., A high resolution, multi parameter, β - γ coincidence, μ - γ anticoincidence system for radioxenon measurement. Nuclear Instruments and Methods in Physics Research, Section A: Accelerators, Spectrometers, Detectors and Associated Equipment, submitted to NIM A on 30.1.2010.